Mario Bacher, BSc.

Cardiac Triggering Based on Locally Generated Pilot-Tones in a Commercial MRI Scanner: A Feasibility Study

Master Thesis

October 25, 2017

Institute for Medical Engineering
Graz University of Technology
Stremayrgasse 16/3, A-8010 Graz

Head: Univ.-Prof. Dipl.-Ing. Dr.techn. Rudolf Stollberger

Supervisor TU Graz: Univ.-Prof. Dipl.-Ing. Dr.techn. Rudolf Stollberger

Supervisor Siemens Healthcare: Dr.rer.nat. Peter Speier

1. Statutory Declaration

I declare that I have authored this thesis independently, that I have not used other than the declared sources / resources, and that I have explicitly marked all material which has been quoted either literally or by content from the used sources.

Erlangen, October 25, 2017

Mario Bacher, BSc.

Contents

List of Figures

List of Tables

2. Introduction

Magnetic resonance imaging (MRI) is inherently slow. Therefore, physiological motion such as breathing, heartbeat and also involuntary movement of the patient presents a fundamental challenge and is one of the most frequent sources of image artifacts [70]. Respiratory motion can, in many applications, be controlled by breath-holding but imaging of the beating heart requires synchronization of the MR measurement to cardiac activity. In cardiac MRI, still images are typically created by capturing data during short periods of relative cardiac quiescence. Alternatively, partial images are acquired throughout the cardiac cycle and averaged over several heartbeats [44]. Synchronization to the patient's heartbeat is commonly achieved by the use of electrocardiogram (ECG) or photoplethysmography (PPG) acquired simultaneously during the scan. Common synchronization strategies are triggering and gating. In triggering, the MR acquisition begins after a physiological event, typically the ECG R-wave, has been detected. Gating may be prospective or retrospective. In retrospective gating, data is acquired constantly and is then sorted based on ECG information. In prospective gating, acquisition is started by e.g. the first R-wave and stops shortly before the next R-wave. This cycle is then repeated until the scan is completed. In segmented acquisitions such as cine, the acquisition is subdivided into segments across several R-R intervals and only a fraction of the complete k-space matrix is acquired during each segment. Thus, data is collected over several cardiac cycles and sorted retrospectively. Triggering is usually restricted to the R-wave as this is the only feature that can reliably be extracted from the ECG.

Proper patient preparation such as shaving of chest hair, cleaning of skin with an abrasive prepping gel and careful placement of surface electrodes is time consuming but also of vital importance for successful ECG monitoring. PPG is typically only used as a fallback solution in cases where ECG can not be reliably obtained. Due to the lowpass effect of the vasculature, features in the PPG are not as well defined as the ECGs R-peak. Since PPG is typically measured at the fingertip or earlobe, a patient specific delay between cardiac activity and measured signal is introduced.

When used inside an MR scanner, the ECG is contaminated by additional effects, namely the magnetohydrodynamic (MHD) effect and gradient induced currents in the electrode leads. The MHD is due to motion of charged blood-particles perpendicular to the static magnetic field B_0. Charged particles flowing in B_0 get deflected by the Lorentz force, resulting in a Hall potential across vessel walls, altering the waveform of the ECG. The MHD effect on the ECG is strongest when the flow direction is perpendicular to B_0 and flow velocity is maximal. This is usually the case during the blood ejection phase in the aorta, which coincides with ventricular repolarization (T-wave). Hence, the major MHD-caused effect observed is an increase in T-wave magnitude [2]. The MHD effect increases with field-strength. While T-wave increase is relatively moderate at 1.5 T, it can, at higher field-strengths result in T-waves that are larger in amplitude than the QRS-complex. Figure 2.1 shows a comparison of ECG traces at 0 to 7 T of the same patient. To ensure reliable R-wave triggering, more advanced detection algorithms such as vectorcardiogram (VCG) [18] need to be used.

Gradient induced artifacts are caused by the rapidly switching gradients needed for image acquisition. These time-varying magnetic fields cause induction in the ECG signal leads which manifests as artifacts in the ECG signal. These artifacts can be reduced by filtering. If the gradients and the ECG systems impulse-response are known, more advanced signal processing methods are possible, such as modeling the systems response to gradient switching as an LTI (linear, time-invariant) system [17] or calculating the gradient-induced signal using approximations of Maxwell's equations [71]. However, real-time processing with only minimal de-

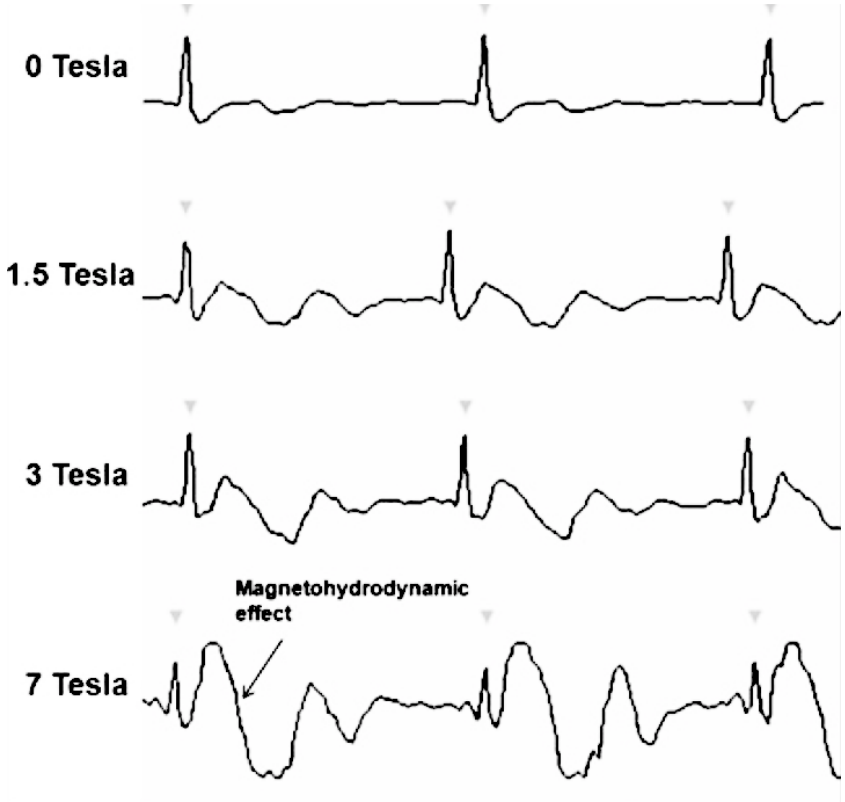

Figure 2.1.: ECG traces using the same electrode placement in the same patient at different field strengths. The MHD effect becomes more pronounced at higher field strengths. Figure from [63].

lay ($< 150\,\text{ms}$ [17], ideally much less) is necessary for triggering, rendering some more advanced processing methods infeasible. One possibility to reduce gradient-induced artifacts is to keep the signal leads as short as possible. Today, wireless ECG amplifiers are commonly used that connect to the ECG electrodes by short leads of only a few centimeters. These amplifiers must however be heavily shielded to operate within the scanners bore, increasing their cost. The effect of gradient-switching is vastly increased when the amplifier and ECG leads are far from the scanners isocenter where gradient switching amplitudes are significantly higher. This is typically the case in angiography of the extremities or head.

Another possibility for motion synchronization are navigator echoes. Navigators are additional radiofrequency (RF) pulses used to dynamically track anatomic motion. Navigators may be based on spin echo (SE) or gradient echo (GRE) [1]. Navigators are more commonly used for respiratory motion, where a thin 2D slice or a pencil-beam is commonly placed intersecting the liver-dome, but can also be used for cardiac motion [46].

An alternative to navigator echoes are self-navigated sequences in which the center of k-space is sampled more frequently and the 1-dimensional fast Fourier transform (FFT) of this readout is treated as a 1D projection of the imaging volume on the superior-inferior (SI) axis [53]. This projection is then compared to a reference taken at the beginning of the scan, usually by taking the cross-correlation to quantify respiratory motion.

However, one fundamental problem of both navigator pulses and self-navigation is that some additional time is needed. Figure 2.2 shows a pulse diagram of a simple spin-echo sequence with an additional navigator pulse played out after the 180 ° inversion pulse. This demand for extra time may be difficult to meet in some applications, especially cardiac MR where fast imaging sequences such as gradient recalled echo (GRE), turbo spin-eche (TSE), balanced steady-state free precession (bSSFP) or echoplanar imaging (EPI) are commonly used and continuous coverage of the cardiac cycle is intended. Introducing navigator echoes in bSSFP for instance would require interrupting the steady-state, which then needs to be build up again. An advantage of navigators however is that motion can be measured quantitatively. Using e.g. a respiratory navigator, both the direction and displacement of the liverdome can be quantified.

Pilot Tones (PT), introduced by Speier et al. [62] are a promising new technique based on the modulation of a locally generated constant RF signal by physiological motion. The PT signal is generated by a low-cost local RF transmitter and is received by the standard MR local coils. Due to the large receive bandwith of the MR scanners receiver, the frequency of the PT signal can be chosen well outside the imaging bandwidth but still inside the receivers bandwidth.

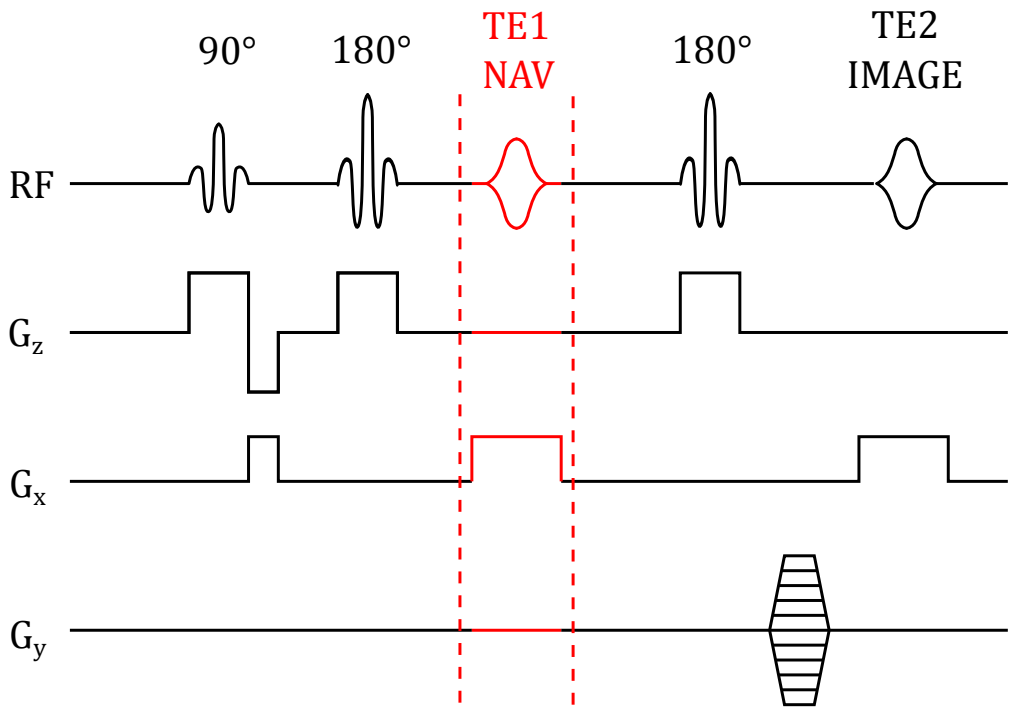

Figure 2.2.: Pulse-diagram of a spin-echo sequence with an additional navigator pulse and echo. G_x = x-axis gradient, G_y = y-axis gradient, G_z = z-axis gradient, RF = radiofrequency pulse. The navigator echo is similar to an image echo, except that no phase encoding is applied. Figure adapted from [15].

It was previously shown by Schröder and Wetzl et al. that the PT signal contains multidimensional respiratory information [59, 61, 67]. PilotTone navigation has an important advantage to navigators and self-navigation: No additional pulses and readouts are necessary. PT navigation works with essentially any sequence without increasing acquisition time. Schröder et al. also found anecdotal evidence of cardiac information encoded in the PT signal [59, 60]. This thesis shall focus on the cardiac information contained in the PT signal and evaluate whether it can be reliably extracted and potentially be used as an alternative to ECG for cardiac triggering and/or gating.

3. Methods

3.1. A Short History of Electromagnetic Diagnostic Methods

The use of electromagnetic waves for contactless monitoring of physiological activity dates back at least to the 1950s, when Moskalenko [42, 43] used microwaves of approx. 1 GHz and measured changes in transmission and reflection caused by changes in volume of blood or respiratory volume. Guy repeated Moskalenkos's experiments at 915 MHz in a human subject and found transmission loss to be proportional to ventricular volume change [32]. Several other groups applied similar methods for monitoring of both cardiac and respiratory activity, e.g. Lin et al. [36, 37] and more recently Pfanner et al. [51, 52].

Fig. 3.1 shows results from above groups: (a) Moskalenko's transmission experiments at 1 GHz in 1958. Oscilloscope traces from top to bottom: Rubber hose filled with NaCl and expanded by squeezing a gummi ball. Beating human heart with transmitter at 5^{th} intercostal space (breath-hold). Beating human heart with transmitter at 2^{nd} intercostal space (breath-hold). Respiratory motion. Sagittal transmission through the brain. Image from [42] (b) Guy's experiments at 915 MHz in 1972. From top to bottom: Ventricular volume change as reference. Recorded transmission loss. Recorded ECG as reference. Timing signal. Image from [32] (c) Lin et al's "Apexcardiogram" at 2.4 GHz, with phono- and electrocardiogram as reference. The transmitter was positioned over the apex. Image from [37] (d)

Pfanner et al. used continuous wave radar at 869 MHz and an array of receive antennas for cardiac gating in computed tomography (CT). Image from [51]

Note that while Moskalenko, Guy and Lin et al. measured transmission, Pfanner et al. used continuous-wave radar.

A commonality shared by all of the methods presented above is that the applied frequency is in or near the GHz range, corresponding to wavelengths in air of approx. $10 - 30$ cm. This means, that for typical transmitter/receiver placements (e.g. some centimeters to meters anterior and posterior of the thorax) and electrically large antennas (i.e. antennae physically larger than one half-wavelength), interaction with the patient happens well within the far-field region (sometimes called the Fraunhofer region), in which E- and H-fields are orthogonal and in-phase to each other. Figure 3.2 shows the most common definition of the reactive and radiative near-field, the far-field and the transition zone between them.

3.2. The Pilot Tone Navigator

Speier et al. [62] introduced Pilot Tone (PT) navigation for use in respiratory synchronization in magnetic resonance imaging (MRPT). This chapter shall focus on describing how the PT signal is generated and how it affects the received MR signal. Finally, a hypothetical model is presented that describes how physiological motion modulates the PT carrier-wave.

In telecommunications engineering, pilot tones (pilots) are defined as e.g. "a signal, usually a single frequency, transmitted over a communications system for supervisory, control, equalization, continuity, synchronization, or reference purposes" [45]. Pilot tones can e.g. be used to infer information about the transmission channel. The sender transmits a pilot of known waveform, e.g. a sine wave with known amplitude and frequency. This pilot is then subjected to the channels transmission characteristics, i.e. dampening or amplification, filtering, compression, distortion

(a) Moskalenko, 1GHz
1958

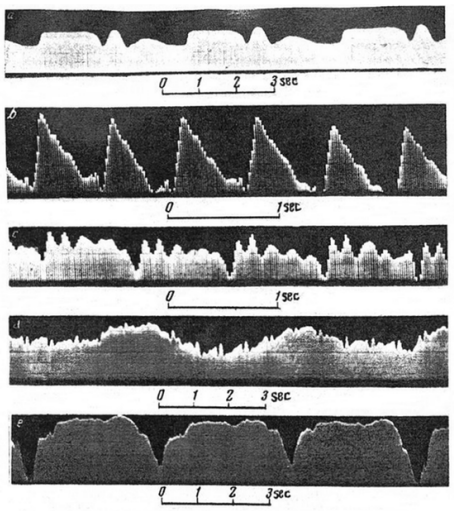

(b) Guy, 915MHz
1972

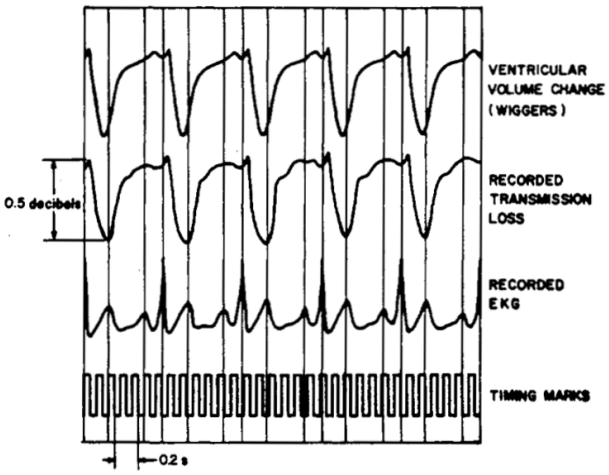

(c) Lin et al., 2.4GHz
1979

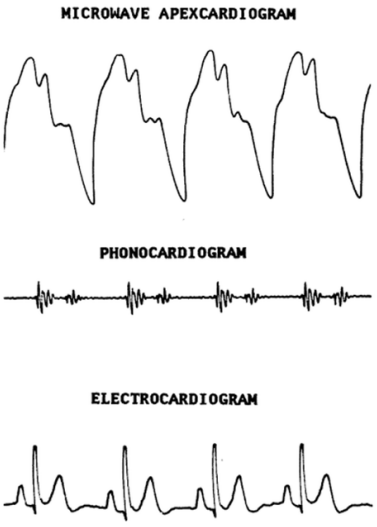

(d) Pfanner et al., 869MHz
2013

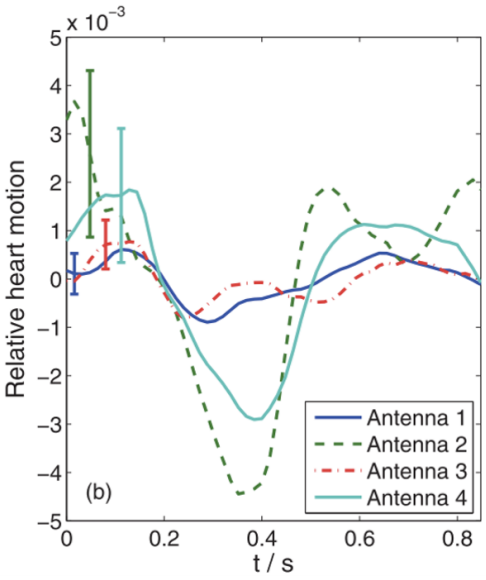

Figure 3.1.: Electromagnetic waves used for measuring physiological signals, 1958-2013.

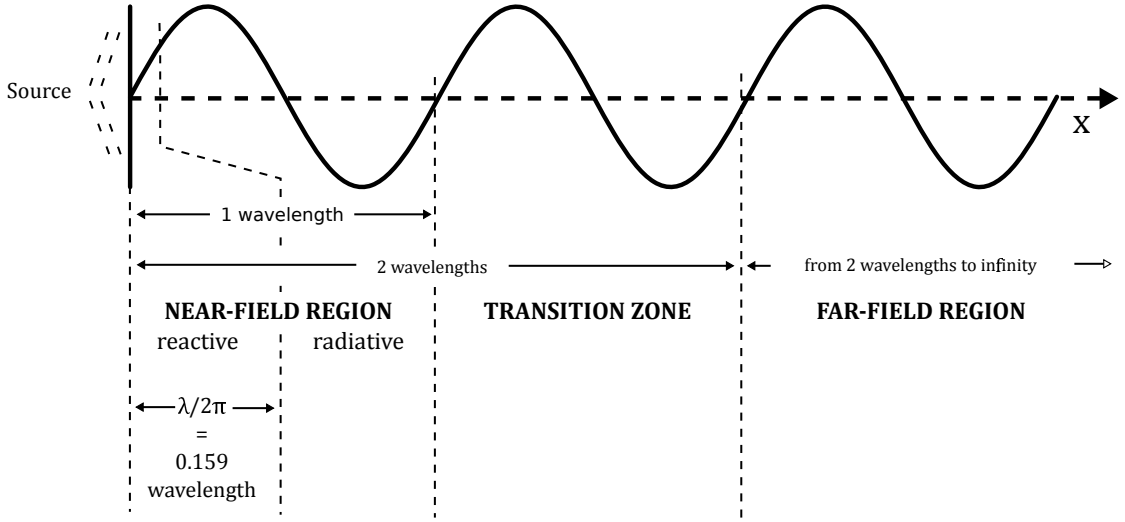

Figure 3.2.: Diagram showing the approximate distances of the near- and far field. Note that the distance at which the far-field starts is dependent on the dimension D of the antenna. Generally, a distance of $2D^2/\lambda$ is used for the near/far-field boundary. Modified from `https://commons.wikimedia.org/wiki/File:Field_regions_for_typical_antennas_vector.svg`

etc. By measuring the pilot at the receiver and comparing it to the original signal, one can infer information about the channel.

Here, the pilot is a continuous wave RF signal outside of the field of view (FOV), but inside the application bandwidth (approx. 63 MHz ± several $10 - 100$ kHz at 1.5 T). The pilot signal can be created either by a standard synthesizer and a non-resonant pickup coil, mounted on e.g. the scanner's cover [62] or by a standalone device. For this thesis, a prototype standalone implementation, built by Jan Bollenbeck (Siemens Hardware R&D), was provided (see Fig. 3.3), transmitting at a frequency of 63.4429 MHz.

The amplitude of the pilot signal was chosen to be received with significantly lower magnitude than the MR signal. In Fig. 3.4 one readout through the center of k-space (top) and its Fourier-tansform (bottom) are plotted. The left peak is the

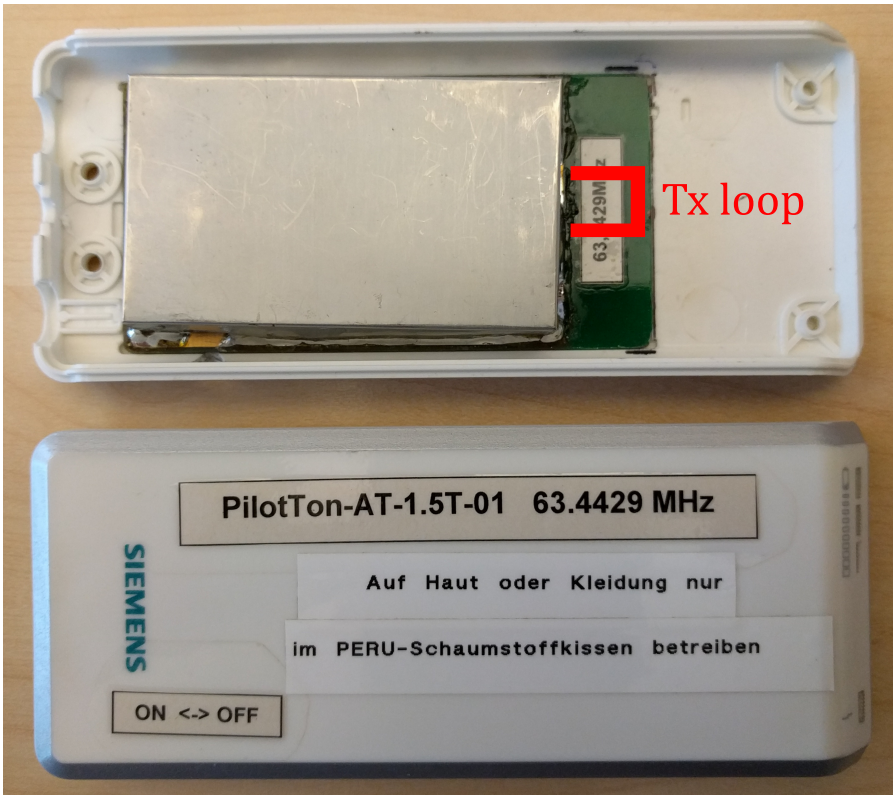

Figure 3.3.: Standalone variant of the pilot tone transmitter (PTx). The fixed frequency of 63.4429 MHz is generated using a quartz-stabilized oscillator circuit and output through a printed half-loop antenna.

PT signal, well outside the frequency range used for imaging. Here, the PT peak is slightly larger than the amplitude of the MR signal.

Figure 3.5 shows an MR image reconstructed from one coil prior to removal of the PT signal on the left. On the right, a single line of k-space in readout-direction, indicated by the red line, is plotted over 500 repetitions (5.5 images/s, GRE, $TR = 189\,\text{ms}$, $TE = 1.04\,\text{ms}$, Pixel BW: 975 Hz).

Contrary to the methods presented in the previous section, where the frequency can be chosen relatively freely, the pilot's frequency range is constrained by the field strength B_0 ($f_0 = B_0\gamma$) and the receiver's bandwidth, usually some $10 - 100\,\text{kHz}$ above and below f_0.

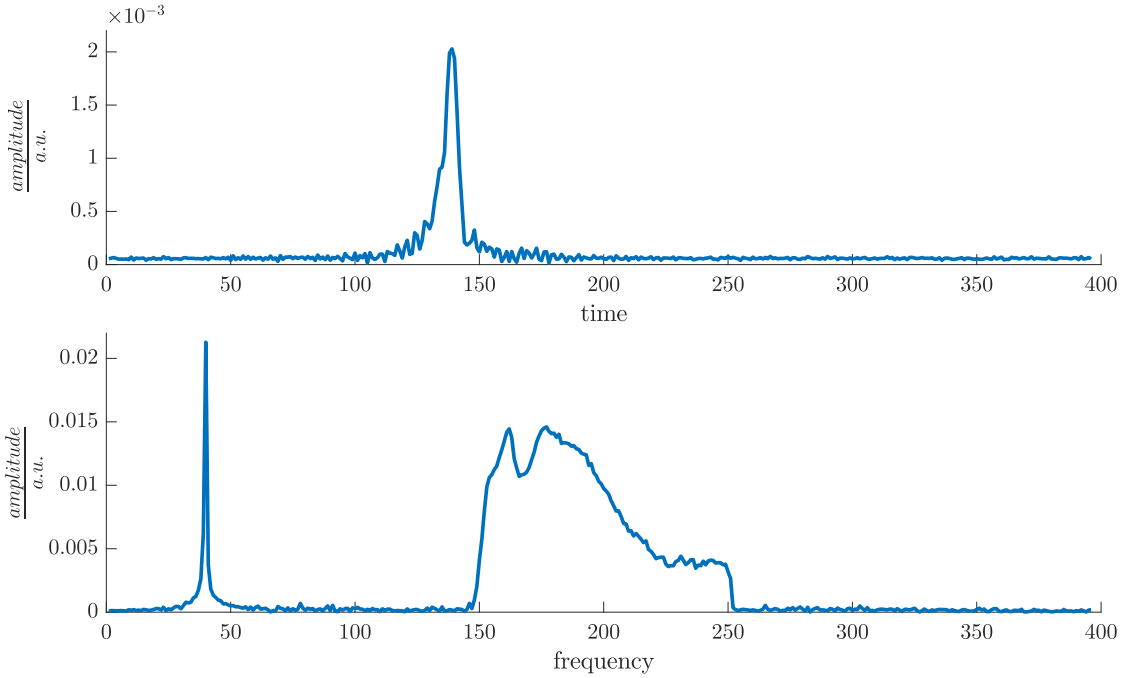

Figure 3.4.: Single readout through the center of k-space (top) and its Fourier-transform (bottom).

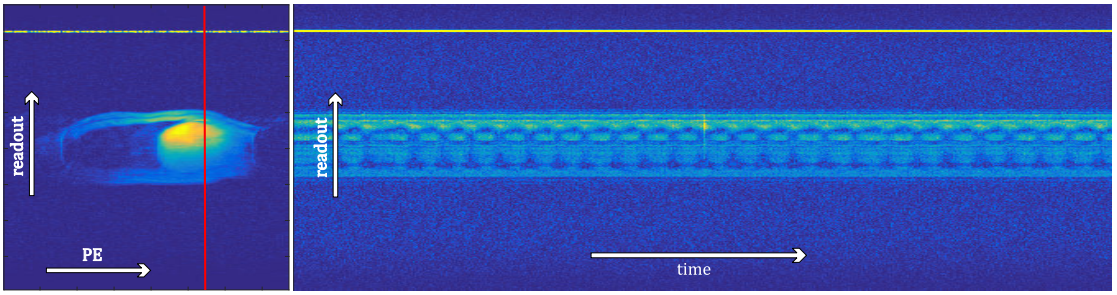

Figure 3.5.: Left: Image reconstructed from one coil. Right: One k-space line in readout direction, indicated by the red line in the left image, plotted as a time-series over 500 repetitions. PE-direction: H-F, readout-direction: A-P.

Typically, this necessitates some degree of oversampling to ensure that the PT navigator signal is within the field of view.

This restriction to approx. 63 MHz at 1.5 T leads to some interesting differences compared to the methods shown above. Most notably, when using frequencies of 1 GHz and above, wavelengths are on the order of several cm, whereas at 63 MHz, $\lambda_0 \approx 4.8\,\mathrm{m}$ (in vacuum). This means, that for a typical setup, where the receivers and the transmitter are placed on or a few centimeters away from the patient, all interaction with biological tissue happens well within the reactive near-field region which, for electromagnetically short antennae (i.e. shorter then one half of the transmitted wavelength), is defined as the region with a radius $r < \frac{\lambda}{2\pi}$ ($r < 0.73\,\mathrm{m}$ at 1.5 T). In this region, the relationship between the electric and magnetic field is usually quite complex. The name "reactive near-field" stems from the fact that in this region, the antenna itself reacts to EM absorption, whereas absorption far from the antenna has no effect on the near-field [57]. Essentially, energy from the source (the oscillator) is stored in the magnetic (H) and electric (E) fields close to the antenna. Since both fields are out of phase with each other by 90 °, no energy is radiated close to the antenna as this would require the E- and H-field to be in-phase.

This also means, that mathematical models typically used to describe the interaction between transmitter- and receiver-antenna do not apply. Instead, the system might best be described as inductive coupling between two coils, separated by a conductive and/or magnetic medium and with arbitrary orientations to each other, similar to a transformer or near-field communication (NFC). The fact that both the PT antenna and the scanners receive antennae are loop antennae (or half-loop in the case of the PT transmitter) means that they will transmit and receive mostly the magnetic field as opposed to dipole antennae, which would transmit/receive mainly the electric field.

In this model, two phenomena are expected to contribute to the PT signal (see Fig. 3.6): The transmitter loop generates a magnetic field, which is changed by the medium and then induces a current in the receiving coils. Any change in the composition of the separating medium is reflected in a change of the magnetic field

and subsequently the induced current, a phenomenon called inductive- or magnetic coupling.

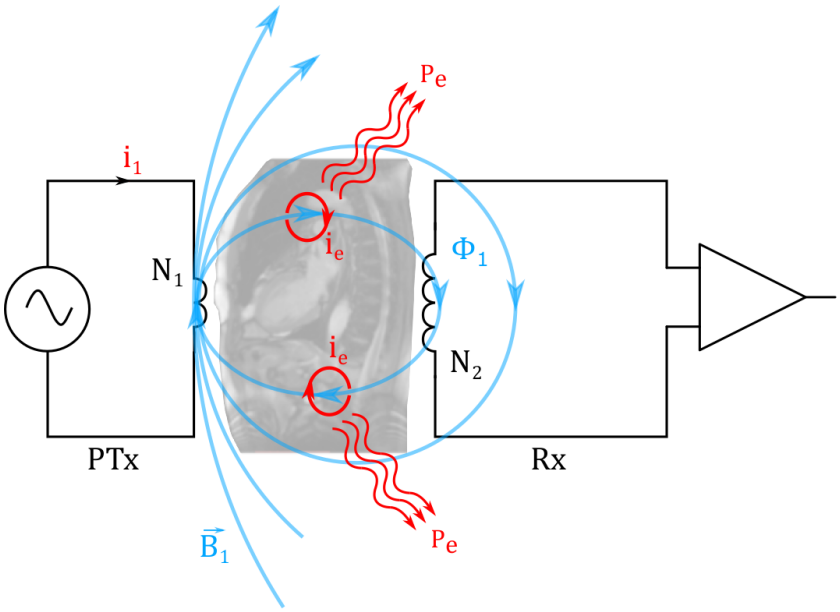

Figure 3.6.: Inductive coupling: An AC electric current generates a magnetic field in coil 1. Field lines intersecting coil 2 induce an electric current in coil 2. Eddy-currents i_e are induced in conductive tissues and take away energy from the magnetic field which is ultimately dissipated as heat P_e.

This inductive coupling can be described in terms of mutual inductance: Let coil L_1 in Fig. 3.6 have N_1 turns and carry a current of $i_1(t)$, giving rise to a magnetic field $\mathbf{B}_1$. Some of the magnetic field lines of $\mathbf{B}_1$ will intersect the receive coil L_2 and induce a current. Let Φ_{21} be the magnetic flux through one turn of coil L_2, having N_2 turns, then by Faraday's law of induction the resulting electromotive force ε in the receiving coil is

$$\varepsilon(t) = -N_2 \frac{d\Phi_{21}}{dt} = -\frac{d}{dt} \iint_{coil2} \mathbf{B}_1 \cdot d\mathbf{A}_2 \tag{3.1}$$

with the sign given by Lenz's law. $d\mathbf{A}_2$ is a surface element in the plane spanned by the receiving coil. The rate of change of $\varepsilon(t)$ is proportional to the change of current $i_1(t)$

$$N_2 \frac{d\Phi_{21}(t)}{dt} \propto M \frac{di_1(t)}{dt} \tag{3.2}$$

with M the so called mutual inductance, which is dependent on geometrical factors such as the number of turns and the coils radii . This is, however, only strictly true for coupling in vacuum. In tissue, the magnetic field $\mathbf{B}_1$ at distance $\mathbf{r}$ from the transmitting coil will be influenced by the surrounding mediums magnetic permeability μ, which is either scalar for isotropic or a second rank tensor for anisotropic media and may also be complex at high frequencies. Magnetic permeability μ is the distinguishing magnetic property of matter and describes a materials ability to conduct magnetic flux. Figure 3.7 shows the behaviour of magnetic field lines in vacuum, dia- ($\mu < 1$) and paramagnetic ($\mu > 1$) matter.

Permeability is often given as relative permeability to the permeability in vacuum:

$$\mu_r = \frac{\mu}{\mu_0} \tag{3.3}$$

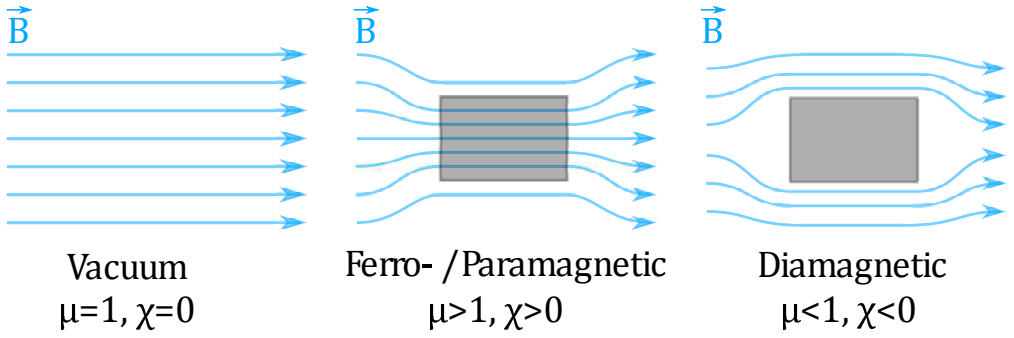

Figure 3.7.: Magnetic field lines in vacuum, ferro-/ paramagnetic and diamagnetic media.

Thus, in practice Eqn. (3.1) must be reformulated to

$$N_2 \frac{d\Phi_{21}(t)}{dt} = kM \frac{di_1(t)}{dt} \tag{3.4}$$

where k is a coupling factor $0 < k < 1$ that is proportional to the permeability μ at position $\mathbf{r}$ and, in the case of PilotTone navigation, also on time as the motion of the heart and lung changes the geometric distribution of μ in the transmission volume.

Permeability in biological tissue is relatively close to that of vacuum and and most tissues are diamagnetic, with the notable exception of desoxigenated blood, which contains a Fe-atom in the hemoglobin molecule. If it binds oxygen, it changes to a diamagnetic state [20], a phenomenon which is exploited in functional BOLD (blood oxygen level dependent) imaging.

Table 3.1 gives magnetic susceptibility ($\chi = \mu - 1$) values for some tissues.

Additionally, as most biological tissues are conductive (see Tab. 3.2), the changing magnetic field will also give rise to eddy-currents in tissues. This conversion of energy stored in the magnetic field to electrical currents and ultimately heat, further decreases the magnetic fields amplitude at the receiver. In a transformer with a (typically iron) core, this loss due to eddy-currents is characterized as

$$P_e = K_e f^2 K_f^2 B^2 \tag{3.5}$$

where K_e is an material dependent eddy-current constant, K_f^2 is a geometry constant and B is the magnetic field. The eddy-current constant K_e is given mainly by the electrical conductivity σ. Contrary to permeability/susceptibility, the conductivity of blood is, to the authors best knowledge, not affected by factors such as oxygenation. Therefore, the eddy-current loss P_e can be assumed to be modulated mainly by changes in geometry. Table 3.2 gives the conductivities for some biological tissues at several frequencies.

It is not known whether eddy-current loss or changes in susceptibility contribute more to the PT signal, but seeing that susceptibility in biological tissues is ex-

Table 3.1.: Magnetic susceptibility $\chi = \mu - 1$ for air, water and some biological tissues. Data from Glaser [20].

	After Maniewski (1991)	After Khenia et al. in: Maret et al (1986)
	10^{-6}	10^{-6}
Air	+0.34	+0.264
Water	-9.05	-9.04
Arterial blood	-9.1	-9.3
Oxygenized erythrocytes		-9.03
Venous blood	-8.4	-7.8
Desoxygenized erythrocytes		+3.88
Lungs (inhaled)	-3.9	
Lungs (exhaled)	-4.1	
Lungs (15% air content)		-4.2
Muscle	-9.0	-9.03
Liver	-8.8	-8.26
Bone	-10	-10

Table 3.2.: Conductivity of some biological tissues at different frequencies. Excerpt from [50].

	Conductivity at frequency			
	13.56 MHz	27.12 MHz	433 MHz	915 MHz
	S/m	S/m	S/m	S/m
Blood	1.16	1.19	1.27	1.41
Lungs (inhaled)	0.11	0.13	-	-
Lungs (exhaled)	0.29	0.32	0.71	0.78
Muscle	0.74	0.76	1.12	1.45
Liver	0.49	0.58	0.89	1.06
Fat	0.21	0.21	0.26	0.35

tremely low, it seems reasonable to assume that eddy-current loss should be the main factor in modulation of the PT signal.

3.2.1. PilotTone raw-data extraction

As the pilot signal is always active, it needs to be separated from the readout. For each ADC (analog to digital converter) readout and for each of the m channels $k = 1 \dots m$, a model for the pilot signal $s_{PT,k}$ is fit to the measured data $s_{meas,k}$ and then subtracted to get the MR signal $s_{MR,k}$, which, owing to the quadrature demodulation used in MRI systems is complex

$$\begin{aligned} s_{PT,k}(t) &= a_k e^{j\omega t} \\ s_{MR}(t) &= s_{meas,k}(t) - s_{PT,k}(t) \end{aligned} \tag{3.6}$$

where ω is the known pilot signal frequency and a_k is a complex amplitude. The model is based on the assumption that a single ADC readout is short enough to ignore modulation due to motion. The PT signal is not synchronized to the down-mixing oscillator, resulting in arbitrary phase. Therefore, the phases of signals $s_{PT,k}(t)$ are normalized sample by sample to an arbitrary reference channel by

$$\begin{aligned} c_{phase} &= \left(\frac{s_{PT,ref}[i]}{|s_{PT,ref}[i]|} \right)^* \\ s_{PT,k,norm}[i] = s_{PT,k}[i] \cdot c_{phase} &= a_{k,norm}[i] e^{j\omega t[i]} \\ i &\in [1, \dots, T] \end{aligned} \tag{3.7}$$

where * denotes complex conjugate and i is the sample number. $s_{PT,ref}$ is the PT signal in an arbitrarily chosen channel used for phase-normalization. The complex amplitude $a_{k,norm}$ is logged as raw PT navigator date for further processing.

A modified image reconstruction program, implemented in ICE (Image Computation Environment, Siemens Healthcare, Erlangen, Germany) was provided for this thesis by Matthias Fenchel (Siemens MR Predevelopment).

In this thesis, only magnitude PT data is used and magnitude is taken before removing the PT signals offset.

Figure 3.8 shows example magnitude raw PT navigator data for one channel and its spectum after offset removal. Peaks at 1.17 Hz (cardiac motion) and around 0.26 Hz (respiratory motion) are clearly visible.

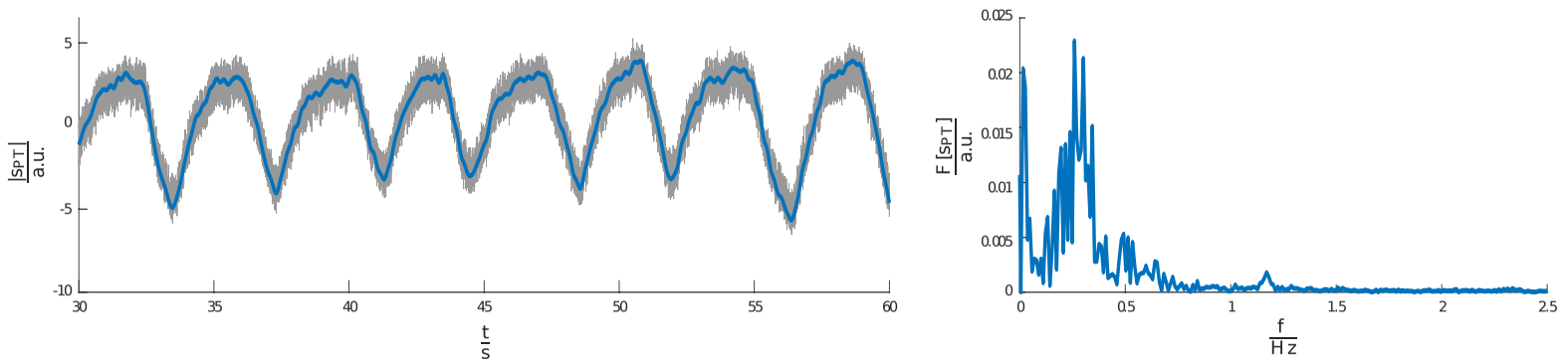

Figure 3.8.: Raw magnitude PT data in one receive coil and its magnitude spectrum. Unprocessed rawdata is shown in grey, data shown in blue has been lowpass-filtered (FIR, $f_{pass} = 4\,\mathrm{Hz}$, $f_{stop} = 5\,\mathrm{Hz}$, stopband attenuation 120 dB.

3.3. Independent Component Analysis

Consider the case where physical phenomena, emanating from k different sources inside a measurement volume V_{meas} are measured simultaneously by m sensors placed at arbitrary positions around V_{meas}. The signal being measured at each of the n sensors then is a (non)linear, unknown mixture of these sources. For instance, an electrode placed at the scalp receives a linearly weighted sum of the electrical activities from the underlying brain areas. The problem of separating these sources, without further knowledge of the characteristics of the sources and V_{meas}, is known as "Blind Source Separation". One popular method to solve this problem is Independent Component Analysis (ICA), proposed by Comon [12].

3.3.1. Principal Component Analysis

PCA tries to find a new orthogonal basis of the data, such that the variance is maximized in the direction of the new base vectors. This can be accomplished be calculating the eigenvectors and eigenvalues of the covariance matrix. The goal of PCA is, given a set of multivariate measurements, to find a smaller set of variables with less redundancy, that gives as good a representation of the original data as possible [27].

Consider the $m \times n$ matrix $\mathbf{X} = [\mathbf{x}_1 \dots \mathbf{x}_m]^T$, where $\mathbf{x}_i$ is the centered (i.e. zero-mean) $1 \times n$ vector of measurements of sensor i. The covariance-matrix $\mathbf{\Sigma}_X$ is then given by

$$\mathbf{\Sigma}_X = \mathrm{cov}(\mathbf{X}) = \mathrm{E}\{\mathbf{X}\mathbf{X}^T\} \approx \frac{1}{n-1}\mathbf{X}\mathbf{X}^T \tag{3.8}$$

where $E(\cdot)$ is the expectation and $\frac{1}{n-1}$ is a normalization factor used when estimating the mean. In $\mathbf{\Sigma}_X$, the ij^{th} element is the product of the i^{th} and j^{th} vector of measurements, i.e. the diagonal elements of $\mathbf{\Sigma}_X$ are the variances of the measurements whereas the off-diagonal elements represent the covariances between

measurement vectors. The covariance matrix is always a square, symmetric $m \times m$ matrix and, without proof, semi-definite.

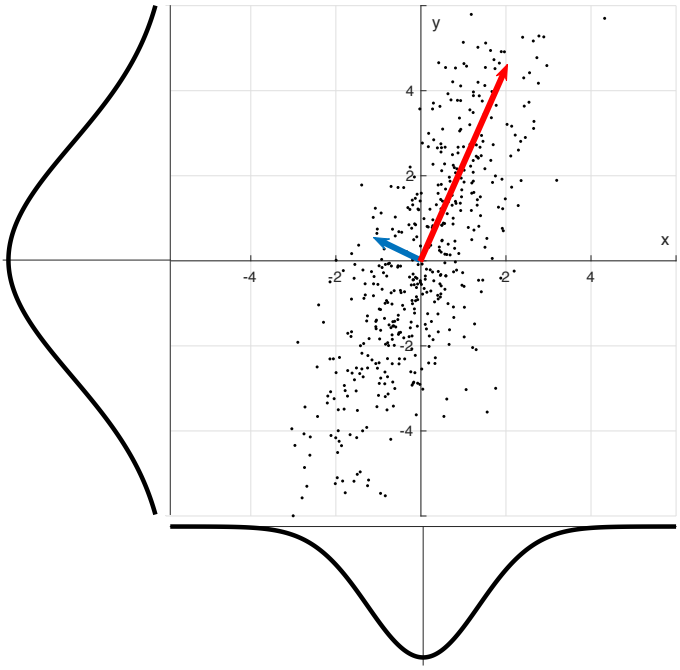

Figure 3.9.: Scatterplot of artificial data from two sensors. Probability densities are shown along the original x- and y-axis. Eigenvectors of the covariance matrix $\mathbf{\Sigma}_X$ are shown in red and blue.

Fig. 3.9 shows an artificial, two-dimensional example of two noisy sensors with means $\mu_1 = \mu_2 = 0$, $\sigma_1 = 6$ and standard deviations $\sigma_2 = \frac{6}{4}$. The covariance matrix is

$$\mathbf{\Sigma}_X = \begin{bmatrix} 1.7395 & 2.8068 \\ 2.8068 & 7.5415 \end{bmatrix} \tag{3.9}$$

Clearly, $\mathbf{x}_1$ and $\mathbf{x}_2$ are correlated, as suggested by the nonzero off-diagonal elements of $\mathbf{\Sigma}_X$. Eigendecomposition yields the two orthogonal eigenvectors, scaled by their respective eigenvalues, shown in blue and red. This demonstrates qualitatively how the variance is maximal along the first axis $\mathbf{e}_1$ in this new base. The second axis,

$\mathbf{e}_2$ corresponds to the maximal variance in the direction orthogonal to the first axis and so on.

In this new coordinate system $\{\mathbf{e}_1, \mathbf{e}_2\}$ the random vectors $\mathbf{x}_1$ and $\mathbf{x}_2$ are uncorrelated. The principal components are then the projections $\mathbf{y}_i = \mathbf{e}_i\mathbf{x}_i$ of $\mathbf{X}$ on $\{\mathbf{e}_1 \dots \mathbf{e}_n\}$. In practice, many of the variances will be so small that they can be discarded, considerably reducing the dimensionality with minimal loss of information.

Thus, the principal components $\mathbf{y}_i$ are guaranteed to be uncorrelated. Uncorrelatedness, however, is a weaker condition for separation of sources than statistical independence, as is used in ICA.

Statistical independence is mathematically defined in terms of probabilities $P(\cdot)$: Let X, Y be random variables. These random variables are said to be statistically independent if and only if

$$P_{X,Y}(X, Y) = P(X)P(Y) \tag{3.10}$$

which leads to the basic property

$$\mathrm{E}\{g(X)h(Y)\} = \mathrm{E}\{g(X)\}\,\mathrm{E}\{h(Y)\} \tag{3.11}$$

with $g(\cdot)$ and $h(\cdot)$ absolutely integrable functions. Recall that two random variables X and Y are said to be uncorrelated if the property

$$r_{XY} = \mathrm{E}\{XY\} = \mathrm{E}\{X\}\,\mathrm{E}\{Y\} \tag{3.12}$$

holds. Comparing Eq. (3.11) and Eq. (3.12) reveals, that independence is a much stronger property than uncorrelatedness. If $g(\cdot)$ and $h(\cdot)$ are linear functions, Eq. (3.11) reduces to Eq. (3.12). In the special case that all random variables are gaussian distributed, uncorrelatedness and independence are the same thing and ICA reduces to PCA. In ICA, at most one source is allowed to be gaussian.

3.3.2. The ICA Model

Independent Component Analysis expands on the idea of PCA by demanding not only uncorrelatedness but actual independence of components. In practice, components will not be completely independent, but their mutual independence can be maximized. The ICA problem can be formulated as follows: Given a set of observations of random variables $(x_1(t), x_2(t), \ldots, x_n(t))$, where t is the time or sample index, assume that they are generated as a linear mixture of independent components:

$$\begin{pmatrix} x_1(t) \\ x_2(t) \\ \vdots \\ x_n(t) \end{pmatrix} = \mathbf{A} \begin{pmatrix} s_1(t) \\ s_2(t) \\ \vdots \\ s_n(t) \end{pmatrix} \tag{3.13}$$

with $\mathbf{A}$ an unknown mixing matrix. Independent Component Analysis now consists of estimating both $\mathbf{A}$ and the $s_i(t)$ when only observing the $x_i(t)$ [27].

Therefore, some measure of independence has to be defined. The central limit theorem states that a sum of non-gaussian random variables approaches gaussianity as $n \to \infty$. This means, that any linear combination of "true" independent components will be closer to gaussianity than either of its constituents. Taking linear combinations $y = \sum_i b_i x_i$ of the observed (mixed) signals, maximizing the non-gaussianity of y leads to an independent component.

Several contrast-functions have been proposed to quantify non-gaussianity, e.g. kurtosis, negentropy or mutual information [12]. In general, higher-order cumulants, i.e. generalizations of variance using higher order polynomials, work well as contrast functions as these are zero for gaussian random variables.

3.3.3. Estimation of Independent Components

Recall the mixing model from Eq. (3.13),

$$\mathbf{x} = \mathbf{A}\mathbf{s} \tag{3.14}$$

which is a linear mixture of the individual components. Since $\mathbf{A}$ is invertible, the independent components are

$$\mathbf{s} = \mathbf{A}^{-1}\mathbf{x} \tag{3.15}$$

Each individual independent component is a linear combination of the form

$$\mathbf{y} = \mathbf{b}^T\mathbf{x} = \sum_i b_i x_i \tag{3.16}$$

where the independent component y is an estimation of s. Finding a vector $\hat{\mathbf{b}}$ that maximizes non-gaussianity gives one independent component. The optimization landscape for nongaussianity in the n-dimensional space of vectors $\mathbf{b}$ has $2n$ local maxima, two for each independent component, corresponding to $-s_i$ and s_i. This also means, that independent components can be estimated only up to a multiplicative sign [27].

3.3.4. Preprocessing

Prior to performing ICA, some preprocessing will, in practical applications, be necessary. In particular, ICA relies on the data to be centered (zero mean) and of unit variance, i.e. whitened. Additionally, the data may be reduced in dimensionality by performing PCA and discarding components with small corresponding eigenvalues.

After centering the data, its covariance matrix $\mathbf{\Sigma}_X$ is computed. If the data were white, the diagonal of $\mathbf{\Sigma}_X$ would be unity. In practice, this will likely not be the case, and a whitening transform will be necessary. Whitening is usually combined with decorrelation, that is, a transformation is computed such that $\mathbf{\Sigma}_X = \mathbf{I}$, where $\mathbf{I}$ is the unit matrix.

This transform is found by first solving the eigenvalue problem on $\mathbf{\Sigma}_X$,

$$\begin{aligned} \mathbf{\Sigma}_X \mathbf{\Phi} &= \mathbf{\Phi} \mathbf{\Lambda} \\ \mathbf{\Phi}^T \mathbf{\Sigma}_X \mathbf{\Phi} &= \mathbf{\Lambda} \end{aligned} \tag{3.17}$$

where $\mathbf{\Lambda}$ is a diagonal matrix of eigenvalues. The columns of $\mathbf{\Phi}$ are the eigenvectors of $\mathbf{\Sigma}$.

The matrix $\mathbf{\Phi}$ diagonalizes $\mathbf{\Sigma}_X$ and thus decorrelates the data $\mathbf{X}$.

$$\mathbf{X}_{decorr} = \mathbf{X} \mathbf{\Phi} \tag{3.18}$$

To achieve whiteness, the covariance matrix must not only be diagonal but unity. Observing that

$$\mathbf{\Lambda}^{-1/2} \mathbf{\Lambda} \mathbf{\Lambda}^{-1/2} = \mathbf{I} \tag{3.19}$$

and substituting this in Eq. (3.17) yields

$$\mathbf{\Lambda}^{-1/2} \mathbf{\Phi}^T \mathbf{\Sigma}_X \mathbf{\Phi} \mathbf{\Lambda}^{-1/2} = \mathbf{I} \tag{3.20}$$

Thus, whitening the data means multiplying by the scaling factor $\mathbf{\Lambda}^{-1/2} \mathbf{\Phi}$.

$$\mathbf{X}_{decorr,white} = \mathbf{Z} = \mathbf{X} \mathbf{\Lambda}^{-1/2} \mathbf{\Phi} \tag{3.21}$$

Fig. 3.10 shows a two-dimensional geometric interpretation of the whitening process. Removing the mean of $\mathbf{X}$ centers the joint distibution around the mean (top right). Eigenvectors of $\mathbf{\Sigma}_X$ are the major and minor axes of an ellipse or, for $n \geq 4$, of an hyperellipsoid. Decorrelation is essentially a rotation, such that the eigenvectors of $\mathbf{\Sigma}_X$ coincide with the x_1 and x_2 axis. Finally, whitening scales the joint distribution along x_1 and x_2 to ensure equal variance. Note, that the

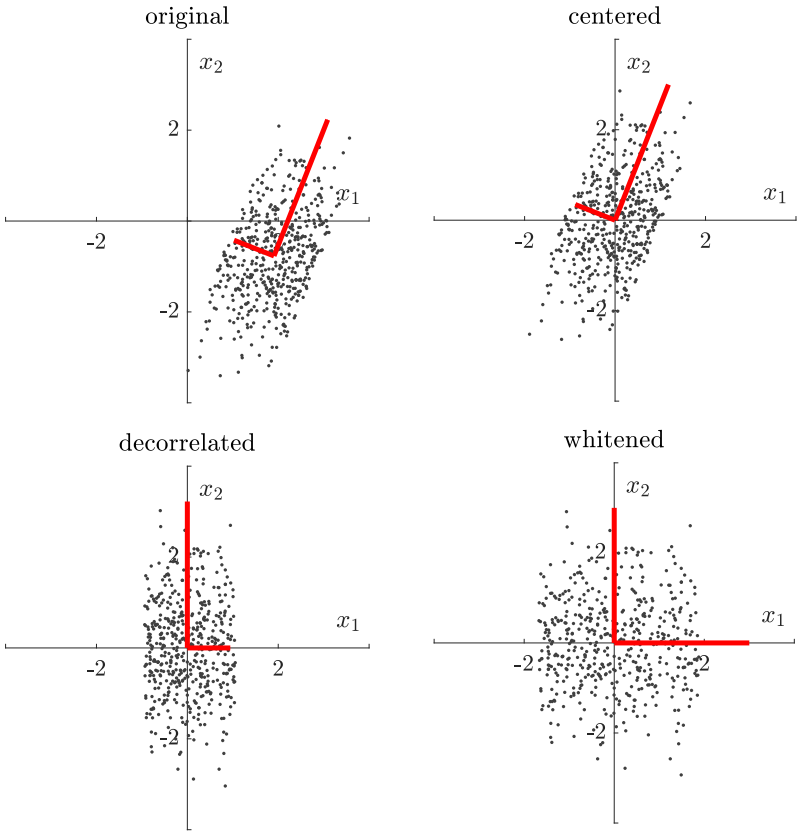

Figure 3.10.: Scatterplot of artificial data. Two random variables, one from a gaussian distribution and one from a uniform distribution. Top left: original data. Top right: data after removing the mean. Bottom left: decorrelation transform applied to the centered data. Bottom right: whitening transform applied to centered data. Eigenvectors are shown in red and have been scaled by a factor of 3 to improve readability.

eigenvectors are now of equal length and form radii of a unit-(hyper)sphere (this is why whitening is sometimes called "sphering"). The whitening transform consists of a rotation followed by scaling - it is an affine transform.

3.3.5. The FastICA Algorithm

The FastICA (FICA) algorithm, proposed by Hyvärinen [28], works by minimizing mutual information between transformed variables s_i, building on the method by Comon [12], expressing mutual information using negentropy.

Negentropy is approximated based on the maximum entropy principle [26] in the form

$$J(y_i) \propto c\left[\mathrm{E}\{G(y_i)\} - \mathrm{E}\{G(v)\}\right]^2 \tag{3.22}$$

where G is any non-quadratic function, c is a constant and v is a standardized gaussian variable. Choice of G determines the quality of the negentropy estimation. Choosing a G that does not grow too fast gives a more robust estimator [27]. Finding an independent component means maximizing $J_G(\mathbf{b})$

$$J_G(\mathbf{b}) = \left[\mathrm{E}\{G(\mathbf{b}^T\mathbf{x})\} - \mathrm{E}\{G'(\mathbf{b}^T\mathbf{x})\}\right]^2 \tag{3.23}$$

with $\mathbf{b}$ an m-dimensional vector of weights under the constraint $\mathrm{E}\{(\mathbf{b}^T\mathbf{x})^2\} = 1$. This can be extended to up to n independent components, maximizing the sum of n contrast functions, taking into account the constraint of decorrelation [28]:

$$\begin{aligned} &\text{maximize } \sum_{i=1}^{n} J_G(\mathbf{b}_i) \quad \text{w.r.t. } \mathbf{b}_i, \quad i = 1, \ldots, n \\ &\text{under constraint } \mathrm{E}\{\left(\mathbf{b}_k^T\mathbf{x}\right)\left(\mathbf{b}_j^T\mathbf{x}\right)\} = \delta_{jk} \end{aligned} \tag{3.24}$$

where every vector $\mathbf{b}_i$ gives one row of the unmixing matrix $\mathbf{B}$. The independent components are then

$$\mathbf{y} = \mathbf{B}\mathbf{x} \tag{3.25}$$

The optimization problem from Eq. (3.24) can be solved using a gradient descend algorithm. Taking the gradient $\nabla(\cdot)$ of the approximization of negentropy from Eq. (3.8) and considering the normalization in Eq. (3.24), gives the update rule

$$\Delta \mathbf{b} \propto \gamma \, \mathrm{E}\{\mathbf{z} \nabla(\mathbf{b}^T \mathbf{z})\} \tag{3.26}$$

To ensure $\mathbf{b}$ projects on the unit-hypersphere, keeping the variance of $\mathbf{b}^T \mathbf{z}$ constant and unity, $\mathbf{b}$ is normalized

$$\mathbf{b} \leftarrow \mathbf{b} / ||\mathbf{b}|| \tag{3.27}$$

The step-size γ is calculated as

$$\Delta \gamma \propto \Big(G(\mathbf{b}^T \mathbf{z}) - \mathrm{E}\{G(\mathbf{v})\} \Big) - \gamma \tag{3.28}$$

Some possible choices for G are given by Hyvärinen [27]:

$$\begin{aligned} G_1(y) &= \frac{1}{\alpha_1} \log \cosh \alpha_1 y \\ G_2(y) &= -\exp(-y^2/2) \end{aligned} \tag{3.29}$$

with $1 \leq \alpha_1 \leq 2$ some suitable constant. Consequently, g are the derivatives of Eqs. (3.29)

$$\begin{aligned} g_1(y) &= \tanh(\alpha_1 y) \\ g_2(y) &= y \exp(-y^2/2) \end{aligned} \tag{3.30}$$

Alternatively, the problem can be solved much faster using Newton's method. While the Newton method usually converges in a small number of steps, it has the computational disadvantage of needing a matrix-inversion in each step. Hyvärinen developed an algorithm approximating Newton's method that does not require

matrix inversion but still, in theory, converges roughly with the same number of iterations as the real Newton method [28], called FastICA.

For estimating more than one independent component, FICA can be run using deflationary orthogonalization. Independent components are estimated one by one. After estimating p vectors $\mathbf{b}_1, \ldots, \mathbf{b}_p$, the projections of the previously estimated p vectors are subtracted and $\mathbf{b}_{p+1}$ is re-orthonormalized. For an in-depth derivation of the algorithm see [27, 28]

Data: whitened data $\mathbf{z}$, # of independent components to estimate k
Result: demixing vectors $\mathbf{b}$
initialization: choose an initial (e.g. random) vector $\mathbf{b_p}$, set $p \leftarrow 1$
for $p \leq k$, $p \leftarrow p + 1$ **do**
  while *not converged* **do**
    Let $\mathbf{b} \leftarrow \mathrm{E}\{\mathbf{z}g(\mathbf{b}^T\mathbf{z})\} - \mathrm{E}\{g'(\{\mathbf{b}^T\mathbf{z})\}\mathbf{b}$
    Orthogonalize $\mathbf{b}_p \leftarrow \mathbf{b}_p - \sum_{j=1}^{p-1} \left(\mathbf{b}_p^T\mathbf{b}_j\right)\mathbf{b}_j$
    Normalize $\mathbf{b} \leftarrow \mathbf{b}/||\mathbf{b}||$
  end
end

Algorithm 1: FastICA algorithm for estimating m ICs with deflationary orthogonalization. The expectations are in practice estimated as sample means.

Alternatively, re-orthonormalization can be done once all k demixing vectors have been updated on the matrix of demixing vectors $\overline{\mathbf{B}}$ by solving

$$\mathbf{B} = \left(\overline{\mathbf{B}\mathbf{B}}^T\right)^{-\frac{1}{2}}\mathbf{B} \tag{3.31}$$

using an appropriate method such as eigendecomposition of $\overline{\mathbf{B}\mathbf{B}}^T = \mathbf{F}\mathbf{D}\mathbf{F}^T$ as $\left(\overline{\mathbf{B}\mathbf{B}}^T\right) = \mathbf{F}\mathbf{D}^{-\frac{1}{2}}\mathbf{F}^T$ or, as is used in FastICA the iterative algorithm by Hyvärinen [28]:

In this approach, no vectors are "privileged" over others which might be beneficial in some applications [33].

Data: matrix of demixing vectors $\overline{\mathbf{B}} = \left(\mathbf{b}_1^T, \mathbf{b}_2^T \dots \mathbf{b}_k^T\right)$
Result: symmetric re-orthonormalization of demixing vectors $\mathbf{B}$
Let $\overline{B} = \frac{\overline{\mathbf{B}}}{||\overline{\mathbf{B}}\overline{\mathbf{B}}||}$
while *not converged* **do**
  $\mathbf{B} = \frac{3}{2}\mathbf{B} - \frac{1}{2}\mathbf{B}\mathbf{B}^T\mathbf{B}$
end

Algorithm 2: Hyvärinens algorithm for symmetric orthonormalization of demixing vectors. The norm $||\cdot||$ can be, in theory, any ordinary matrix norm, except the Frobenius norm [28].

3.3.6. ICA Quality & Reliability Measures

The performance of ICA, i.e. it's ability to reliably separate components, is highly dependent on the chosen parameters, such as the degree of dimensionality reduction in the preceding PCA, the number of independent components that are to be fit, preprocessing of data (lowpass filtering to improve SNR), the used contrast function and the choice of separation algorithm (i.e. deflationary, see Algorithm 1) or the symmetric approach (Algorithm 2) described in more detail in [28].

The ICA demixing matrix is, in the absence of a more reliable starting guess, initialized with random numbers and the algorithm is expected to produce slightly different solutions with each new run and may also be prone to getting trapped in local minima (or maxima, if maximizing e.g. non-gaussianity).

Therefore, any evaluation of ICA performance must be done statistically, using a Monte-Carlo approach, that is, running ICA several times and comparing results. Himberg et al. [23] have developed ICASSO, a Matlab toolbox aimed at assessing both the algorithmic stability and reliability of independent components using clustering and visualization.

To assess the validity of found components, the ICA algorithm is run several times on the same dataset using random initial guesses for the demixing matrix. Results are then compared by some kind of similarity measure. In the case of ICASSO,

Himberg at al. use the mutual corellation coefficient of the estimated independent components.

Recall the ICA model from Eq. 3.13

$$\mathbf{x} = \mathbf{A}\mathbf{s} \tag{3.32}$$

and

$$\mathbf{s} = \mathbf{W}\mathbf{x} \tag{3.33}$$

where $\mathbf{A}$ is the mixing matrix and $\mathbf{W}$ its pseudo-inverse, i.e. the demixing matrix separating independent components. FastICA [28] is then run M times, each run producing an estimate $\hat{\mathbf{W}}_i$ with $i = 1 \dots M$, of the demixing matrix which is collected in a single matrix $\hat{\mathbf{W}} = [\hat{\mathbf{W}}_1^T, \hat{\mathbf{W}}_2^T \dots \hat{\mathbf{W}}_M^T]^T$. Estimating a fixed number n_i of independent components in each round, the resulting matrix $\hat{\mathbf{W}}$ will be of size $K \times k$, where $K = \sum_i n_i$ and k is the dimension of each individual component vector.

The mutual correlation coefficient $r_{ij}, \quad i, j = 1, \dots, K$ are then the ij^{th} element of the matrix

$$R = \hat{\mathbf{W}}\mathbf{C}\hat{\mathbf{W}}^T \tag{3.34}$$

where $\mathbf{C} = \text{cov}\{\mathbf{x}\}$ is the covariance matrix of the original data. Since in ICA the sign of the ICs is undetermined, correlations can be positiv or negative. The final similarity matrix is therefore taken as

$$\sigma_{ij} = |r_{ij}| \tag{3.35}$$

In ICASSO, also a dissimilarity index is used, defined intuitively as

$$d_{ij} = 1 - \sigma_{ij} \tag{3.36}$$

The clustering method used in ICASSO is agglomerative hierarchical clustering (AHC), a bottom up clustering method. The basic algorithm for doing AHC is given below, for a more in-depth description see e.g. Everitt et al. [16].

Data: data points x_i
Result: Cluster $C = \{x_1, \ldots, x_K\}$ containing all data points and dendogram
Initialization: each cluster contains one data point: $C_i = \{x_i\}$
while *number of clusters* > 1 **do**
  Find a pair of clusters that is closest: $\min_{i,j} D(C_i, C_j)$
  Merge the clusters C_i, C_j into a new cluster $cCi + j$
  Remove C_i, C_j from the collection C, add C_{i+j}
end

Algorithm 3: Basic algorithm for agglomerative hierarchical clustering. The algorithm is run until there is only a single cluster left. A dendogram is produced, which is a hierarchical tree of clusters. Computational complexity: $\mathcal{O}(n^2K + n^3)$. The operator $D(\cdot, \cdot)$ defines a distance metric over clusters.

The dendogram is an intuitive visualization of the clustering process: In Figure Fig. 3.11 the individual data points ("leafs") are drawn at the abscissa, the distance metric $D(\cdot, \cdot)$ on the ordinate. First, the two closest data points $\min_{i,j} D(x_i, x_j)$ are found and a connecting horizontal line is drawn at the corresponding distance. These two data points now form the cluster C_{i+j}. Now this process is repeated until only one big cluster containing all data points is left.

Several metrics can be used for distance $D(\cdot, \cdot)$. In ICASSO, group average-linkage (AL) is used:

$$D_{AL}(C_k, C_l) = \frac{1}{n_{C_k} n_{C_l}} \sum_{i \in C_k, j \in C_l} d_{ij} \tag{3.37}$$

that is, the distance between clusters C_k and C_l is the average euclidian distance over all pairwise distances between data points in those clusters.

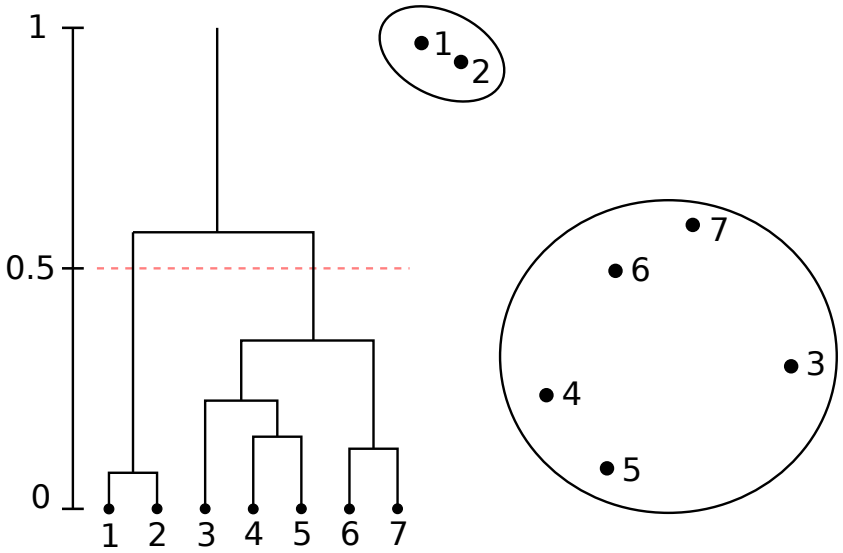

Figure 3.11.: Right: Data points and clustering into two clusters. Left: corresponding dendogram. The dashed line represents the distance d_{cut} used to generate the two clusters.

To produce L disjoint clusters, the user can either specify a distance at which clusters should be considered to be seperate (essentially cutting the dendrogram with a horizontal line at some arbitrary distance d_{cut} or the user specifies a specific number L of clusters and the distance d_{cut} is found such that the cut results in L clusters.

For visual inspection, Himberg et al. also provide a tool for nonlinear projection of data points into a $2D$ space. A convex hull bounds the data points belonging to a cluster and data points are connected by lines whose thickness or color is determined by their similarity σ_{ij} [23]. In this visualization, the smaller the convex hull is the more compact is it's corresponding cluster. An ideal cluster would contract into a single point [23]. An example of this visualisation is shown in Fig. 3.13. Essentially, tightly clustered and well separated data points correspond to estimated ICs that differ only little between realizations of FastICA and are maximally dissimilar to other ICs. In this example, the following ICA parameters were used:

- Algorithm: symmetric
- Contrast: gauss
- Number of ICs: 10
- Reduced dimensionality: 12

Figure. 3.12 left shows the found independent components, ranked from top to bottom by their quality index I_q. Quality- and reliability indices are plotted in the middle and rightmost plots respectively. The independent components plotted on the left represent the "mean" component from 200 runs of FastICA. These so called "centrotypes" are also indicated in Fig. 3.13 by blue circles. The cardiac component (number 1, plotted in blue) was found 199 times out of 200 and appears compact and isolated, indicating high reliability.. Note that the number of centrotypes in this example is 12 instead of the expected 10. This is because in some runs, components were found that did not lie in any of the clusters. These rarely found components (9 and 6) therefore form clusters of their own. Clusters 9, 10, 11 and 12 are overlapping and have comparatively low I_q and I_r.

Let C be the set of all estimated ICs, C_m the set of indices that belong to the m^{th} cluster and $|C_m|$ the size of the m^{th} cluster. The quality index I_q is then defined as

$$I_q(C_m) = \frac{1}{|C_m|^2} \sum_{i,j \in C_m} \sigma_{ij} - \frac{1}{|C_m||C_{-m}|} \sum_{i \in C_m} \sum_{j \in C_{-m}} \sigma_{ij} \tag{3.38}$$

where C_{-m} is the set of indices that does not belong to the m^{th} cluster. Thus, I_q is essentially the difference between the average intra-cluster similarity and the average extra-cluster similarity [23].

Additionally, the number of times the component was found is given, which can be used to measure the reliability as

$$I_r = \frac{\#found}{\#trials} \quad \in [0, 1] \tag{3.39}$$

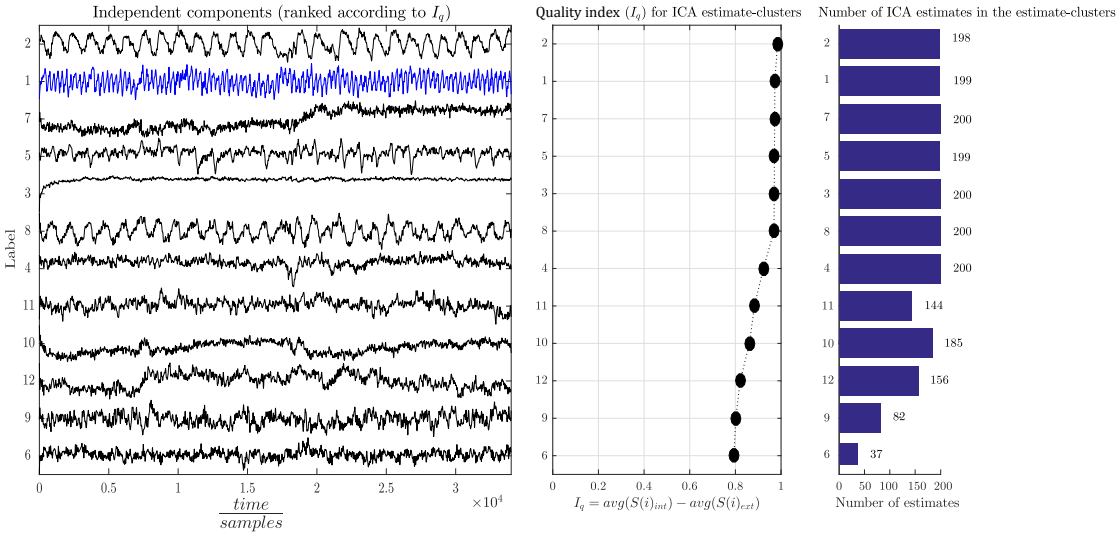

Figure 3.12.: Independent components, ranked by I_q (left), corresponding quality index I_q (center) and times the component was found over 200 trials with randomized starting-guess. The traces on the left are the "mean" components, i.e. centrotypes shown in Fig. 3.13. The cardiac component is shown in blue. The labels used in this plot correspond to those in Fig. 3.13.

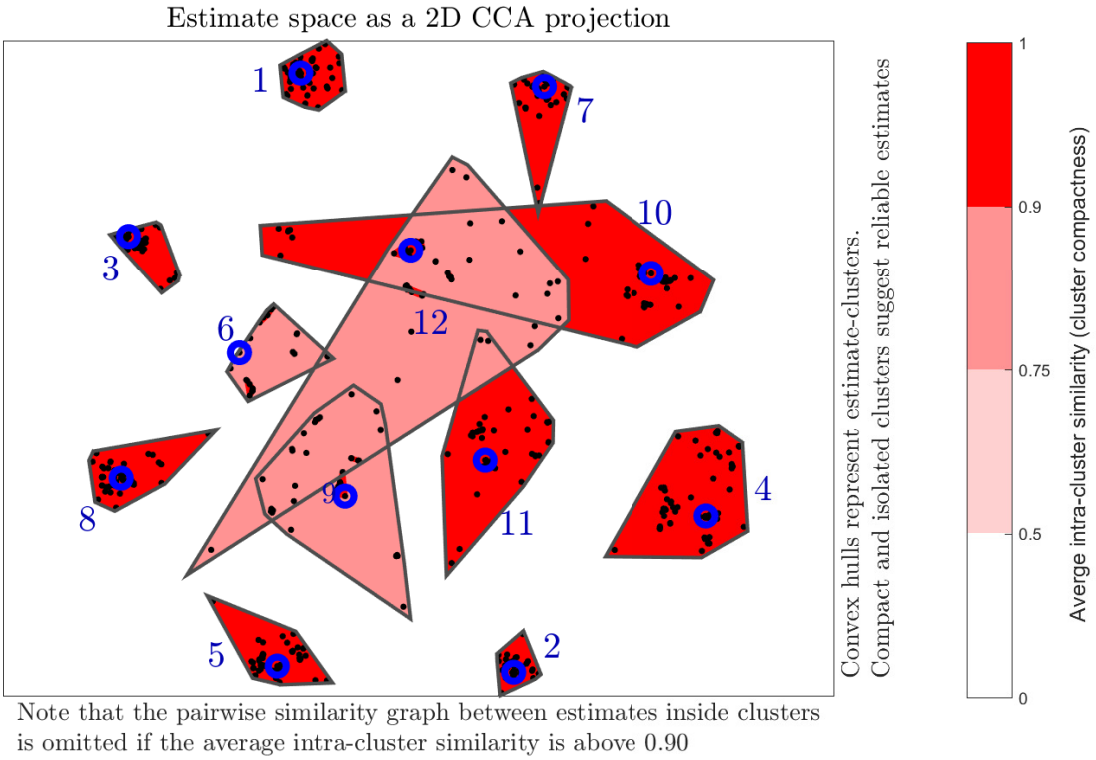

Figure 3.13.: Example cluster visualization. FastICA was run 200 times. Clusters are colored by their average intra-cluster similarity. Note cluster number 1 (top left), corresponding to the cardiac IC and cluster numbers 2 and 8 corresponding to respiratory motion.

4. Experimental setup

To assess the feasibility of PilotTone based cardiac triggering, several factors need to be evaluated: First, the cardiac signal needs to be reliably extracted from the raw data and separated from other components such as respiratory motion. Secondly, triggers obtained from the cardiac signal need to correspond well to those obtained from the ground truth ECG. Additionally, since the Transmitter is a small standalone device and can be positioned freely it is necessary to evaluate the influence of transmitter position on the end result. The following chapter will explain the different analyses used to answer these questions.

Figure in the Appendix shows a flow-chart of all steps, from acquisition of the raw data through (pre)processing of the PilotTone signal to final statistical analysis.

All experiments were performed on a 1.5T system (MAGNETOM Aera, Siemens Healthcare GmbH, Germany) on a diverse group of healthy volunteers recruited from the Siemens volunteer pool (14 male, 6 female, age: 56 ± 15 a, height: 1.72 ± 0.08 m, weight: 77 ± 15 kg, BMI: 26 ± 5.3).

The prototype standalone MRPT transmitter (Tx) was affixed to a Body 18 coil (Siemens Healthcare GmbH, Germany), roughly anterior to the volunteers heart. Additionally, the 16 most proximal channels of the 32 channel Spine 32 coil embedded in the patient table were active, covering the volunteers abdomen and thorax. The coil- and PTx placement is shown in Fig. 4.1. Volunteers were instructed to either breathe freely or to perform breath-holds during the 90 s scan at their discretion.

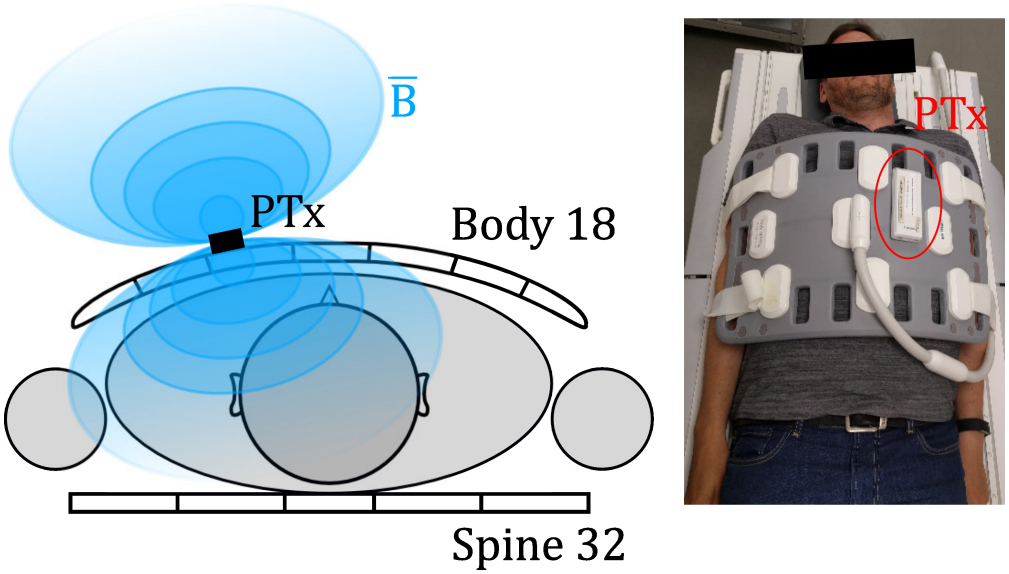

Figure 4.1.: The PT transmitter was affixed to the Body 18 coil array so as to lie roughly anterior to the volunteers heart.

On each volunteer multiple free-breathing, fluoroscopic scans (GRE, $TR = 2.78\,\text{ms}$, $TE = 1.04\,\text{ms}$, $5\,\text{images/s}$) were performed over $93\,\text{s}$ each. This resulted in an effective sampling-rate of the PilotTone signal s_{PT} of $f_s = 359.7\,\text{s}^{-1}$. A standard four-lead electrocardiogram (ECG) and ECG R-peak positions ($\mathbf{T}_{ECG}$) were recorded alongside as ground truth.

The PilotTone signal for each scan was processed by a prototype reconstruction program implemented in ICE (Image Calculation Environment, Siemens Healthcare GmbH, Germany) as described in section 3.3.4, yielding a complex valued $N \times k$ navigator matrix $\mathbf{N}_{PT}$ where k is the number of receive channels and N is the number of complex samples per channel.

4.1. Modulation Depth

Modulation depth is essentially a measure of what fraction of the received signals amplitude carries actual information relative to the carrier waves amplitude. Ac-

cording to the model proposed in Sec. 3.2, any physiological motion modulates the continuous wave PT carrier. Processing using the ICE program described in Sec. 3.2.1 results in a complex $T \times k$ matrix $\mathbf{x}$ where k is the number of channels and T is the length of the PT signal, dependent on acquisition duration and effective sampling rate, containing the phase-normalized complex amplitude $a_{k,norm}$, see Eq. (3.7). The complex amplitude $a_{k,norm}$ consists of a DC offset and some AC component due to modulation. To quantify the strength of modulation, modulation depth (in percent) is defined as

$$m = 100 \cdot \frac{M}{A} \tag{4.1}$$

where M is the peak-to-peak modulation amplitude and A is the carriers amplitude. Here, M and A are defined as

$$M_k = \max(a_{k,norm}) - \min(a_{k,norm}) \tag{4.2}$$

and

$$A_k = \text{mean}(a_{k,norm}) \tag{4.3}$$

resulting in

$$m_k = 100 \cdot \frac{\max(a_{k,norm}) - \min(a_{k,norm})}{\text{mean}(a_{k,norm})} \tag{4.4}$$

Modulation depth was computed for all available datasets (16 volunteers, free-breathing and interspersed breath-holds, 119 datasets total, 90 s acquisition each).

Additionally, the same analysis was performed on only free-breathing datasets (69 datasets total).

4.2. Optimized ICA Parameters

The performance of ICA depends on a number of parameters: In the preprocessing step, dimensionality reduction is performed by PCA. Here, the user can choose freely how many principal components should be retained. ICA then must be set up with the number of individual components that should be estimated, the contrast function and the algorithm used for performing FastICA (deflationary or symmetric approach).

This experiment is designed to determine what combination of parameters offers the overall best quality and reliability.

To this end, FastICA was run 200 times (runs) for each combination of

- Algorithm: symmetric, deflationary
- Contrast function: tanh, exp, power, gauss and skewness
- Number of independent components (3-12)

giving a total of 80 possible combinations and a total of 16.000 FastICA runs. The IC corresponding to cardiac motion was then picked by visual inspection and its quality index and reliability stored for further analysis.

Due to the extremely high computational burden, dimensionality reduction by PCA was fixed to the 12 largest principal components and the analysis was run only on one dataset of a free breathing volunteer (volunteer 08, see App. Tab.). Magnitude data was centered and lowpass filtered prior to PCA/ICA.

The number of clusters L was chosen to correspond to the number of ICs. This should give an indication of how many ICs can be reliably estimated.

If a component is not found in every trial, i.e. $I_r << 1$, it is more likely that those few datapoints are closer together, giving a high quality index I_q. Therefore, a combined quality- and reliability-index $I_{qr} = I_r I_q$ was used to assess overall quality and reliability, essentially penalizing those components that are not found consistantly.

Following this analysis, the three best performing combinations were applied to all datasets of free-breathing volunteers (68 total) to evaluate whether those parameters perform consistently over a wide range of volunteers.

Results were statistically analyzed using Wilcoxon's signed-rank test and Quade's test. For in-depth information on the statistical tests used, the reader is referred to e.g. [8, 49]. Statistical computations were performed using R (R Foundation for Statistical Computing, Vienna, Austria [55]).

The ideal combination of FastICA parameters found in this analysis, while potentially not truly "optimal", nevertheless should provide a good starting point for robust FastICA performance and was subsequently used for all other experiments in this thesis.

4.3. Comparison of PT & ECG Triggers

In the following experiments, the independent component relating to cardiac motion was extracted using the FastICA parameters found in Section 4.2 (pre-filtered data, symmetric algorithm, tanh contrast function and 12 ICs) and compared to ECG ground truth.

Independent components were extracted in Matlab 2016a (MathWorks, Natick, USA) using the FastICA package (Hyvärinen et al. [28]). The independent component relating to cardiac motion $s_{PT}(t)$ was identified automatically by choosing the component with the highest spectral power in the frequency band $0.8 - 3\,\mathrm{Hz}$.

To further suppress high-frequency noise and any possible contribution from respiratory motion due to imperfect separation of components, $s_{PT}(t)$ was bandpass filtered in the time-domain using a FIR filter of order $N = 2000$. The filter was set to a passband of $[0.7 \ldots 5.5]\overline{RR}^{-1}$ where $\overline{RR}^{-1}$ is the inverse of the mean R-R interval calculated from ECG data. Passband frequencies were chosen to include the fundamental heart rate ($\overline{RR}^{-1}$) and up to four possible harmonics. Typically, the fundamental heart-rate and one to four peaks at approximately the corresponding

harmonic frequency could be identified in the spectrum, see e.g. Fig. 4.2 and Fig. 4.3.

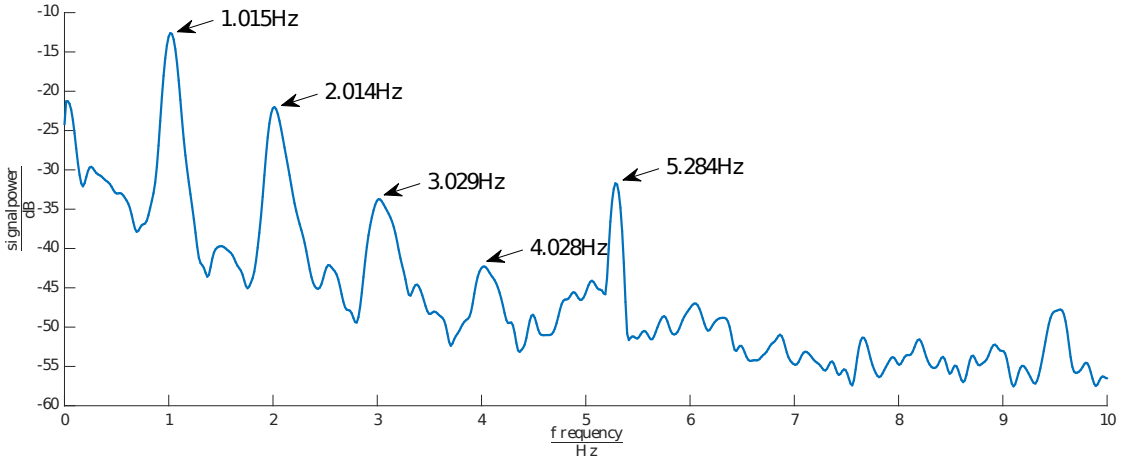

Figure 4.2.: Power spectrum of an unfiltered cardiac independent component. In this volunteer, the fundamental and 4 harmonics are visible.

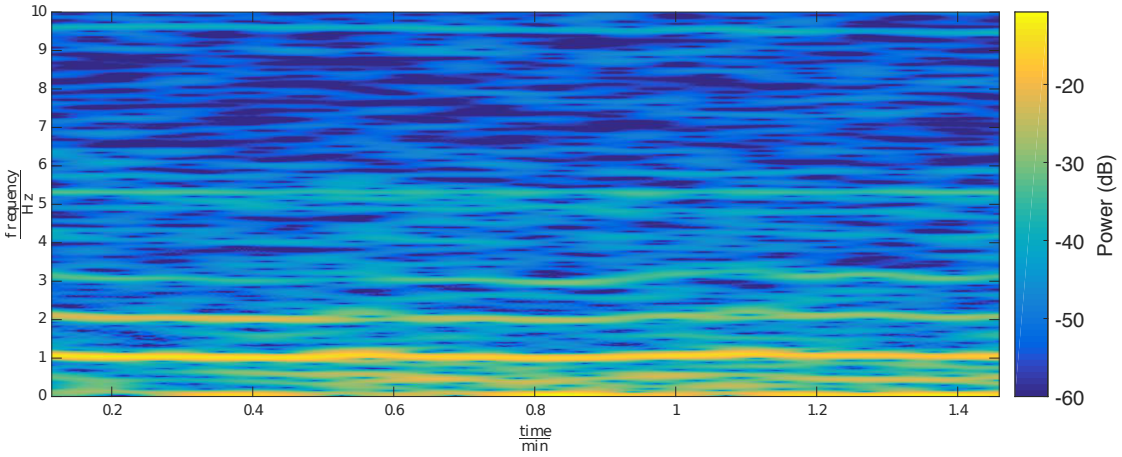

Figure 4.3.: Spectrogram of the same data as in Fig. 4.2, showing the time evolution over approx. 90 s. Fundamental heart rate and four harmonics are visible.

The filtered cardiac IC $s_{PT,f}(t)$ was then numerically differentiated and the maxima of the 1^{st} derivative were identified using Matlab's *findpeak()* function to serve as trigger points $\mathbf{t}_{PT}$.

Figure 4.4 (a) shows a plot of raw- and filtered cardiac IC data and Fig. 4.4 (b) ECG data with triggers and the filtered cardiac IC and its numerical 1^{st} derivative and its maxima.

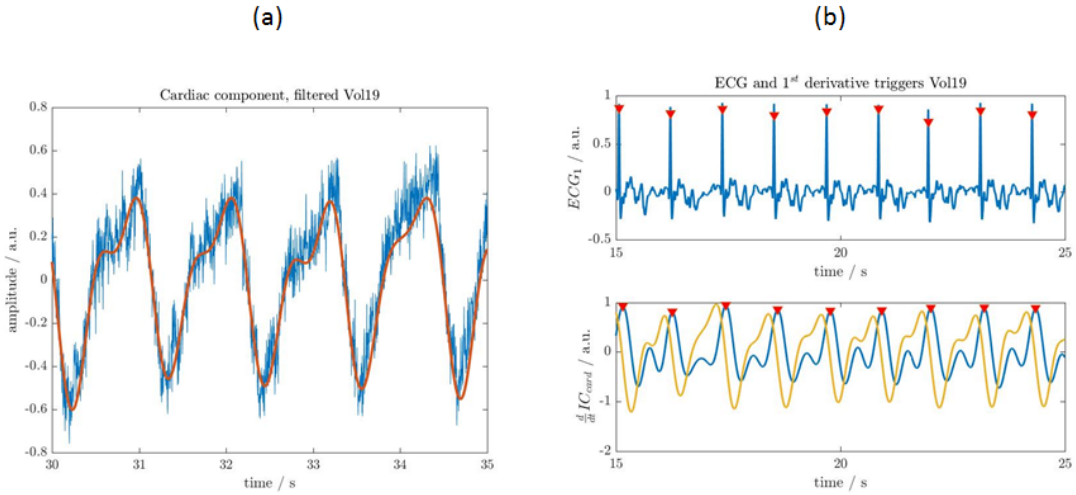

Figure 4.4.: (a) unfiltered (blue) and filtered (orange) cardiac IC over four heartbeats. (b, top) ECG ground truth and R-peak trigger points $\mathbf{t}_{ECG}$ (red triangles). (b, bottom) Filtered cardiac IC (blue) and its 1^{st} derivative $\frac{d}{dt}s_{PT,f}(t)$. Maxima of the negative 1^{st} derivative are marked with red triangles.

The 1^{st} derivative

$$\dot{s}_{PT,f}(t) = \frac{d}{dt}s_{PT,f}(t) \tag{4.5}$$

of $s_{PT,f}$ should, under the assumption that $s_{PT,f}$ represents cardiac volume, correspond to velocity of the cardiac wall. The maximum of $-\dot{s}_{PT,f}$ is then the point of maximum velocity of the cardiac wall, which is reached slightly after the R-peak, which marks the depolarization of the myocard. This means, that $\mathbf{t}_{ECG}$ can not coincide with $\mathbf{t}_{PT}$. The delay $DT[n]$ between time points $\mathbf{t}_{ECG}[n]$ and $\mathbf{t}_{PT}[n]$ should however be relatively constant.

The time delay DT is expected to vary with the volunteers heart rate, therefore DT was calculated in percent of the mean RR-interval $\overline{RR}$:

$$DT[n] = 100\frac{\mathbf{t}_{PT}[n] - \mathbf{t}_{PT}[n]}{\overline{RR}} \tag{4.6}$$

and mean DT

$$\overline{DT} = 100\frac{\langle \mathbf{t}_{PT} - \mathbf{t}_{ECG} \rangle}{\overline{RR}} \tag{4.7}$$

where $\langle \cdot \rangle$ represents the mean of a vector.

Additionally, trigger-jitter j_{PT} (in $\%\overline{RR}$) was defined as $\pm$ one standard-deviation around the mean time-delay $\overline{DT}$, see Fig. 4.5

$$j_{PT} = 2 \cdot 100 \cdot sd\left(\frac{\mathbf{t}_{PT} - \mathbf{t}_{ECG}}{\overline{RR}}\right) \tag{4.8}$$

or in ms as

$$j_{PT} = 2 \cdot sd\left(\mathbf{t}_{PT} - \mathbf{t}_{ECG}\right) \tag{4.9}$$

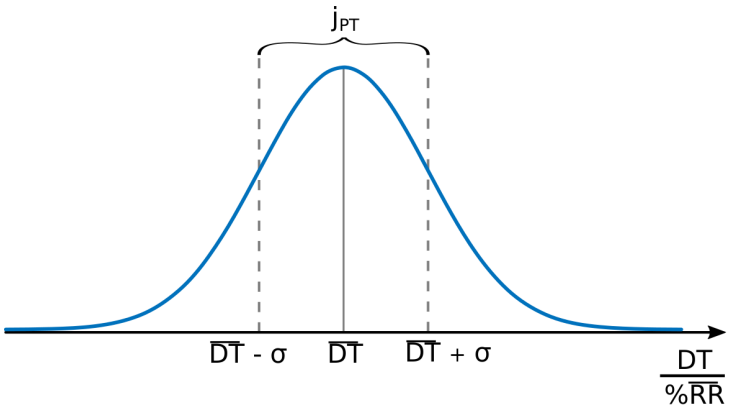

Figure 4.5.: Trigger-jitter j_{PT} is defined as 2 $\pm$ one standard deviation around the mean time difference $\overline{DT}$.

Some trigger-points, either in $\mathbf{t}_{PT}$ or in t_{ECG} might conceivably be wrong. Movement of the volunteer for instance is likely to interfere with the ECG resulting in spurious triggers. This would then result in unrealistically large time delays between $\mathbf{t}_{PT}$ and $\mathbf{t}_{ECG}$. Since mean and standard deviations (i.e. $\overline{DT}$ and j_{PT}) are highly susceptible to outliers, these erroneous measurements need to be removed. An upper threshold $DT[n] > 0.1\,\overline{\mathrm{RR}}$ was arbitrarily chosen, above which $DT[n]$ would be excluded from calculation of $\overline{DT}$ and j_{PT}. The number of outliers was automatically logged for each dataset alongside $\overline{DT}$ and j_{PT}.

This automated analysis was repeated 30 times with randomly varying FastICA initial guesses to quantify whether these slight differences in the estimated demixing matrices have any significant effect on trigger positions and thus $\overline{DT}$.

Analysis of Variances (ANOVA) was performed on $\overline{DT}$ of the repeated ICA realizations to determine whether the stochastic nature of ICA results in significant differences in trigger times.

Finally, Bland-Altman plots [40] were generated comparing absolute trigger times found by ECG and PT.

4.4. Influence of Transmitter Placement

Assuming the transformer-like model of PT signal generation, it is reasonable to assume that the placement of the transmitter with respect to the receiving coils is an important factor. To test robustness against slight variations in transmitter placement, additional measurements were done on one volunteer with the transmitter positioned at eleven different positions and evaluated $\overline{DT}$. ICA was again run 10 times. Transmitter positions are shown in Fig. 4.6, where the circles roughly indicate the position of the transmit loop. Mean time-difference $\overline{TD}$ and trigger-jitter j_{PT} were calculated for all ten realizations of ICA.

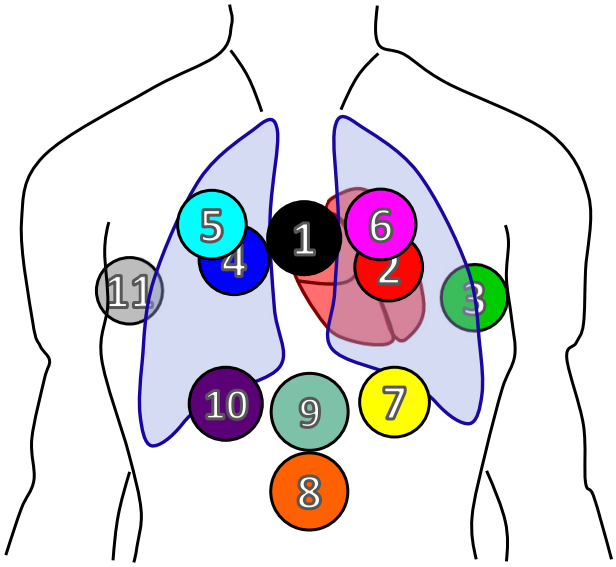

Figure 4.6.: Approximate positions of the PT Transmitter. Positions 11 and 3 are posterior of the volunteer, between the volunteer and the spine array. All other positions are anterior of the volunteer. In positions 4 and 2, the transmitter was placed between the volunteer and the coil array. In all other positions the transmitter was positioned above the coil array.

5. Results

5.1. Modulation Depth

Figure 5.1 shows a histogram of observed modulation depth per channel m_k for real and imaginary components. Median modulation depth was $(4.09 - j1.13)\,\%$

For free-breathing only datasets, median m_k was $(2.96 + j1.08)\,\%$, min: $(0.75 - j0.18)\,\%$ and max: $(83.84 - j12.14)\,\%$. When using magnitude data the median modulation depth was $2.52\,\%$, min: $0.75\,\%$ and max: $82.44\,\%$.

Additionally, median modulation depths for all datasets of free-breathing volunteers were tested for correlation with body mass index (BMI) but no significant correlation was found (real part: $r = 0.176$, imaginary part: $r = 0.176$).

Most subjects were scanned repeatedly during the same session without repositioning of the PT transmitter. Modulation depth varied strongly between repeat scans in some subjects. Figure 5.2 shows boxplots (real and imaginary parts) of intra-subject modulation depths where repeat scans were available.

Clearly, only a small part of the PT signal contributes useful information necessitating highly sensitive receivers.

5.2. Optimized ICA Parameters

Increasing the number of individual components from three to 12 resulted in an increase in both reliability I_r and quality I_q and subsequently I_{qr}. When using

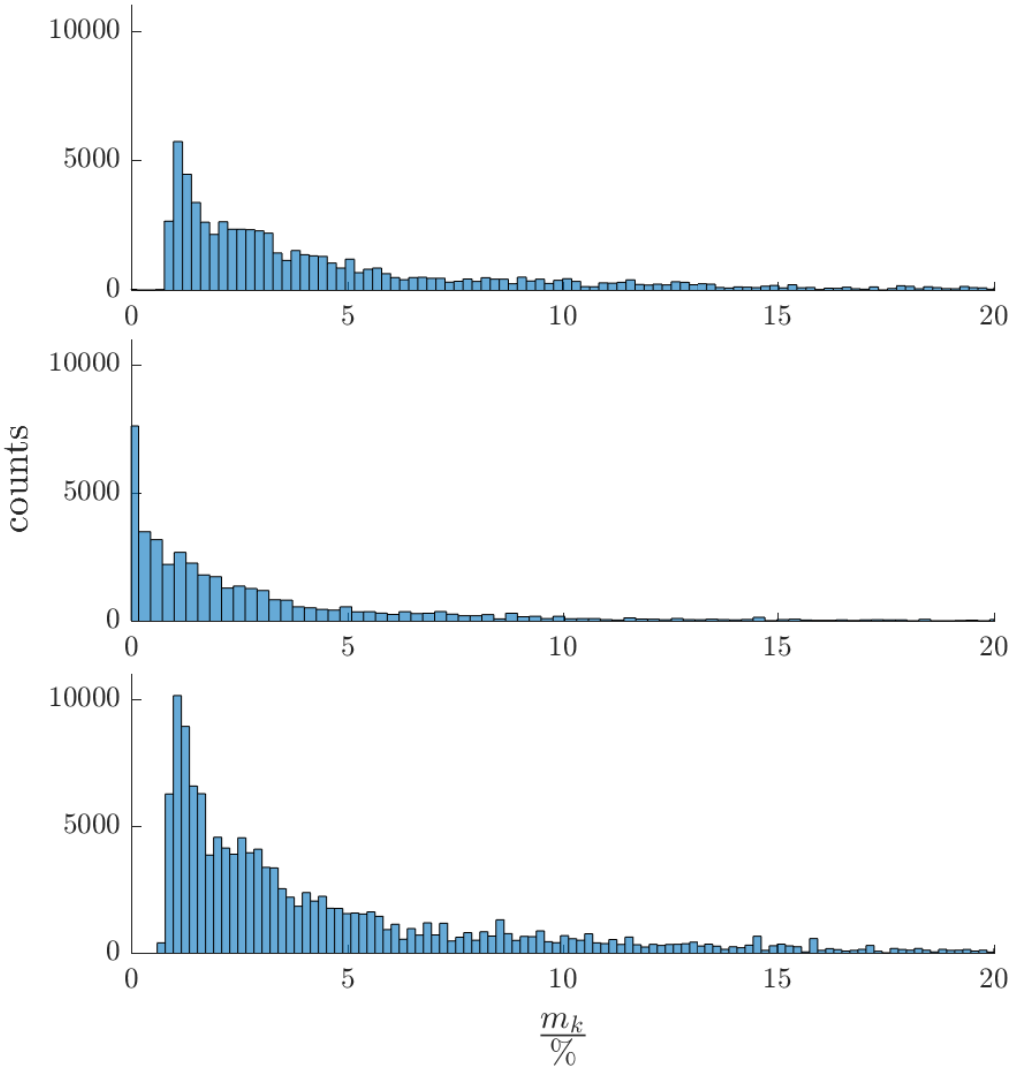

Figure 5.1.: Histograms of real and imaginary parts of the complex modulation depth m_k (top, middle) and m_k when using magnitude PT data. Data come from 119 scans with 34 channels each.

fewer ICs, the reliability tends to decrease heavily: The cardiac component could be found in less than 50% of trials when using seven or fewer ICs. Reliability reached a plateau at approximately 9-12 individual components, achieving an $I_r > 0.9$. Figure 5.3 shows reliability I_r and cluster quality I_q plotted over the number

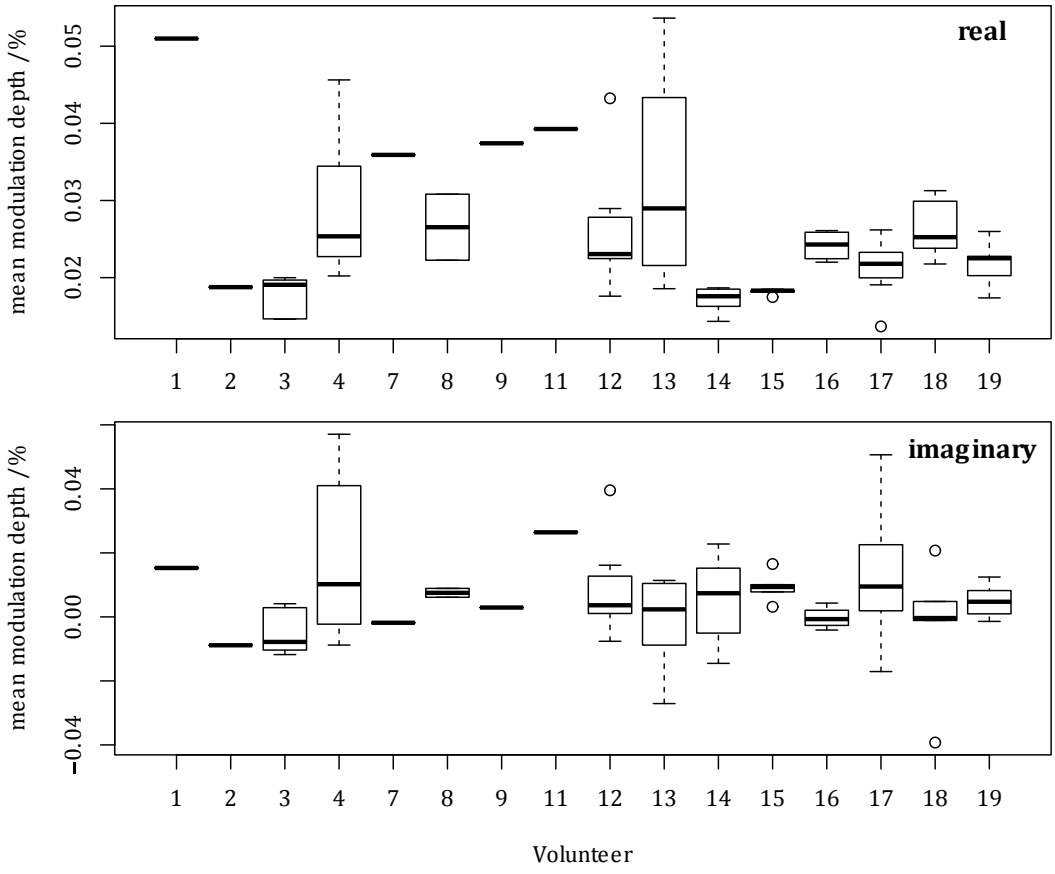

Figure 5.2.: Boxplot of intra-subject variance in modulation depth m_k. Boxes show the distribution of median modulation depth for repeat scans. Where no box is plotted only one scan has been performed. Volunteers were free-breathing for all scans.

of ICs for all algorithm and contrast combinations. In both diagrams, skewness contrast was excluded, as it consistently failed to separate the cardiac component.

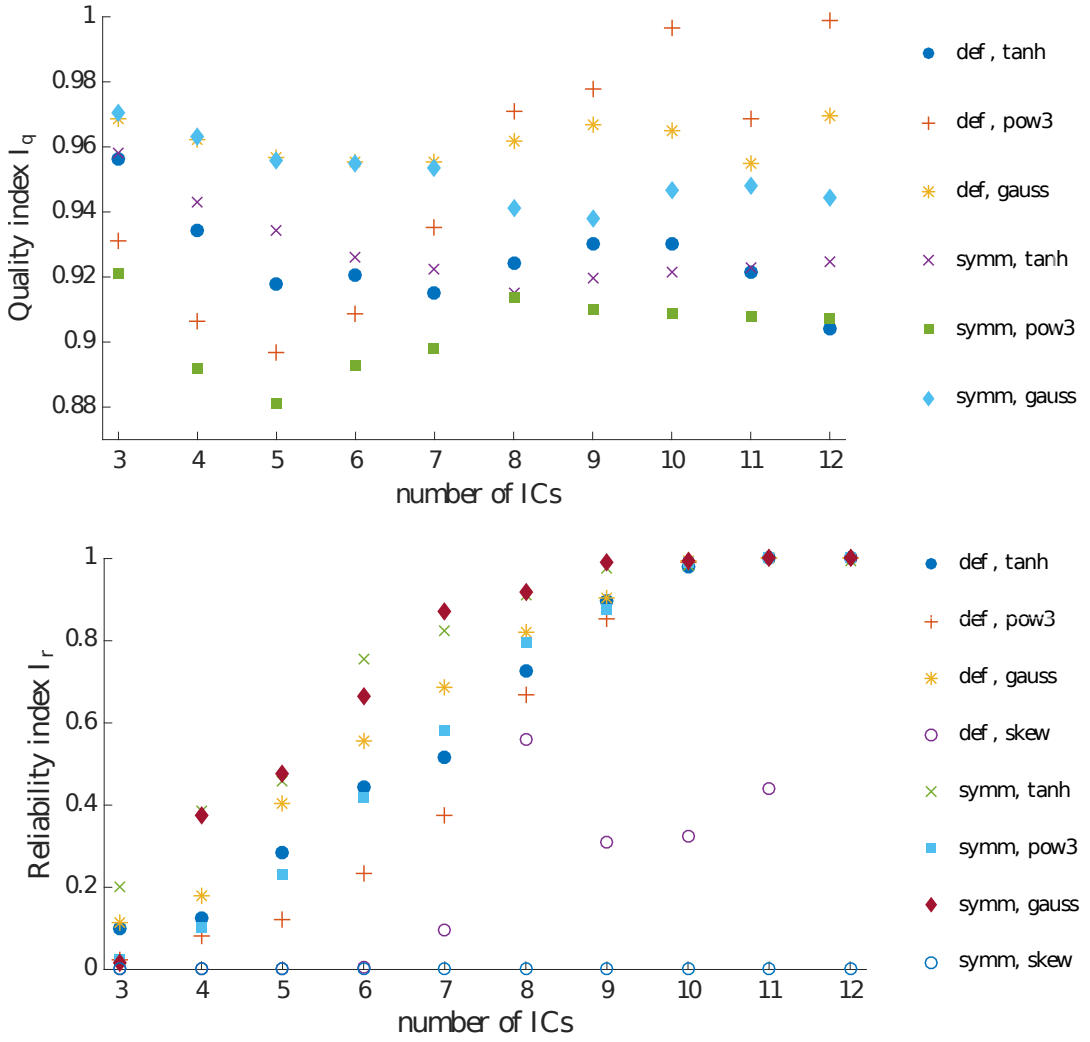

Figure 5.3.: Reliability index I_r and cluster-quality index I_q plotted over the number of ICs used. Note that combinations using skewness as a contrast function are excluded in the I_q plot to improve readability, as those consistently failed to find the independent component associated with cardiac activity ($I_r = 0$).

Cluster quality was high ($I_q > 0.9$) for almost all combinations of algorithm, number of ICs and contrast function, except skewness. However, as mentioned

earlier, cluster-quality tends to increase for less reliable components. Figure 5.4 shows the combined quality- and reliability index I_{qr}.

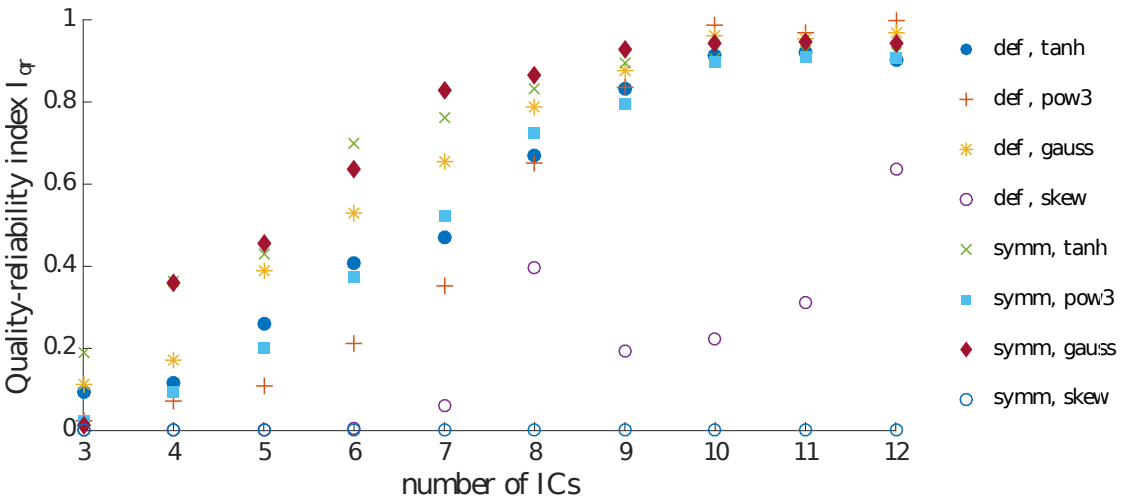

Figure 5.4.: Combined reliability- and quality index I_{qr}.

These results indicate, that the number of ICs should be set to 10-12 for best results.

As for the choice of algorithm, a Wilcoxon Signed-rank test indicated that I_{qr} does not differ significantly (at the $\alpha = 0.01$ significance level) between the symmetric and deflationary approach ($Z = 411, p = 0.3734$).

Following this analysis, the three best performing combinations were then used on free-breathing datasets of all volunteers, using the symmetric estimation approach, to determine whether these parameters perform consistently well over a wide variety of volunteers.

ICA was performed on a total of 67 datasets from 16 free-breathing volunteers using the symmetric algorithm, 12 ICs and three different contrast functions:

- symmetric, tanh, 12 ICs
- symmetric, pow3, 12 ICs
- symmetric, gauss, 12 ICs

The cardiac independent component was again chosen manually and its I_q, I_r and I_{qr} values calculated.

Using the tanh contrast function, the algorithm failed to find the cardiac component in eight of 67 datasets, while using the pow3 and gauss contrasts the algorithm failed twelve and five times, respectively.

To find the overall best performing combination, I_{qr}-values were analyzed statistically to determine whether significant differences in I_{qr} exist. As I_{qr} was not distributed normally, the number of groups was less then five and ICA was ran repeatedly on the same set of volunteers, the non-parametric Quade-test was used. Datasets for which one or more combinations failed to reliably find the cardiac component were excluded (12 datasets total).

Figure 5.5 shows a boxplot representation of I_{qr} values for all three contrast functions used, the histograms for I_{qr} are pictured in Fig. 5.6.

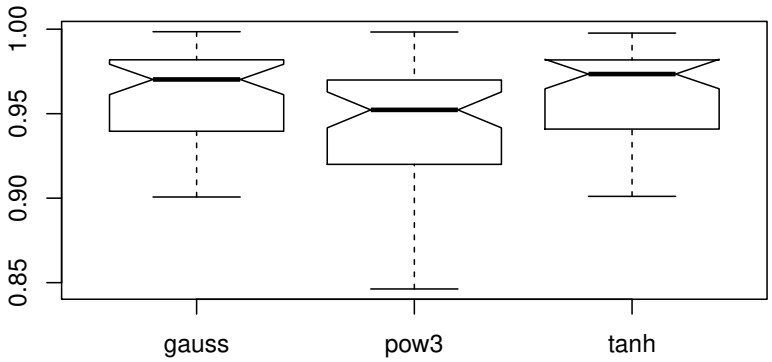

Figure 5.5.: Box-and-whiskers plot of combined reliability- and quality index I_{qr} for different contrast functions. The box ranges from the 1^{st} to the 3^{rd} quartile, i.e. the inter-quartile range IQR. The line represents the median and the notch the medians 95 % confidence interval. Whiskers cover $\pm 1.5IQR$.

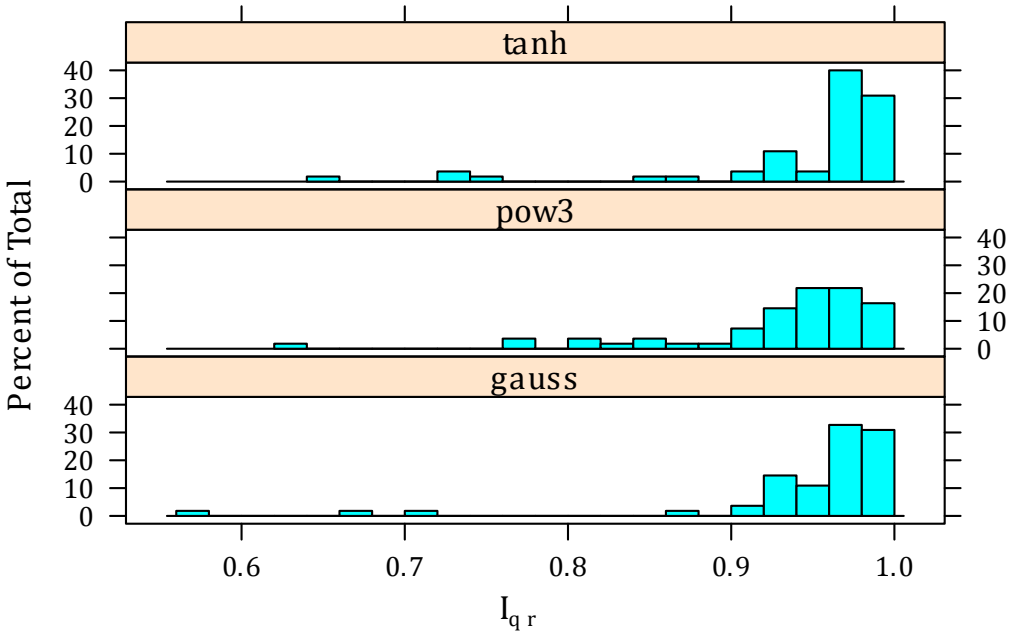

Figure 5.6.: Histograms of reliability- and quality index I_{qr} for different contrast functions.

To determine, whether different contrast functions produce different results, I_{qr} data were tested under the Null-Hypothesis that the distributions of I_{qr} for each contrast are equal.

Quade's test found significant differences between contrasts at the $\alpha = 0.01$ significance level ($F = 6.2421$, $p = 0.00272$), indicating that at least one contrast performs significantly different.

Post-hoc analysis, using Bonferroni correction to account for multiple comparisons, revealed that the tanh and gauss contrasts do not differ significantly from each other in I_{qr}, while the pow3 contrast performs significantly worse.

Therefore, using either tanh or gauss as contrast functions seems to be ideal. Since the gauss contrast failed to find the cardiac IC less often (five times) than tanh, gauss contrast, with 12 ICs and using the symmetric approach was subsequently used for all other experiments in this thesis.

5.3. Comparison of PT & ECG Triggers

Out of a total of 67 datasets from 18 volunteers, six datasets were excluded because FastICA failed to reliably extract the cardiac IC. The automatic selection of the cardiac IC based on signal energy in the $0.8-3$ Hz band correctly chose the correct component in all cases.

The number of missed triggers was low overall: Over repeated runs of FastICA, an average of 0.75 %, sd:1.58 % of ECG triggers were classified as missed triggers under the ($TD[n] > 0.3\overline{RR}$) criterion. In 57 % of all datasets no ECG triggers were missed.

Figure 5.7 shows mean time-delay $\overline{TD}$ plotted against mean R-R interval $\overline{RR}$. Error bars represent the $\pm 1sd$ interval, i.e. trigger jitter. Volunteers are stratified by color. As a visual aid to the viewer, the size of the circles qualitatively shows the percentage of missed triggers.

Mean trigger-jitter j_{PT} was 30.1 ms with a standard-deviation of 5.5 ms or 1.47 %$\overline{\text{RR}}$ with standard-deviation 0.6 %$\overline{\text{RR}}$.

A moderate positive correlation ($r = 0.55, sd : 0.04$) was found between $\overline{TD}$ and $\overline{RR}$, suggesting that TD increases with the R-R interval (intercept: -6.98, $sd : 1.05$ and slope: 14.45, $sd : 1.04$).

To determine whether the stochastic nature of ICA results in significantly different resulting trigger points, ANOVA was performed, testing the null-hypothesis $H_0 : \mu_1 = \mu_2 = \cdots = \mu_n$ where $n = 1 \ldots 30$ are repeated applications of FastICA.

Figure 5.8 show boxplots of $\overline{TD}$ for all 30 realizations of FastICA. Before using ANOVA, the underlying assumptions of normality of the data and homoscedasticity were tested positively at the 0.01 confidence level (Shapiro-Wilk test for normality: $W = 0.95$, $p = 0.014$).

ANOVA found no significant differences in $\overline{TD}$ between ICA realizations at the 0.01 confidence level ($F = 0.09$, $p > 0.01$).

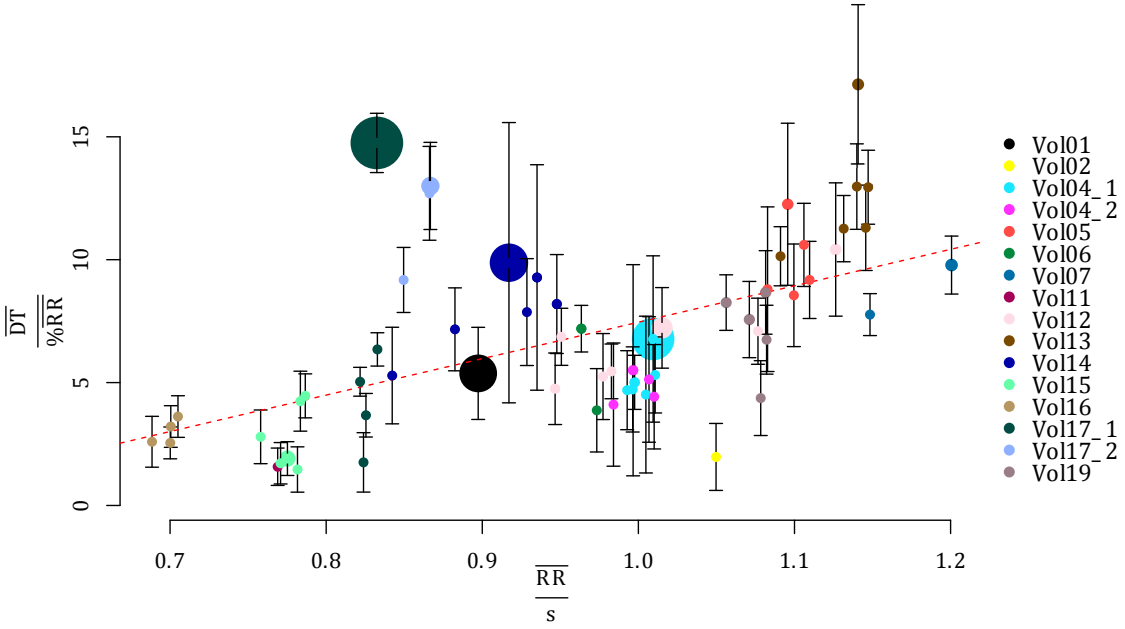

Figure 5.7.: Mean time-delay $\overline{TD}$ plotted against mean R-R interval $\overline{RR}$. Volunteers stratified by color. Error-bars represent trigger jitter and size of circles denotes the percentage of missed triggers. The dotted red line shows a linear fit between $\overline{TD}$ and $\overline{RR}$.

Bland-Altman plots (see Fig. 5.9 for an example) showed good agreement between absolute trigger times found by ECG and PT. According to Bland and Altman, if 95 % of data points fall within the ±1.96 sd interval (sometimes given as ±2 sd) around the mean, variance in the new method (PT) can be explained by variance in the reference method (ECG). The number of triggers outside this interval was, on average, below 5 % (mean: 4.66 %, sd: 1.63 %, min: 0 %, max: 10.11 %). Bland-Altman plots also give a good graphical representation of the (mean) offset $\overline{TD}$ between the two methods under comparison. It is evident from the choice of 1^{st} derivative as trigger point, that such an offset must exist and be positive in relation to the R-peak (see Fig. 5.3). $\overline{TD}$ was found to be 66.3 ms on average (mean: 66.3 ms, sd: 33.0 ms, min: 17.0 ms, max: 169.3 ms). Two measurements had offsets of > 800 ms: Here, the automatic determination of the cardiac ICs sign failed and the measurements were excluded from the analysis.

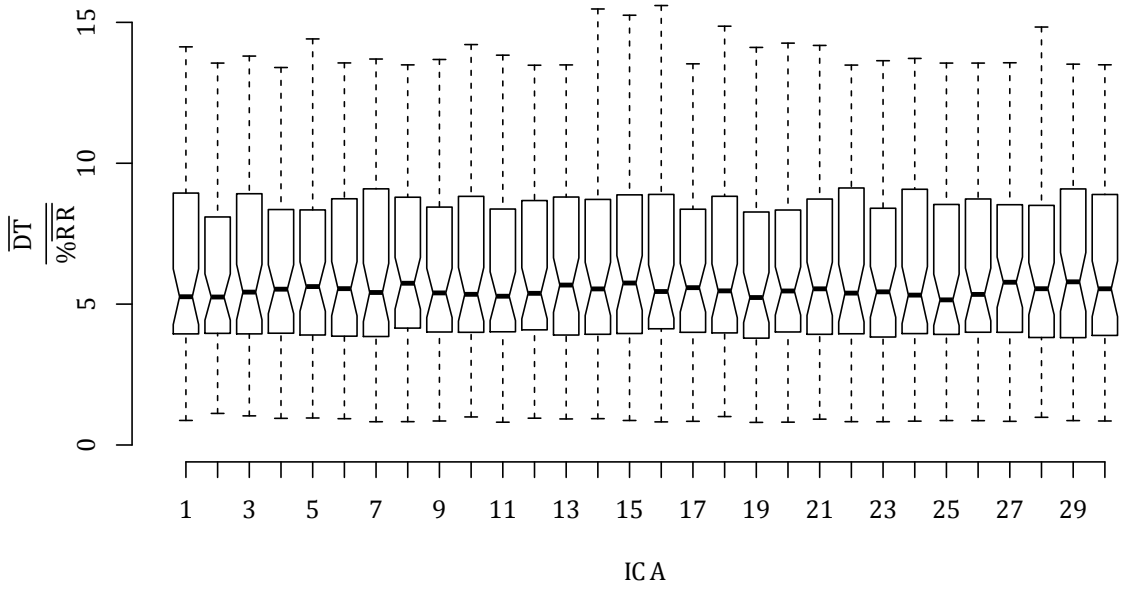

Figure 5.8.: Boxplot of mean time-difference $\overline{TD}$ over 30 realizations of FastICA.

5.4. Influence of Transmitter Position

Figure 5.10 shows a scatterplot of mean time-difference $\overline{TD}$ vs. mean R-R interval $\overline{RR}$. Positions are stratified by color and the ± 1 sd interval (trigger-jitter j_{PT} is plotted as error bars.

Tight clustering of ICA realizations and low trigger-jitter are taken as indication for good positions of the PT transmitter. Overall, positions 2 (red, anterior to the volunteers heart and positioned between the thorax and the coil array) and 6 (pink, anterior to the volunteers heart and positioned on the coil array) produced the best results, i.e. low j_{PT} and tight clustering of results from repeated ICA. Quality decreases when the transmitter is positioned farther away from the heart. The linear relation between $\overline{TD}$ and $\overline{RR}$ found in Sec. 5.3 is plotted as a dashed red line. For positions 8, 9 and 10 the FastICA algorithm failed to converge reliably or results were too polluted by respiratory and other components.

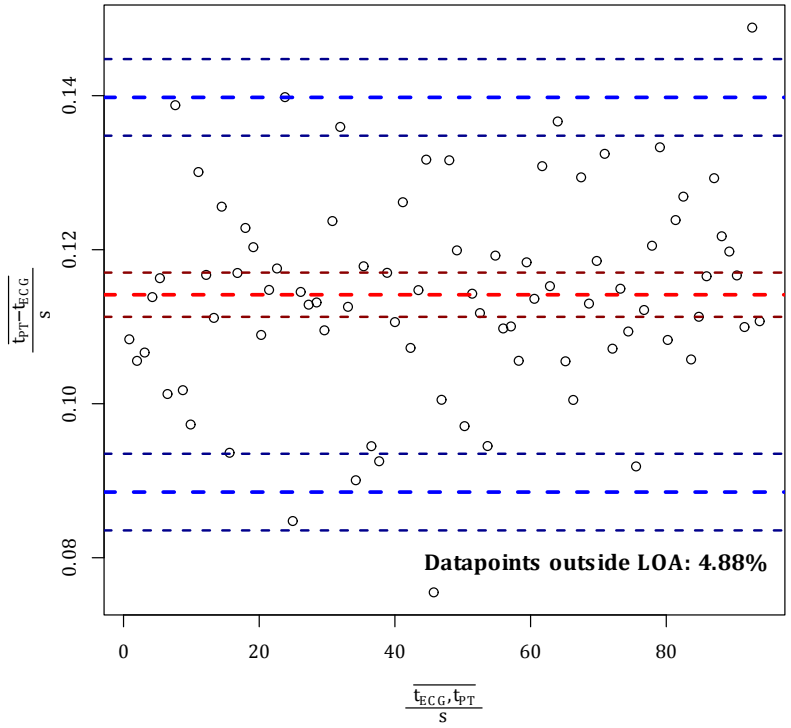

Figure 5.9.: Exemplary Bland-Altman comparing the difference between methods (y-axis) to the mean of both methods (x-axis) . Dashedred and blue lines show mean and ±1.96 sd limits of agreement and their respective 95 % confidence intervals.

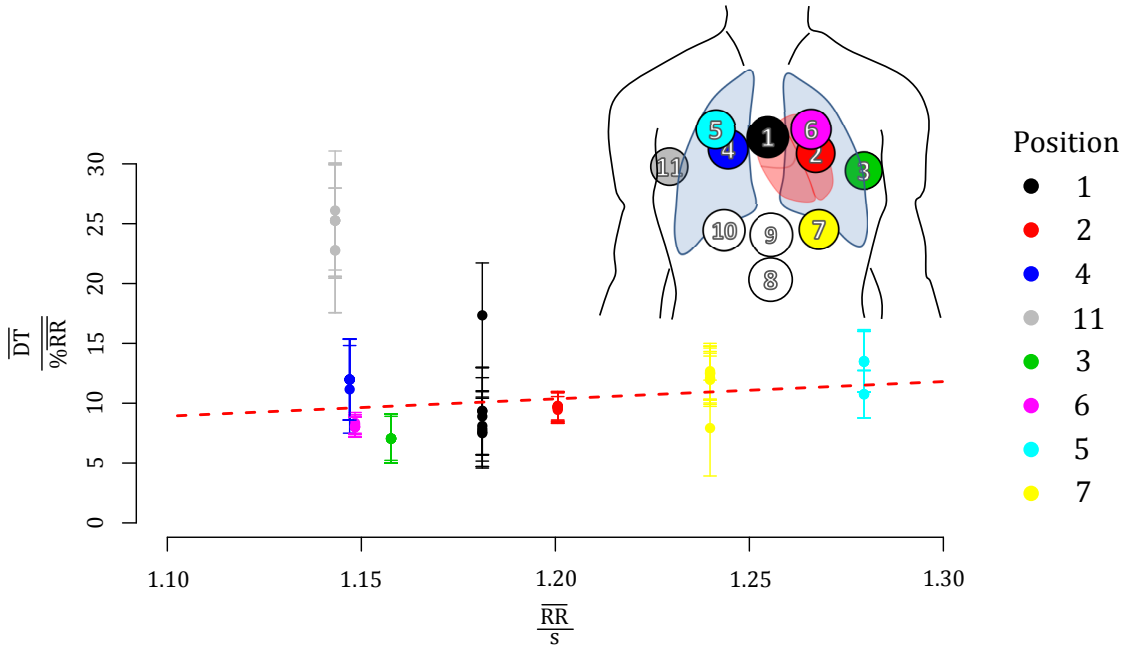

Figure 5.10.: Scatterplot of $\overline{TD}$ vs. $\overline{RR}$. Error-bars depict the ± 1 sd interval (trigger-jitter). Each dataset was reconstructed several times using randomized FastICA starting-guesses. The dashed red line shows the linear relationship between $\overline{TD}$ and $\overline{RR}$ found in section 5.3.

6. Discussion & Outlook

The goal of this thesis was to evaluate whether cardiac triggering based on the PilotTone navigator would be a feasible alternative to ECG based triggering. To this end, a variety of methods from different fields were used. This section shall attempt to combine these results and to determine whether PT navigation is a feasible technique in practical applications.

Since PT navigation is a new method, a processing framework had to be developed that enables reliable extraction of cardiac motion data. In this thesis, several methods of analysis were used, each contributing a piece of a broader picture.

1. Determining the modulation depth, i.e. the fraction of the total PT signal carrying physiological motion information is an important parameter as it defines the requirements on the receiver.

2. Independent component analysis has been shown to be a viable approach to separation of the cardiac signal. However, ICA itself is a relatively new technique and still actively being researched. Being stochastic in nature, validation of components found by ICA is a challenging task. In Sec. 4.2, Monte-Carlo like procedures were used to evaluate the reliability and quality of components found under different ICA parameters and randomized starting conditions. While by no means exhaustive, this analysis resulted in a set of ICA parameters that achieved reliable, high quality separation of the cardiac component. The results obtained from this experiment (Sec. 5.2) were then used in all following experiments.

3. In Sec. 4.3, triggers obtained from PT and ECG are compared. The PT trigger was chosen as maximum velocity of cardiac motion. Statistical hypothesis-testing and Bland-Altman plots were used to determine how well triggers derived from the PT signal correspond to those from ECG. In evaluating the agreement of PT triggers with those obtained from ECG, the challenge was that triggers from PT navigation and those from ECG are based on two separate but strongly linked processes: PT navigation essentially measures mechanical activity whereas ECG measures electrical activity. This necessarily results in a delay between PT and ECG triggers. This delay was found to be non-constant. Possible causes for this shall be discussed in Sec. 6.3.

4. The statistical methods used in Sec. 4.3 were also used in Sec. 4.4 to determine the methods sensitivity to variations in transmitter placement. To be a feasible alternative to ECG, PT navigation must also be easy to use in clinical practice. In Sec. 4.4 PT navigation was found to be relatively robust against variations in transmitter placement.

Independent Component Analysis is still under active research and a multitude of enhancements to the basic FastICA algorithm used in this thesis have been proposed. For a comprehensive review of new developments in the field of ICA see e.g. Hyvärinen [29], Girolami [19] and Bingham et al. [7]. Some of these might offer further improvements and are discussed briefly in this chapter.

Finally, while the results in this thesis were obtained from retrospective evaluations, real-time processing is of prime importance if the PT navigator is to be used as a means of triggering cardiac MRI sequences. Some preliminary results of real-time processing the PT data are shown in Sec. 6.5.

6.1. Modulation depth

Modulation depth varied strongly between channels but does not seem to correlate with BMI. This indicates that even in more massive volunteers PT signal penetration was sufficient for reliable reconstruction of the PT navigator. The higher median m_k observed when considering all datasets can easily be explained by the fact that for 52 of the 119 datasets volunteers were asked to repeatedly perform breath-holds during the 90 s acquisition. This stronger peak inhalation volume resulted in increased modulation depth. Curiously, in three datasets modulation depths of $m_k > 100\,\%$ where observed in one channel each. Upon further inspection of these channels, the PT signal was found to exhibit strong drift in the offset, going from positive to negative (or vice versa) over the duration of the acquisition, the cause of which could not be determined.

In general, modulation depth was not equal in the real and imaginary component. It has been observed, that the complex PT signal in most channels is non-circular and improper. A circular complex random variable has a probability distribution that is invariant to rotation in the complex plane, i.e. a circular disc:

$$\mathbf{X} \overset{d}{=} \mathbf{X}e^{j\theta} \quad \forall\theta \tag{6.1}$$

Additionaly, a complex random variable is considered proper, if its pseudo-covariance vanishes, that is

$$\mathrm{E}\{\mathbf{X}^2\} = \mathrm{E}\{\mathbf{X}_r^2 - \mathbf{X}_i^2 + 2j\,\mathrm{E}(\mathbf{X}_i\mathbf{X}_r)\} = 0 \tag{6.2}$$

where subscripts r and i denote real- and imaginary parts respectively. Note that circularity implies propriety, but not vice versa and impropriety implies non-circularity, but not vice versa [3].

In many algorithms for processing of complex data circularity and/or propriety are implicitly assumed. While these assumptions are conveniant, as they simplify

computation, Adah et al. [3] claim that, at least in some cases, exploitation of non-circularity and impropriety can greatly improve performance of statistical signal processing. However, the existence of non-circularity and impropriety does not necessarily mean that the complex signals phase is informative, i.e. offers additional, physiologically relevant information. Some preliminary experiments using complex raw data and the complex-valued JADE [10] ICA algorithm did not result in significant improvements. Additionally, complex ICA is computationally more expensive than real-valued ICA using e.g. FastICA.

6.2. Optimized ICA Parameters

The results in chapter 5, section 5.2 show that the quality and reliability of source separation is largely dependent on the proper choice of contrast function and the number of assumed independent components. In this thesis, FastICA default contrast functions were used but in principle one is free to choose any non-quadratic function $G(y)$ as contrast. Recall Eq. 3.22, the approximation of negentropy used as an objective function in FastICA

$$J(y_i) \propto c\,[\mathrm{E}\{G(y_i)\} - \mathrm{E}\{G(v)\}]^2 \tag{6.3}$$

where $g(y) = G'(y)$ is the contrast function, c is some constant, v is a zero-mean gaussian variable with unit variance and $\mathrm{E}\{\cdot\}$ denotes expectancy. It is clear from Eq. 6.3, that a hypothetical (zero-mean) gaussian component y_1 would lead to $J(y_i) = 0$. Since the goal of FastICA is to maximize negentropy $J(y_i)$, a good contrast function thus transforms y_i such that it is as "non-gaussian" as possible.

In Fig. 6.1 the pdf of a typical cardiac IC signal is shown (top) together with its pdf after transformation with several contrast functions.

This example also demonstrates, why the skew contrast repeatedly failed to find the cardiac component: Under skew contrast, the PDF appears to be closer to zero-mean gaussian than before transformation, leading to very low $J(y_i)$.

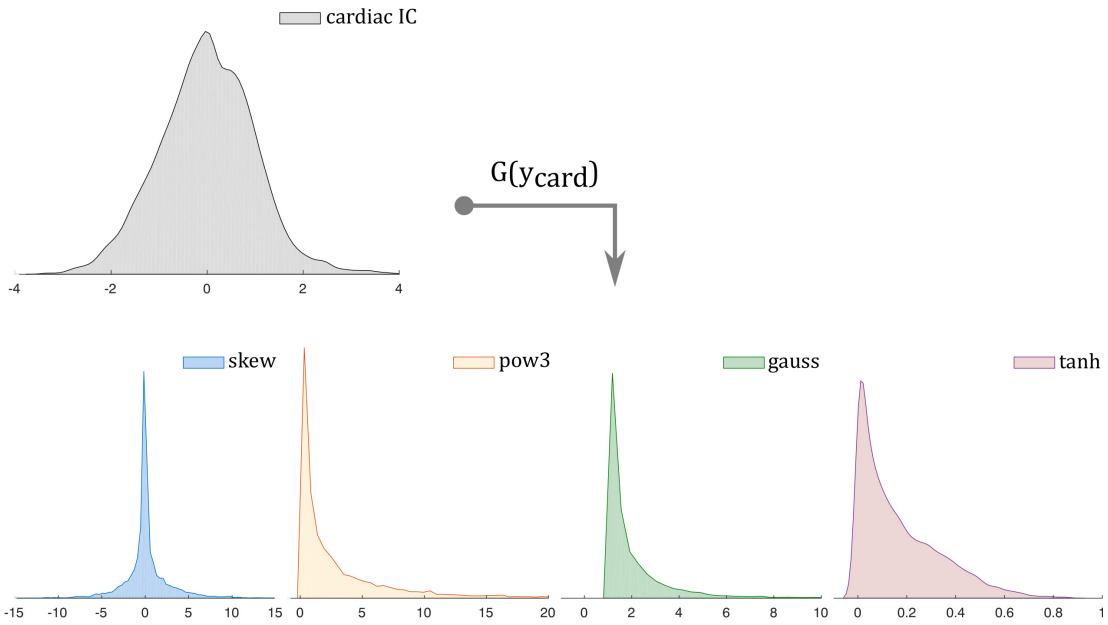

Figure 6.1.: Top: PDF of the cardiac component (Volunteer 01). Bottom: PDFs of of the cardiac component under transformation by $G(y_{card})$. PDFs were obtained by Kernel Density Estimation using a gaussian kernel.

Other implementations of ICA are based not on negentropy but use e.g. kurtosis as objective function - using such an algorithms, skew contrast might perform significantly better, as it produces a highly leptokurtic PDF.

Independent component analysis has so far primarily been used as a exploratory data analysis tool and the contrast functions used in this thesis have been found to produce good results in a wide variety of applications (CITE). In the context of PT navigation however, at least the basic shape of the cardiac signal is known a priori. It therefore seems reasonable that a contrast function can be found that is optimized to this particular application. In the literature, optimized contrast functions have been suggested in recent years for diverse applications, such as e.g. twin fetal ECG [34], functional magnetic resonance imaging (fMRI) [58] and image processing [4, 38].

Another aspect that might significantly improve ICA performance is continuous updates of the demixing matrix. Currently, ICA is being computed once after a short training period. It is reasonable to assume that the obtained demixing matrix is primarily a representation of the underlying geometry and the subjects anatomy, i.e. the relative position of the PT transmitter and receive coils and the subjects body composition. Both are non-stationary in practice, especially in free-breathing exams where the respiratory movement of the chest wall also moves the PT transmitter relative to the receive coils in the spine array. Any demixing matrix calculated from a free-breathing training set can thus only be a kind of "mean-demixing" matrix, representing the average coil geometry and respiratory state. While this has been shown to be sufficient for robust and reliable separation of the cardiac component, some respiratory can often be identified in the cardiac IC resulting in low-frequency offset. Non-stationary ICA, wherein the mixing matrix is allowed to vary over time, has been actively researched in recent years and several solutions to the problem have been proposed, implemented using e.g. a sliding window approach [21, 27], recursive algorithms [25] or using particle filters [19].

It is somewhat surprising that the ideal number of independent components to search for is between $10 - 12$ ICs. Respiratory motion accounts for two individual components. Schroeder et al. have demonstrated that the respiratory information contained in the PT signal can be separated into anterior-posterior and superior-inferior components [61], but the splitting of respiratory motion as found by ICA could also represent a separation of motion of the lungs and liver.

This however leaves $7-9$ ICs of unknown origin. One additional component should, in theory, be mostly gaussian noise as ICA is capable of finding exactly one component that is gaussian distributed. Some of the remaining components may possibly be attributed to gradient switching and other sources of imperfections in the measurement chain. If this assumptions holds, the number of components found by ICA should be reduced when measuring just the PT signal without any concurrent imaging.

Finally, the ICA problem is essentially a non-convex optimization problem. This means, that there are several local maxima/minima in which the solver can get stuck. For instance, the sign of each component is indeterminate in the ICA model and two maxima exist, one for positive and one for negative sign. Especially the symmetric algorithm could often be observed continuously switching the sign of some components, essentially ping-ponging between two equally good solutions. This case can easily be prevented by either stopping after a predefined number of iterations or by using some algorithm for step size selection such as randomized step sizes (stochastic gradient descent).

The more problematic case is when the solver runs into a local minimum/maximum, resulting in an imperfect solution to the demixing matrix. Selection of a good contrast function should help to alleviate this problem to some extent, but in the absence of some a-priori knowledge about the demixing matrix, a small chance remains that the randomized starting guess is too far from the global maximum to achieve convergence. Assuming, as in the discussion above, that the demixing matrix is mostly determined by geometry and underlying anatomy, it seems feasible that some initial guess can be found that is, on average, closer to the global solution than a purely randomized initial guess.

6.2.1. A Note on Convergence of the FastICA Algorithm

To the authors knowledge, global convergence of the FastICA algorithm has not been proven for the general case. For some special cases only, global convergence has been proven theoretically, see e.g. Oja & Yuan [47] for the case of pow3 contrast function and infinite samples. However, the FastICA algorithm has been used extensively and global convergence is known to be quite good [64]. Tichavsky et al. [64] found failure rates of $0.01-1\,\%$ when running FastICA repeatedly 10.000 times using randomized initial conditions, depending on model dimension, stopping criterion and data-length. They also found that in most cases, failure to converge was due to the algorithm getting stuck at a saddle point lying approximately halfway between two solutions. They propose an improved version of FastICA

where a check for saddle points is performed and, if one is found, one or two additional iterations are performed. Using this improved algorithm, they found failure rates to be approaching zero, except for very short input data. In this thesis, the complete acquisition (approx. 90 s) were used for training, but preliminary results using a real-time capable prototype show that some $2-3$ heartbeats are sufficient for solving the ICA problem. As the PT signal is always active, this training data can, in practical applications, easily be recorded during the imagers calibration phase, thus incurring no time penalty on total examination-time.

6.3. Cardiac IC vs. ECG

In general, trigger points could be reliably extracted from the PilotTone signal and showed a high degree of correlation to those extracted from ECG. These results indicate, that triggering and/or gating using the PilotTone navigator is feasible and should lead to results comparable to using ECG. When running ICA repeatedly on the same data, the algorithm tended to converge to the same solution with only rare cases were the cardiac IC was not reliably estimated. Since the basic shape of the cardiac IC is known a-priori, these cases should be easy to detect in practice and ICA can be run again, possibly with adapted parameters.

However, the approach used herein for validating PT to ECG triggers may not be entirely precise. One fundamental challenge in comparing trigger points obtained from PT to those from ECG is that while ECG measures the electrical activity of the heart, PT data must be assumed to be a representation of the hearts mechanical state. The electrical and mechanical activity are intricately linked, each feeding back to the other on a cellular level. This mechano-electrical feedback is mediated by factors such as stretch-dependent Ca^{2+}-channels [65]. It is a well established fact in the field of numerical cardiac modeling that simply solving the electrical problem and then feeding results to the mechanical model is insufficient to capture the intricacies of cardiac activity. Instead, multiphysics, multiscale coupled

electromechanical models are necessary. See e.g. Trayanova and Rice [65] for an excellent overview of cardiac electromechanics in a numerical modeling context.

The ECG QRS complex marks the beginning of the ventricular systole, i.e. depolarization of ventricular cells. In MRI, the R peak is used for triggering as it is usually the only feature that can be reliably identified. In this thesis, the minimum of the 1^{st} derivative of the pilot tone signal s_{PT} was used because it is close to the R-peak and easy to compute. Mechanically it marks the point of maximum velocity of myocardial contraction, assuming that s_{PT} indeed is representative of cardiac volume. It is therefore not surprising that PT trigger points, i.e. maximum velocity of contraction, lag behind those obtained from ECG by some $30 - 100\,\text{ms}$. This time difference $\overline{TD}$ was found to be moderately correlated to the mean R-R interval $\overline{RR}$. This result seems reasonable, as both systolic and diastolic time intervals were previously found to be dependent on heart-rate [11, 35, 41].

Lance et al. [35] found left ventricular ejection time (LVET) (see Fig. 6.2) to be strongly correlated to heart-rate. Mertens et al. [41] later demonstrated that also the electromechanic systole, i.e. the Q-S_2 interval defined as starting with the Q-wave and ending with the onset of the aortic component of the second heart-sound (S2), shortens with $\overline{RR}$. As the PT trigger lies in the first half of the electromechanic systole, it can be expected to also exhibit this behavior. Furthermore, Gurev et al. [22] evaluated electro-mechanical delays in a electro-mechanically linked numerical model of a rabbit's heart. Their results agree well with experimental data and show that electro-mechanical delay (EMD), i.e. the delay between local depolarization of myocytes and the onset of myocyte shortening, changes with pacing and mechanical preload and is in the range of $25 - 40\,\text{ms}$. Constantino et al. [13] found similar results in a computational study using a electromechanically coupled numerical model of a canine heart. Both groups also found electromechanical delay to be spatially varying [13, 22]. Figure 6.3 [13] shows 3D maps of electrical activation, mechanical activation and electromechanical delay in canine ventricular models. Neither group mentiones how this translates to humans, but rabbits are

often used as transgenic model to the human heart [39], even though they have much higher heart-rate ($R - R \approx 300\,\text{ms}$).

In humans, Provost et al. [54] measured the electromechanical wavefront using electromechanic wave imaging (EWI), a relatively new, ultrasound-based imaging technique. 2D ultrasound CINE movies provided by the authors show the propagation of the electromechanic wavefront together with the ECG. From these movies, the time from R-peak to onset of contraction was found to be around 20 ms in two healthy volunteers whereas $\overline{TD}$ (R-peak to peak velocity of contraction) was $63 \pm 26\,\text{ms}$. Furthermore, Brookes at al. confirmed that measures of cardiac contractile function are subject to beat-to-beat variances [9]. In summary, while this does not completely rule out the possibility that the observed trigger-jitter j_{PT} (on average $\overline{TD} \pm 15\,\text{ms}$) and time-delay $\overline{DT}$ come from systematic problems with the PT method, it nevertheless strongly suggests that at least part of this variation is well explained by physiological processes.

6.4. Influence of Transmitter Placement

Overall, positions 2 (red) and 6 (purple) seem to be preferable. Notably, having the coil array as an additional barrier between the transmitter and the coils posterior to the volunteer does not appear to compromise separation or trigger quality. This increases patient comfort and ease of use, as the transmitter need not be wedged between the volunteer and coil array but can instead easily be affixed to the coil array. Positions 3 (green), 4 (blue), 5 (turquoise) could still be considered adequate. Position 1 (black), while still close to the heart seems to be less reliable, possibly because in this position the transmitter is very close to the electronics box of the used Body 18 coil which might distort the magnetic field.

Mean time-delay seems to increase with distance of the transmitter from the heart, but the volunteers mean R-R interval increased during the scan session and the observed increase in $\overline{DT}$ might also, at least in part, be explained by the linear

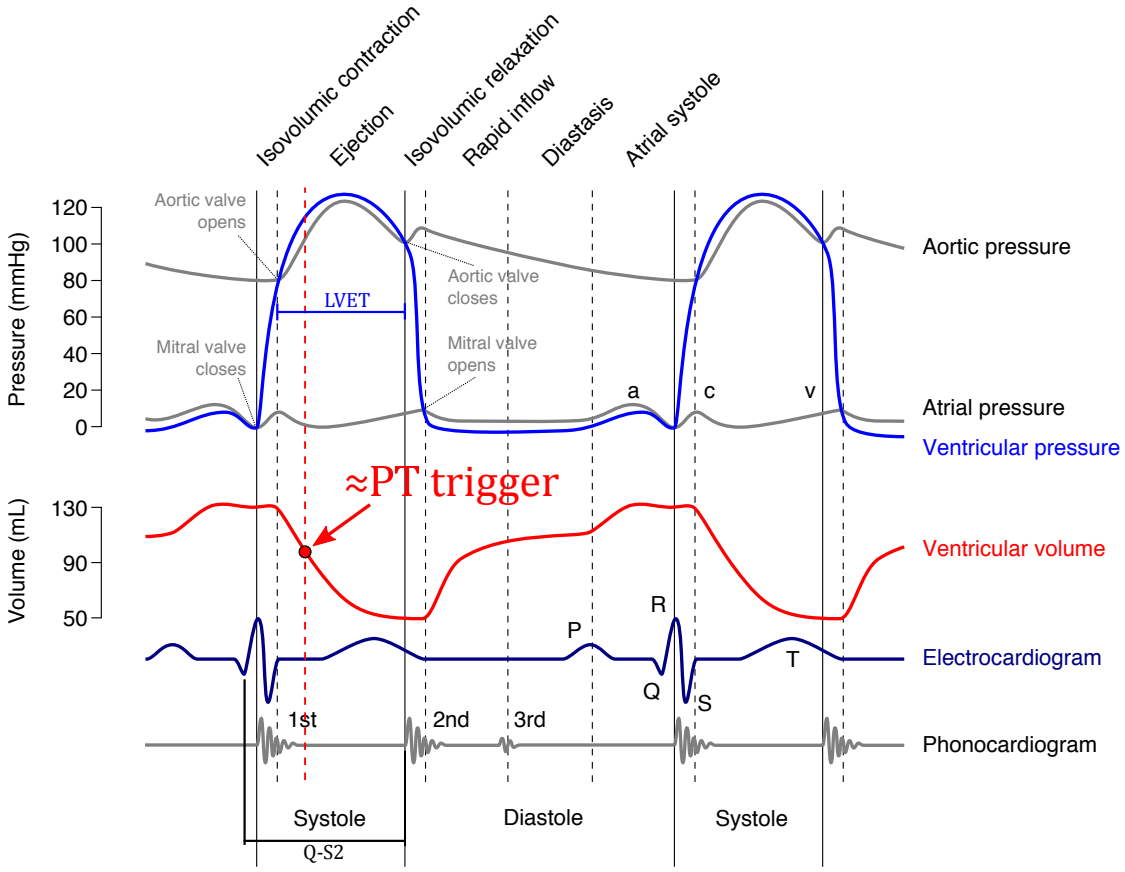

Figure 6.2.: Wiggers Diagram showing aortic, atrial and ventricular pressure, ventricular volume, electrocardiogram and phonocardiogram over time. The approximate position of the PT 1^{st}-derivative trigger has been marked in red. Modified from: `https://commons.wikimedia.org/wiki/File:Wiggers_Diagram.svg`

relation between $\overline{DT}$ and $\overline{RR}$ observed in Sec. 5.3, plotted as a dashed red line in Fig. 5.10.

These results indicate, that the position of the transmitter should be chosen approximately anterior to the heart but allows for some imprecision in placement while still producing reliable separation and triggering.

Crucially, the location dependent delay in the cardiac signal observed by Pfanner et al. [52] at 869 MHz was not observed. Two factors might contribute to this: Firstly,

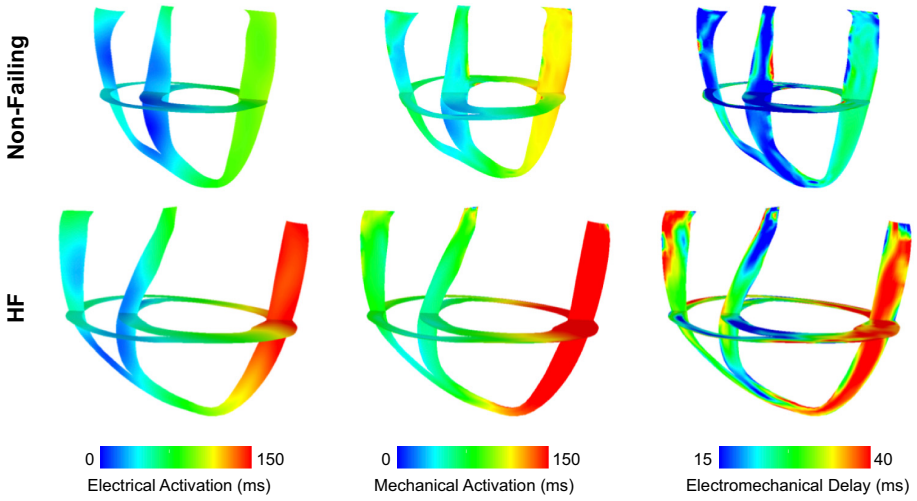

Figure 6.3.: Electrical activation times (left), mechanical actvation times (middle) and electromechanical-delay (EMD, right) maps in dyssynchronous non-failing (top) and dyssynchronous heart-failure (bottom) canine ventricular models. Figure from Constantino et. al [13].

the frequency used for PT navigation is much lower, ranging from 64 MHz at 1.5 T to 298 MHz at 7 T. This results in much lower spatial resolution. Secondly, ICA would not be able to separate two components that are similar in waveform but delayed as their respective PDFs would be almost identical. Both effects result in a kind of "averaging" that is expected to smooth out such minor differences and produce a robust estimate of total cardiac volume. As wavelength decreases with increasing frequency, it will be interesting to see wether this would becomes problematic at higher field strengths, which would require the pilot tone to be of higher frequency, e.g. 294 MHz at 7 T.

6.5. Real-time processing

So far, all analyses in this thesis have been performed retrospectively, i.e. using time-domain digital filtering to eliminate noise in the PT signal. While some

applications may benefit from PT data evaluated retrospectively, to be a viable alternative to ECG-based triggering the PT signal needs to be processed in real-time. For cardiac applications, the effective PT sampling-rate, determined by echo-spacing is expected to be approximately in the $200-400\,\mathrm{Hz}$ range while the cardiac signal is in the range of $0.65-12\,\mathrm{Hz}$ (assuming heart-rates from $45-180\,\mathrm{bpm}$, including two harmonics). Thus, extremely narrow-band filters would be necessary. This is problematic for realtime applications as such powerful filters have a group delay of several hundred samples.

Consider the following filter:

- Type: FIR Lowpass
- Sampling frequency: $f_s = 360\,\mathrm{Hz}$
- Passband frequency: $f_{pass} = 6\,\mathrm{Hz}$
- Stopband frequency: $f_{stop} = 8\,\mathrm{Hz}$
- Stopband attenuation: $60\,\mathrm{dB}$
- Design: Equiripple

Trying to meet these criteria results in a FIR filter of order 356 which has a group delay of 178 samples - 0.5 s at $f_s = 360\,\mathrm{Hz}$ or half a heartbeat. Infinite-impulse-response (IIR) filters can be designed with significantly shorter group-delay using modern filter design techniques but will have non-constant group delay. Figure 6.4 shows the group-delay of an IIR filter equivalent to the one above designed in Matlab using the constrained least P^{th}-norm algorithm [6]. For a cardiac signal with a heart rate of 1 bpm, the group delay would be between 25 and 30 samples or $69-83\,\mathrm{ms}$ while still performing relatively poorly (see insert in Fig. 6.4).

This chapter shall give a short outlook on the steps needed to enable real-time processing of the PT signal following extraction of the cardiac independent component using ICA showing some promising preliminary results not included in this thesis due to time constraints.

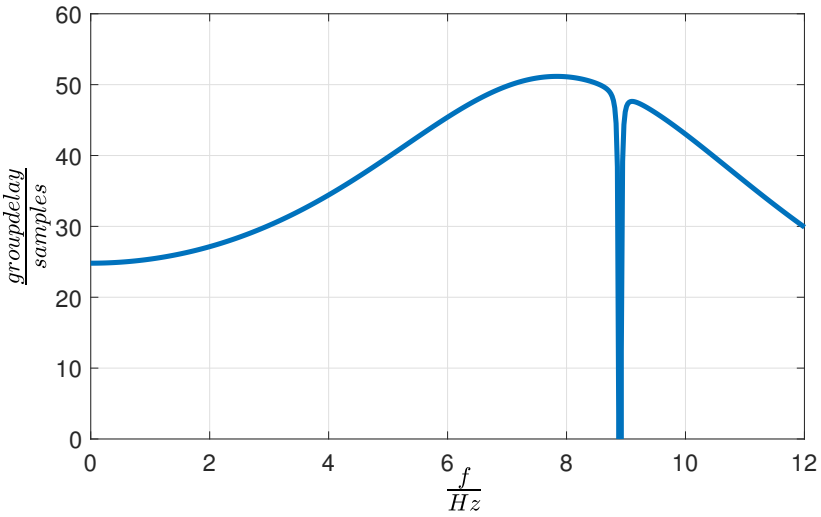

Figure 6.4.: Frequency dependent group-delay of an IIR lowpass filter. Passband: $f_{pass} = 6\,\text{Hz}$, stopband: $f_{pass} = 8\,\text{Hz}$, Stopband attenuation: $60\,\text{dB}$. Designed using the constrained least P^{th}-norm algorithm.

Recall Figs. 4.2 and 4.3, showing the power-spectrum and time resolved spectrogram of a typical cardiac independent component: The fundamental frequency (heart-rate) and some, typically two to four, harmonics can be identified. Furthermore, heartbeat is predominantly quasi-periodic [14]. This probabilistic component is reflected in the broadening of spectral peaks, owing to variance in heart-rate.

This suggests, that a simple, phenomenological model of the cardiac component can be constructed by synthesis in the frequency domain, such that

$$\hat{s}_{PT} = c_0(t) + \sum_{k=0}^{K} a_k(t) \sin(k\omega(t)t + \Theta_k) \tag{6.4}$$

where K is the number of peaks included in the model, $c_0(t)$ a time-varying offset, k the index of the spectral peak, $\omega(t)$ the time-varying fundamental frequency (heart-rate), $a_k(t)$ is each peaks time-varying amplitude and ϕ_k is each peaks phase.

Such a model can then be fit to the incoming data in real-time using e.g. an Extended Kalman Filter (EKF). This has previously been proposed by e.g. Parker and Anderson [48] and was since successfully implemented for several problems where time-evolving, (quasi)-periodic signals need to be tracked such as the passive Sonar-tracking and identification of submarines, where the vessels rotating engine generates a approximately periodic sound, but frequency changes with the targets speed and amplitude with distance [48, 66]. Yuen et al.[68, 69] used a model similar to that from Parker and Anderson for synchronizing a surgical robot to heart motion.

For denoising the PT signal, an EKF was implemented in Matlab using the Fourier-synthesis model from Eq. 6.4 and the unfiltered cardiac independent component as input. In short, the Kalman Filter uses the current state of the model to predict the next incoming sample (prediction phase). Then the next sample is compared to this prediction in a least-squares sense and the model is corrected, if necessary (correction step). This process is repeated as samples come in and, based on the covariance of measured data, the so called Kalman-gain K_G is computed, which determines whether more trust should be put in the predicted or the measured data. This essentially means that when measured data is very noisy, it is less reliable and more trust is put in the model-predicted value. Conversely, when measured data is less noisy the amount of correction to the model is increased. If the underlying model is non-linear, an Extended Kalman Filter is used which linearizes the problem around the working point ($1^{st} order$), requiring to either know the models Jacobian or to compute it numerically. In above model, the Jacobian can be easily computed analytically. For a good introduction to the Kalman Filter and Extended Kalman Filter see e,g. Ribeiro [56] or Anderson and Moore [5].

The EKF is an attractive alternative to classical digital time-domain filters as it does not have any intrinsic delay other then that accrued by the computation itself, which, if the Jacobians are known analytically, has complexity $\mathcal{O}(N^3)$ with N the number of free parameters [24]. In the authors opinion, an efficient implementation

of the EKF algorithm running on a powerful machine will produce only negligible processing delays.

Figure 6.5 shows output of an EKF implemented in Matlab (top). The model was chosen to include the fundamental frequency and one harmonic. The output $\hat{s}_{PT}$ of the EKF is plotted in red, black dots are the noisy input signal and the dashed blue trace is the lowpass filtered input $s_{PT,filt}$, used as ground truth. The bottom plot shows residuals $r(t) = s_{PT,filt} - \hat{s}_{PT}$.

The distribution of residuals is plotted in Fig. 6.6 together with residuals over the complete 90 s acquisition. Residuals are gaussian with nearly zero-mean, indicating that there are no systematic deviations from ground truth. Note the higher residuals in the first $5 - 10$ s: The initial guess for the model parameters was not ideal and the EKF therefore took some time to stabilized. This behaviour is also noticeable in Fig. 6.7.

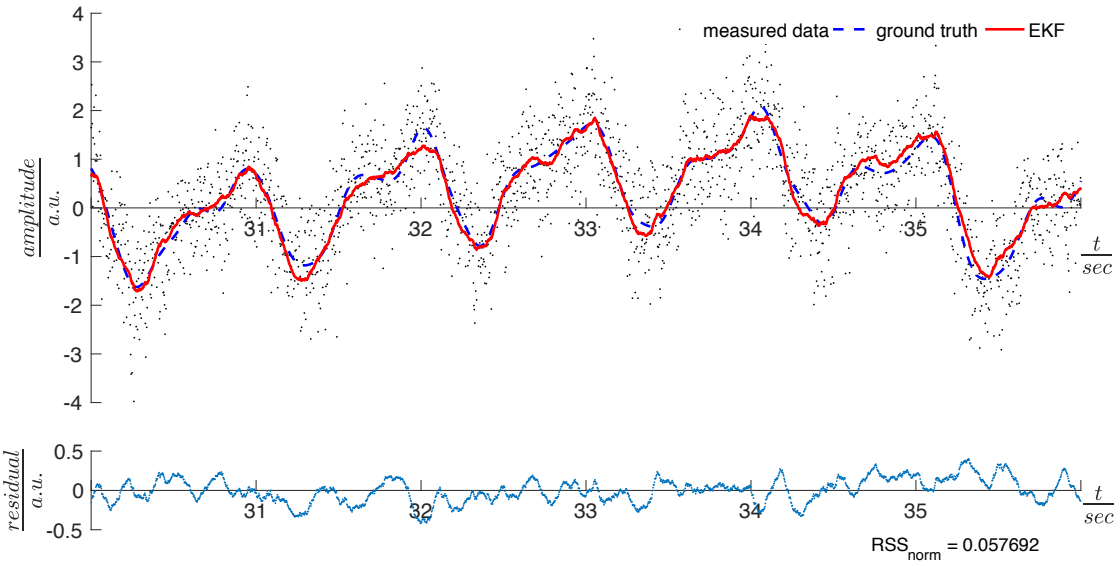

Figure 6.5.: Output of the EKF using a one harmonic model. Top: noisy input signal (black dots), ground truth (dashed blue) and EKF output generated from the fitted model (red). Bottom: residual $r(t) = s_{PT,filt} - \hat{s}_{PT}$.

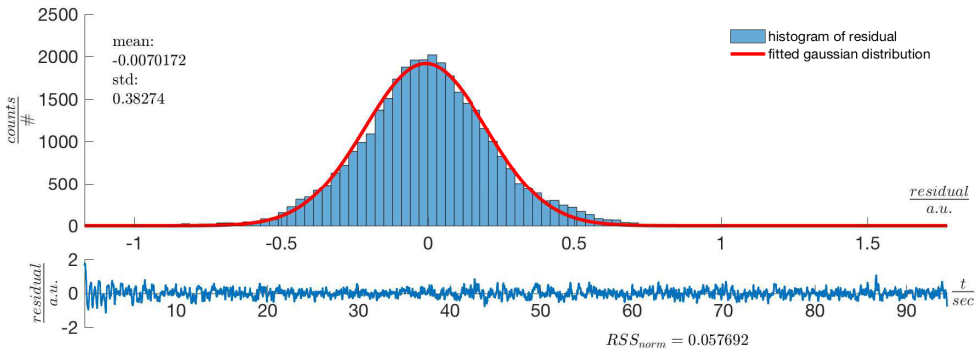

Figure 6.6.: Top: Distribution of residuals and gaussian best-fit. Bottom: Residuals over the full 90 s acquisition.

Figure 6.7 shows the tracked parameters over 90 s. Offset, amplitudes of the fundamental and harmonic, fundamental frequency and phase of fundamental and harmonic are plotted. Ground truth exists for offset (lowpass filtered input) and frequency (from time-resolved spectrogram analysis) and are plotted in red. Offset and frequency are tracked with high accuracy. The phases behave as expected, simply increasing over time and $\Theta_2(t) \approx 2\Theta_1(t)$. Thus, it might be unnecessary to have both phases as free parameters, reducing the complexity of the model to just five free parameters.

This model-based approach offers another potential benefit: It is well known that the problem of numerical differentiation is extremely ill posed, but differentiation might be a useful tool in trigger detection algorithms. However, since the output of the EKF is a parameterized model, much more stable differentiation can be achieved by simply differentiating the model itself and using the EKFs results in this new model. This is shown in Fig. 6.8, where the output of $\hat{s}_{PT}$ and $\frac{d}{dt}\hat{s}_{PT}$ are shown against the filtered ground truth $s_{PT,filt,BP}$ and its derivative $\frac{d}{dt}s_{PT,filt,BP}$. The ground truth $s_{PT,filt,BP}$ has been bandpass filtered to remove low-frequency offset and the EKF output $\hat{s}_{PT,noDC}$ has been computed from the model by simply omitting the offset term $c_0(t)$.

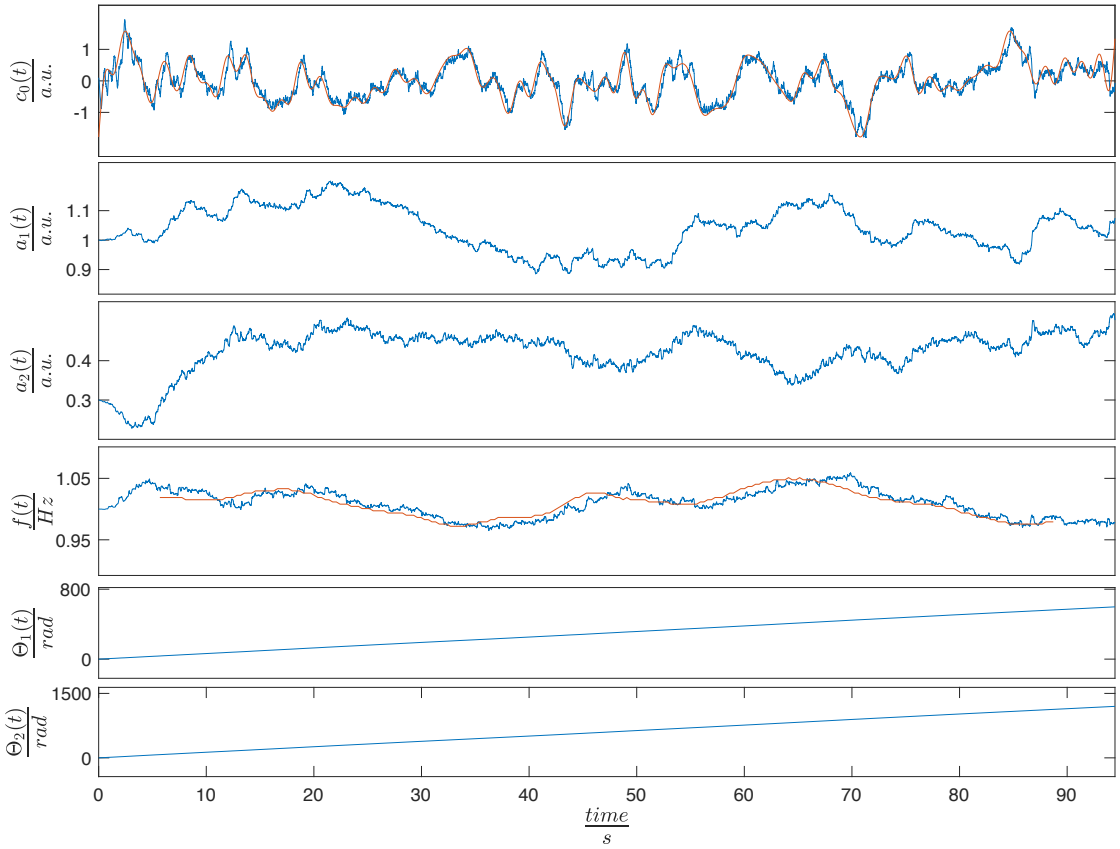

Figure 6.7.: Tracked parameters of the one-harmonic EKF. From top to bottom: offset $c_0(t)$, amplitude $a_1(t)$, amplitude $a_2(t)$, fundamental frequency $f_1(t) = \frac{\omega_1(t)}{2\pi}$, phase of the fundamental Θ_1 and phase of the harmonic Θ_2. If available, ground truth is plotted in red.

While this "pseudo-analytic" derivative fails to capture all the dynamics present in the numerical derivative of the ground-truth, it should enable accurate and reliably triggering on e.g. the "maximum-velocity" trigger used throughout this thesis.

Although the proposed method has not yet been thoroughly investigated, these preliminary results are very promising and should enable minimal-delay real-time processing of PilotTone signals suitable for prospective triggering. Some consideration needs to be given to the fact that the EKF takes, depending on the quality of the initial guess, some seconds to stabilize. This initial guess could in practical implementations be derived from the calibration data that is needed for ICA.

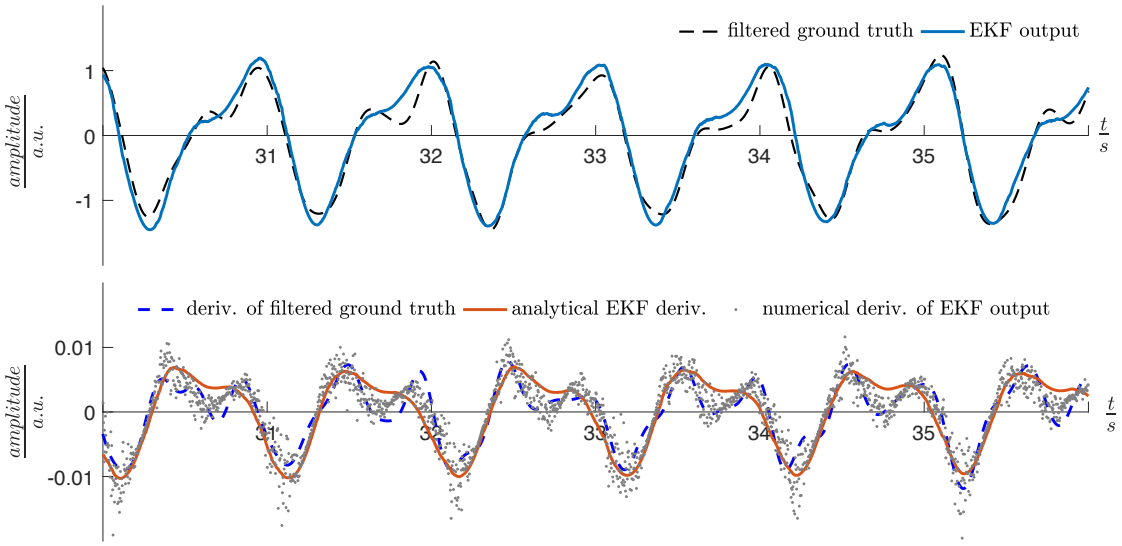

Figure 6.8.: Top: EKF output (blue) and filtered PT trace as ground truth (black). Bottom: Derivative calculated analytically from EKF model parameters (orange), numerical derivative of filtered PT trace (blue) and numerical derivative of EKF output (grey dots). Ground truth was bandpass-filtered and EKF output was calculated without the offset term $c_0(t)$ to eliminate offset.

Another interesting aspect is the EKFs ability to, to some extent, accurately predict future values of the model. It might be possible to predict at least some 10 or even 100 ms of cardiac activity which would be highly beneficial for cardiac MRI sequences needing highly accurate preparatory pulses such as inversion- or saturation recovery.

7. Conclusion & Further development

It could be shown in this thesis that the cardiac component can be reliably extracted in a wide variety of volunteers (see Sec. 5.2) and that PT triggers correspond well to ECG triggers (see Sec. 5.3). The PT transmitter should be placed anterior to the patients heart, with some cm of tolerance (Sec. 5.4).

Furthermore, the method should offer some additional benefits over ECG triggering such as the ability to extract additional interesting trigger points such as the start of diastole or diastasis or period of minimal motion between the rapid inflow phase and the start of the atrial systole (see Fig. 6.2). However, it has not yet been established that the PT cardiac signal indeed corresponds to total cardiac volume. Further experiments are needed here such as comparing the PT signal to cardiac volume-curves computed from e.g. real-time, compressed-sensing CINE measurements.

Preliminary results also show that efficient real-time processing is possible, which is of paramount importance to practical implementations of PT navigation.

In order to establish PT navigation as an attractive, easy to use alternative to ECG, some further development is necessary. In the current implementation, PT data can only be acquired when imaging readouts are active. In sequences that acquire data continuously this is not problematic, but many sequences introduce pauses, for instance to wait until a desired relaxation state is reached. This would result in gaps in the PT navigator signal. Also, PT navigators can not currently

be acquired between imaging sequences. Preliminary results show that an ICA solution computed at the beginning of the scan session can be reused as long as the patient remains reasonably still. However, the Kalman filter used for realtime processing requires some heartbeats to stabilize, taking away precious time before triggering can start, especially in breath-held examinations. To solve this problem, it will be necessary to reprogram the scanner to allow for ADC readouts even when not imaging. In practice, this would also enable continuous monitoring of the cardiac activity in high-risk patients.

Another useful enhancement would be the ability to control both frequency and amplitude of the PT signal. While the PT navigator could be reliably extracted in most datasets and all volunteers, it seems logical that slightly increased amplitude could be necessary in very large patients. Amplitude is however limited as the PT carrier should remain in the linear range of the receiver. Frequency adjustment would be needed to use the PT navigator on arbitrary clinical sequences, as the bandwidth used for imaging is application specific.

No experiments have so far been done on patients with arrhythmia. While arrhythmic heartbeats are not expected to pose a problem in PT signal extraction, the response time of the Kalman filter would depend on its current state, i.e. favoring either measurement data over model-predicted data (fast adaptation) or vice versa (slower adaptation). In theory, arrhythmic beats should result in a sudden increase of prediction error, reflected in a change of Kalman gain. This information could then be used to reject the heartbeat.

The physical model for modulation of the PT carrier presented in Sec. 3.2 has so far not been evaluated against experimental data. At the time of writing of this thesis, a phantom is being developed by a team at the Siemens Innovation Think Tank (ITT) that should aid in validation of the proposed model. The phantom consists of two compartments, an outer layer filled with a gel that has electrical and magnetic properties similar to those in human tissues and a inner sphere that can be inflated with either air or a liquid. The phantom will be MR compatible, enabling experiments inside the scanners bore, but can also be used in a stan-

dalone setup, with Pilot Tones being generated by the mobile PT transmitter and measurements made using a simple receive coil and an amplifier. The phantoms geometric simplicity should also enable validation of the experiments against a numerical EM simulation.

Jaeschke et al. [30, 31] recently proposed a somewhat similar method, estimating the scatter-matrix in a parallel-transmit (pTx) system at 7 T using the systems SAR monitor. Instead of using a continuous-wave pilot, their method relies on the RF pulses used for MR imaging. Cardiac signals generated by their method look strikingly similar to those from PT navigation and measures of time differences between ECG and triggers derived from the respective method are comparable: Jaeschke et al. found a standard-deviation of 12.5 ms during breath-holding and 22 ms during free-breathing [30], while for PT navigation the average trigger-jitter (defined more conservatively in this thesis as two times the standard-deviation, see Fig. 4.5) was 30.2 ms during free breathing.

In conclusion, PT navigation has been shown to be a feasible alternative to ECG triggering and further research in this direction is highly warranted.

Bibliography

[1] http://mriquestions.com/navigator-echoes.html.

[2] D. Abi-Abdallah, V. Robin, A. Drochon, and O. Fokapu. Alterations in human ECG due to the MagnetoHydroDynamic effect: A method for accurate R peak detection in the presence of high MHD artifacts. *Annual International Conference of the IEEE Engineering in Medicine and Biology - Proceedings*, pages 1842–1845, 2007. ISSN 05891019. doi: 10.1109/IEMBS.2007.4352673.

[3] T. Adah, P. J. Schreier, and L. L. Scharf. Complex-Valued Signal Processing : The Proper Way to Deal With Impropriety. 59(11):5101–5125, 2011.

[4] V. K. Ananthashayana and M. Jyothirmayi. Blind Source Separation Using Modified Gaussian FastICA. *World Academy of Science, Engineering & Technology*, 1(3):394–397, 2009.

[5] B. D. O. Anderson and J. B. Moore. *Optimal Filtering*. Dover Books on Electrical Engineering. Dover Publications, 2005. ISBN 9780486439389. URL `https://books.google.de/books?id=VZ4oAwAAQBAJ`.

[6] A. Antoniou. *Digital filters : analysis, design, and applications*. New York : McGraw-Hill, 2nd ed edition, 1993. ISBN 0071126007. Includes bibliographical references and index.

[7] E. Bingham, S. Kaski, J. Laaksonen, and J. Lampinen. *Advances in Independent Component Analysis and Learning Machines*. Elsevier Science, 2015. ISBN 9780128028070. URL `https://books.google.de/books?id=hQ50BQAAQBAJ`.

[8] J. Bortz, G. Lienert, and K. Boehnke. *Verteilungsfreie Methoden in der Biostatistik*. Springer-Lehrbuch. Springer Berlin Heidelberg, 2013. ISBN 9783662225936. URL https://books.google.de/books?id=19jvBgAAQBAJ.

[9] C. I. O. Brookes, P. A. White, M. Staples, P. J. Oldershaw, A. N. Redington, P. D. Collins, and M. I. M. Noble. Myocardial contractility is not constant during spontaneous atrial fibrillation in patients. *Circulation*, 98:1762–1768, 1998. ISSN 0009-7322. doi: 10.1161/01.CIR.98.17.1762.

[10] J. Cardoso and A. Souloumiac. Blind beamforming for non-gaussian signals. *IEE Proceedings F Radar and Signal Processing*, 140(6):362, 1993. ISSN 0956375X. doi: 10.1049/ip-f-2.1993.0054.

[11] A. Cieslinski, W. K. Hui, P. J. Oldershaw, G. Gregoratos, and D. Gibson. Interaction between systolic and diastolic time intervals in atrial fibrillation. *British heart journal*, 51(4):431–7, 1984. ISSN 0007-0769. URL http://www.pubmedcentral.nih.gov/articlerender.fcgi?artid=481526{&}tool=pmcentrez{&}rendertype=abstract.

[12] P. Comon. Independent component analysis, A new concept? *Signal Processing*, 36(3):287–314, 1994. ISSN 01651684. doi: 10.1016/0165-1684(94)90029-9.

[13] J. Constantino, Y. Hu, A. C. Lardo, and N. A. Trayanova. Mechanistic insight into prolonged electromechanical delay in dyssynchronous heart failure: a computational study. *AJP: Heart and Circulatory Physiology*, 305(8):H1265–H1273, 2013. ISSN 0363-6135. doi: 10.1152/ajpheart.00426.2013. URL http://ajpheart.physiology.org/cgi/doi/10.1152/ajpheart.00426.2013.

[14] D. Creanga, C. Nadejde, and P. Gasner. Dynamical analysis of heart beat from the viewpoint of chaos theory. *Romanian Journal of Physics*, 56:177–184, 2011. ISSN 1221146X. URL http://www.nipne.ro/rjp/2011{_}56{_}1-2.html.

[15] R. L. Ehman and J. P. Felmlee. Adaptive technique for high-definition MR imaging of moving structures. *Radiology*, 173(1):

255–263, 1989. ISSN 0033-8419. doi: 10.1148/radiology.173.1.2781017. URL http://eutils.ncbi.nlm.nih.gov/entrez/eutils/elink.fcgi?dbfrom=pubmed{&}id=2781017{&}retmode=ref{&}cmd=prlinks.

[16] B. S. Everitt, S. Landau, M. Leese, and D. Stahl. *Cluster Analysis*, volume 14. 2011. ISBN 9780470749913. doi: 10.1007/BF00154794. URL http://www.springerlink.com/index/10.1007/BF00154794.

[17] J. Felblinger, J. Slotboom, R. Kreis, B. Jung, and C. Boesch. Restoration of Electrophysiological Signals Distorted by Inductive Effects of Magnetic Field Gradients During MR Sequences. *Magnetic resonance in medicine*, 41(4): 715–721, 1999. ISSN 0740-3194. doi: 10.1002/(SICI)1522-2594(199904)41.

[18] S. E. Fischer, S. A. Wickline, and C. H. Lorenz. Novel real-time R-wave detection algorithm based on the vectorcardiogram for accurate gated magnetic resonance acquisitions. *Magnetic Resonance in Medicine*, 42(2):361–370, 1999. ISSN 07403194. doi: 10.1002/(SICI)1522-2594(199908)42:2<361::AID-MRM18>3.0.CO;2-9.

[19] M. Girolami, editor. *Advances in Independent Component Analysis*. Springer-Verlag London, 1 edition, 2000.

[20] R. Glaser. *Biophysics*. Springer Berlin Heidelberg, 2013. ISBN 9783662044940. URL https://books.google.de/books?id=RUX1CAAAQBAJ.

[21] X. Guo, X. Wu, X. Gong, and L. Zhang. Envelope detection based on online ICA algorithm and its application to motor imagery classification. *International IEEE/EMBS Conference on Neural Engineering, NER*, (2):1058–1061, 2013. ISSN 19483546. doi: 10.1109/NER.2013.6696119.

[22] V. Gurev, J. Constantino, J. J. Rice, and N. A. Trayanova. Distribution of electromechanical delay in the heart: Insights from a three-dimensional electromechanical model. *Biophysical Journal*, 99(3):745–754, 2010. ISSN 00063495. doi: 10.1016/j.bpj.2010.05.028. URL http://dx.doi.org/10.1016/j.bpj.2010.05.028.

[23] J. Himberg, A. Hyvärinen, and F. Esposito. Validating the Independent Components of Neuroimaging Time-Series via Clustering and Visualization. *NeuroImage*, 22(3):1–17, 2003. ISSN 10538119. doi: 10.1016/j.neuroimage.2004.03.027. URL `http://www.sciencedirect.com/science/article/pii/S1053811904001661`.

[24] S. A. Holmes, G. Klein, and D. W. Murray. An O(N2) Square Root Unscented Kalman Filter for Visual Simultaneous Localization and Mapping. *IEEE transactions on pattern analysis and machine intelligence*, 31(7):1251–1263, 2009. ISSN 0162-8828. doi: 10.1109/TPAMI.2008.189.

[25] S. H. Hsu, T. Mullen, T. P. Jung, and G. Cauwenberghs. Online recursive independent component analysis for real-time source separation of high-density EEG. *Conference proceedings: Annual International Conference of the IEEE Engineering in Medicine and Biology Society. IEEE Engineering in Medicine and Biology Society. Annual Conference*, 2014(1):3845–3848, 2014. ISSN 1557170X. doi: 10.1109/EMBC.2014.6944462.

[26] A. Hyvärinen. New approximations of differential entropy for independent component analysis and projection pursuit. *Proceedings of the 1997 Conference on Advances in Neural Information Processing Systems*, 10:273–279, 1998. URL `http://dl.acm.org/citation.cfm?id=302528.302606`.

[27] A. Hyvärinen, J. Karhunen, and E. Oja. Independent Component Analysis. *Applied and Computational Harmonic Analysis*, 21(1):135–144, 2001. ISSN 10635203. doi: 10.1002/0471221317. URL `http://linkinghub.elsevier.com/retrieve/pii/S1063520306000509{%}5Cnhttp://doi.wiley.com/10.1002/0471221317`.

[28] A. Hyvärinen. Fast and robust fixed-point algorithm for independent component analysis. *IEEE Transactions on Neural Networks and Learning Systems*, 10:626–634, 1999. ISSN 1045-9227. doi: 10.1109/72.761722.

[29] A. Hyvärinen. Independent component analysis: recent advances. *Philosophical Transactions of the Royal Society A: Mathematical, Physical*

and Engineering Sciences, 371(1984), dec 2012. URL `http://rsta.royalsocietypublishing.org/content/371/1984/20110534.abstract`.

[30] S. H. F. Jaeschke, C. O'Brien, A. T. Hess, and M. D. Robson. Contact-free Cardiac Motion Estimation using the Scatter of a Parallel Transmit Coil at 7T MRI. In *Proc. Intl. Soc. Mag. Reson. Med. 25 (2017)*, page 3262, 2017.

[31] S. H. F. Jaeschke, M. D. Robson, and A. T. Hess. Evaluating the Influence of B1-Shimming on Contact-free Cardiac Gating using Scatter of a Parallel Transmit Coil at 7T MRI. In *Proc. Intl. Soc. Mag. Reson. Med. 25 (2017)*, page 1131, 2017.

[32] C. C. Johnson and A. W. Guy. Nonionizing Electromagnetic Wave Effects in Biological Materials and Systems. *Proceedings of the IEEE*, 60(6):692–718, 1972.

[33] J. Karhunen, E. Oja, L. Wang, R. Vigario, and J. Joutsensalo. A class of neural networks for independent component analysis. *IEEE transactions on neural networks / a publication of the IEEE Neural Networks Council*, 8(3): 486–504, 1997. ISSN 1045-9227. doi: 10.1109/72.572090. URL `http://www.ncbi.nlm.nih.gov/pubmed/18255654`.

[34] M. Keralapura, M. Pourfathi, and B. Sirkeci-Mergen. Impact of contrast functions in Fast-ICA on twin ECG separation. *IAENG International Journal of Computer Science*, 38(1):38–47, 2011. ISSN 1819656X.

[35] V. Q. Lance and D. H. Spodick. Heart rate–left ventricular ejection time relations. Variations during postural change and cardiovascular challenges. *British heart journal*, 38(12):1332–1338, 1976. ISSN 1355-6037. doi: 10.1136/hrt.38.12.1332.

[36] J. C. Lin and J. Salinger. Microwave Measurement of Respiration. In *Microwave Symposium, 1975 IEEE-MTT-S International*, pages 285–287, 1975. doi: 10.1109/MWSYM.1975.1123362.

[37] J. C. Lin, J. Kiernicki, M. Kiernicki, and P. B. Wollschlaeger. Microwave apexcardiography. *IEEE Transactions on Microwave Theory and Techniques*, 27(6):618–620, 1979. ISSN 15579670. doi: 10.1109/TMTT.1979.1129682.

[38] D. A. Mahajan and G. Birajdar. Blind Source Separation Using Modified Contrast Function in Fast ICA Algorithm. 6(4):14–17, 2010.

[39] A. Marian. On Mice, Rabbits, and Human Heart Failure. *Circulation*, 111: 2276–2279, 2005. ISSN 00092665. doi: 10.1007/s11103-011-9767-z.Plastid.

[40] J. Martin Bland and D. Altman. Statistical Methods for Assessing Agreement Between Two Methods of Clinical Measurement. *The Lancet*, 327(8476):307–310, 1986. ISSN 01406736. doi: 10.1016/S0140-6736(86)90837-8.

[41] H. M. Mertens, H. Mannebach, G. Trieb, and U. Gleichmann. Influence of Heart Rate on Systolic Time Intervals: Effects of Atrial Pacing versus Dynamic Exercise. *Clin. Cardiol*, 4:22–27, 1981.

[42] Y. E. Moskalenko. Utilization of superhigh frequencies in biological investigations. *Biophysics (USSR), (english translation)*, 3:619–626, 1958.

[43] Y. E. Moskalenko. Application of centimetre radio waves for non-contact recording of changes in volume of biological specimens. *Biophysics (USSR), (english translation)*, 5(2):225–228, 1960.

[44] M. S. Nacif, A. Zavodni, N. Kawel, E.-Y. Choi, J. A. C. Lima, and D. A. Bluemke. Cardiac magnetic resonance imaging and its electrocardiographs (ECG): tips and tricks. *The international journal of cardiovascular imaging*, 28(6):1465–75, 2012. ISSN 1875-8312. doi: 10.1007/s10554-011-9957-4. URL `http://www.ncbi.nlm.nih.gov/pubmed/22033762{%}5Cnhttp://www.pubmedcentral.nih.gov/articlerender.fcgi?artid=PMC3476721`.

[45] National Communications System Technology & Standards Division. Federal Standard 1037C, 1996.

[46] K. Nehrke and D. Manke. Advanced Navigator Techniques. 2(2):6–7, 2000.

[47] E. Oja and Z. Yuan. The FastICA Algorithm Revisited: Convergence Analysis. *IEEE Transactions on Neural Networks*, 17(6):1370–1381, 2006.

[48] P. J. Parker and B. D. O. Anderson. Frequency tracking of nonsinusoidal periodic signals in noise. *Signal Processing*, 20(2):127–152, 1990. ISSN 01651684. doi: 10.1016/0165-1684(90)90124-H.

[49] D. Paulson. *Applied Statistical Designs for the Researcher*. Chapman & Hall/CRC Biostatistics Series. Taylor & Francis, 2003. ISBN 9780824756406. URL `https://books.google.de/books?id=LzRr3MgaLBsC`.

[50] R. Pethig. Electrical Properties of Biological Tissue. *Modern Bioelectricity*, pages 93–132, 1988. URL `http://andrewamarino.com/modernbioelectricity.html`.

[51] F. Pfanner, J. Maier, T. Allmendinger, T. Flohr, and M. Kachelrieß. Monitoring internal organ motion with continuous wave radar in CT. *Medical Physics*, 40(9):091915, 2013. ISSN 00942405. doi: 10.1118/1.4818061. URL `http://doi.wiley.com/10.1118/1.4818061`.

[52] F. Pfanner, T. Allmendinger, B. Bohn, T. Flohr, and M. Kachelrieß. Monitoring cardiac motion in CT using a continuous wave radar embedded in the patient table. *Medical Physics*, 41(8):081908, 2014. ISSN 00942405. doi: 10.1118/1.4886056. URL `http://doi.wiley.com/10.1118/1.4886056`.

[53] D. Piccini, A. Littmann, S. Nielles-Vallespin, and M. O. Zenge. Respiratory self-navigation for whole-heart bright-blood coronary MRI: Methods for robust isolation and automatic segmentation of the blood pool. *Magnetic Resonance in Medicine*, 68(2):571–579, 2012. ISSN 07403194. doi: 10.1002/mrm.23247.

[54] J. Provost, W.-N. Lee, K. Fujikura, and E. E. Konofagou. Imaging the electromechanical activity of the heart in vivo. *Proceedings of the National Academy of Sciences of the United States of America*, 108(21):8565–

70, 2011. ISSN 1091-6490. doi: 10.1073/pnas.1011688108. URL `http://www.pnas.org/content/108/21/8565.long`.

[55] R Core Team. *R: A Language and Environment for Statistical Computing*. R Foundation for Statistical Computing, Vienna, Austria, 2017. URL `https://www.R-project.org/`.

[56] M. I. Ribeiro. Kalman and Extended Kalman Filters : Concept , Derivation and Properties. *Institute for Systems and Robotics Lisboa Portugal*, (February):42, 2004. doi: 10.1.1.2.5088. URL `http://citeseerx.ist.psu.edu/viewdoc/download?doi=10.1.1.2.5088{&}rep=rep1{&}type=pdf`.

[57] A. Rudge. *The Handbook of Antenna Design*. Number Bd. 1 in Electromagnetics and Radar Series. P. Peregrinus, 1982. ISBN 9780906048825. URL `https://books.google.de/books?id=njTri1942n4C`.

[58] V. J. Schmithorst. Higher-order Contrast Functions Improve Performance Of Independent Component Analysis Of FMRI Data. *Journal of Magnetic Resonance*, 29(1):242–249, 2009. doi: 10.1002/jmri.21621.HIGHER-ORDER.

[59] L. Schröder. *Information Content of a Novel MR Navigator Relating to Physiological Activities*. Master's thesis, Friedrich-Alexander-Universität Erlangen-Nürnberg, 2015.

[60] L. Schroeder, J. Wetzl, A. Maier, L. Lauer, J. Bollenbeck, M. Fenchel, and P. Speier. A Novel Method for Contact-Free Cardiac Synchronization Using the Pilot Tone Navigator. In *Proc. Intl. Soc. Mag. Reson. Med. 24*, page 0410, 2016. doi: 10.1002/mrm.25858.

[61] L. Schroeder, J. Wetzl, A. Maier, R. R. Rehner, M. Fenchel, and P. Speier. Two-Dimensional Respiratory-Motion Characterization for Continuous MR Measurements Using Pilot Tone Navigation. In *Proc. Intl. Soc. Mag. Reson. Med. 24*, page 3103, 2016. doi: 10.1007/s10334-015-0487-2.

[62] P. Speier, M. Fenchel, and R. Rehner. PT-Nav: a novel respiratory navigation method for continuous acquisitions based on modulation of a pilot tone in the

MR-receiver. In *Book of Abstracts ESMRMB 2015*, volume 28, pages S97–S98. Magnetic Resonance Materials in Physics, Biology and Medicine, 2015. ISBN 09685243. doi: 10.1007/s10334-015-0488-1. URL `http://link.springer.com/10.1007/s10334-015-0488-1`.

[63] J. J. Suttie, L. Delabarre, A. Pitcher, P. F. van de Moortele, S. Dass, C. J. Snyder, J. M. Francis, G. J. Metzger, P. Weale, K. Ugurbil, S. Neubauer, M. Robson, and T. Vaughan. 7 Tesla (T) human cardiovascular magnetic resonance imaging using FLASH and SSFP to assess cardiac function: Validation against 1.5T and 3T. *NMR in Biomedicine*, 25(1):27–34, 2012. ISSN 09523480. doi: 10.1002/nbm.1708.

[64] P. Tichavský, Z. Koldovský, and E. Oja. Performance Analysis of the FastICA Algorithm and Cramér – Rao Bounds for Linear Independent Component Analysis. *IEEE Transactions on Signal Processing*, 54(4):1189–1203, 2006.

[65] N. A. Trayanova and J. J. Rice. Cardiac electromechanical models: From cell to organ. *Frontiers in Physiology*, 2 AUG(August):1–19, 2011. ISSN 1664042X. doi: 10.3389/fphys.2011.00043.

[66] M. Üner. *Frequency, Amplitude and PhaseTracking of Nonsinusoidal Signal in Noise with Extended Kalman Filter*. Master's thesis, Naval Postgraduate School, Monterey, California, 1991.

[67] J. Wetzl, L. Schroeder, C. Forman, F. Lugauer, R. Rehner, M. Fenchel, A. Maier, J. Hornegger, and P. Speier. Two-Dimensional Respiratory-Motion Characterization for Continuous MR Measurements Using Pilot Tone Navigation. In *Proc. Intl. Soc. Mag. Reson. Med. 24*, page 3103, 2016. doi: 10.1007/s10334-015-0487-2.

[68] S. G. Yuen, D. T. Kettler, and R. D. Howe. Robotic motion compensation for beating intracardiac surgery. *2008 10th International Conference on Control, Automation, Robotics and Vision, ICARCV 2008*, 28(10):617–622, 2008. ISSN 0278-3649. doi: 10.1109/ICARCV.2008.4795589.

[69] S. G. Yuen, P. M. Novotny, and R. D. Howe. Quasiperiodic predictive filtering for robot-assisted beating heart surgery. *Proceedings - IEEE International Conference on Robotics and Automation*, pages 3875–3880, 2008. ISSN 10504729. doi: 10.1109/ROBOT.2008.4543806.

[70] M. Zaitsev, J. Maclaren, and M. Herbst. Motion Artefacts in MRI: a Complex Problem with Many Partial Solutions. *J Magn Reson Imaging*, 42(4):165–187, 2015. ISSN 2045-2322. doi: 10.1007/128.

[71] S. H. L. Zhang, Z. T. H. Tse, C. L. Dumoulin, R. Y. Kwong, W. G. Stevenson, R. Watkins, J. Ward, W. Wang, and E. J. Schmidt. Gradient-induced voltages on 12-lead ECGs during high duty-cycle MRI sequences and a method for their removal considering linear and concomitant gradient terms. *Magnetic Resonance in Medicine*, 75(5):2204–2216, 2016. ISSN 15222594. doi: 10.1002/mrm.25810.

A. Appendix

Table A.1.: Quality I_q, reliability I_r and combined index I_{qr} for the symmetric algorithm, 12 independent components and contrasts tanh, pow3 and gauss. For the following statistical evaluation, datasets for which one or more combination of parameters failed (marked in red) had to be excluded.

Volunteer		**tanh contrast**				**pow3 contrast**				**gauss contrast**			
#	**N**	$\mathbf{I_q}$	$\mathbf{N_{IC}}$	$\mathbf{I_r}$	$\mathbf{I_{qr}}$	$\mathbf{I_q}$	$\mathbf{N_{IC}}$	$\mathbf{I_r}$	$\mathbf{I_{qr}}$	$\mathbf{I_q}$	$\mathbf{N_{IC}}$	$\mathbf{I_r}$	$\mathbf{I_{qr}}$
1	1	0.99	200	1.00	0.99	0.96	200	1.00	0.96	0.97	200	1.00	0.97
2	1	0.96	200	1.00	0.96	0.85	200	1.00	0.85	0.96	200	1.00	0.96
3	1	0.97	200	1.00	0.97	0.99	200	1.00	0.99	0.97	200	1.00	0.97
3	2	1.00	200	1.00	1.00	0.97	200	1.00	0.97	0.99	200	1.00	0.99
3	3	0.97	200	1.00	0.97	0.95	200	1.00	0.95	0.97	200	1.00	0.97
3	4	0.93	200	1.00	0.93	0.00	0	0.00	0.00	0.97	199	1.00	0.97
3	5	0.94	200	1.00	0.94	0.92	200	1.00	0.92	0.95	200	1.00	0.95
4	1	0.95	200	1.00	0.95	0.91	200	1.00	0.91	0.97	200	1.00	0.97
4	2	0.00	0	0.00	0.00	0.00	0	0.00	0.00	0.00	0	0.00	0.00
4	3	0.75	200	1.00	0.75	0.92	200	1.00	0.92	0.67	200	1.00	0.67
4	4	0.00	0	0.00	0.00	0.00	0	0.00	0.00	0.61	163	0.82	0.50
4	5	0.00	0	0.00	0.00	0.00	0	0.00	0.00	0.80	142	0.71	0.57
4	6	0.72	200	1.00	0.72	0.92	200	1.00	0.92	0.56	200	1.00	0.56
4/2	1	0.74	161	0.81	0.60	0.00	0	0.00	0.00	0.72	190	0.95	0.68
4/2	2	0.97	200	1.00	0.97	0.95	200	1.00	0.95	0.92	200	1.00	0.92
4/2	3	0.00	0	0.00	0.00	0.00	0	0.00	0.00	0.62	200	1.00	0.62

7	1	0.93	200	1.00	0.93	0.87	200	1.00	0.87	0.94	200	1.00	0.94
8	1	0.94	200	1.00	0.94	0.95	200	1.00	0.95	0.97	200	1.00	0.97
8	2	0.98	200	1.00	0.98	0.94	200	1.00	0.94	0.99	200	1.00	0.99
9	1	0.00	0	0.00	0.00	0.00	0	0.00	0.00	0.00	0	0.00	0.00
11	1	0.94	200	1.00	0.94	0.81	200	1.00	0.81	0.95	200	1.00	0.95
12	1	0.98	200	1.00	0.98	0.96	200	1.00	0.96	0.98	200	1.00	0.98
12	2	0.98	200	1.00	0.98	0.97	200	1.00	0.97	0.97	200	1.00	0.97
12	3	1.00	200	1.00	1.00	0.96	200	1.00	0.96	0.98	200	1.00	0.98
12	4	0.98	200	1.00	0.98	0.94	200	1.00	0.94	0.98	200	1.00	0.98
12	5	0.99	200	1.00	0.99	0.92	200	1.00	0.92	0.99	200	1.00	0.99
12	6	0.99	200	1.00	0.99	0.97	200	1.00	0.97	0.97	200	1.00	0.97
12	7	0.94	200	1.00	0.94	0.96	200	1.00	0.96	0.94	200	1.00	0.94
13	1	0.94	200	1.00	0.94	0.94	200	1.00	0.94	0.92	198	0.99	0.91
13	2	0.97	200	1.00	0.97	1.00	200	1.00	1.00	0.98	200	1.00	0.98
13	3	0.96	200	1.00	0.96	0.94	200	1.00	0.94	0.95	200	1.00	0.95
13	4	0.69	191	0.96	0.66	0.96	200	1.00	0.96	0.78	181	0.91	0.71
13	5	0.98	200	1.00	0.98	0.97	200	1.00	0.97	0.98	200	1.00	0.98
13	6	0.90	200	1.00	0.90	0.94	200	1.00	0.94	0.90	200	1.00	0.90
14	1	0.97	200	1.00	0.97	0.95	200	1.00	0.95	0.98	200	1.00	0.98
14	2	0.96	200	1.00	0.96	0.82	200	1.00	0.82	0.94	200	1.00	0.94
14	3	0.00	0	0.00	0.00	0.00	0	0.00	0.00	0.00	0	0.00	0.00
14	4	0.89	200	1.00	0.89	0.00	0	0.00	0.00	0.95	200	1.00	0.95
14	5	0.86	200	1.00	0.86	0.00	0	0.00	0.00	0.96	200	1.00	0.96
14	6	0.00	0	0.00	0.00	0.00	0	0.00	0.00	0.00	0	0.00	0.00
15	1	0.99	200	1.00	0.99	0.98	200	1.00	0.98	1.00	200	1.00	1.00
15	2	0.98	200	1.00	0.98	0.98	200	1.00	0.98	0.98	200	1.00	0.98
15	3	0.98	200	1.00	0.98	0.95	200	1.00	0.95	0.99	200	1.00	0.99
15	4	0.98	200	1.00	0.98	0.99	200	1.00	0.99	0.98	200	1.00	0.98
15	5	0.99	200	1.00	0.99	0.96	200	1.00	0.96	0.99	200	1.00	0.99
16	1	0.98	200	1.00	0.98	0.77	200	1.00	0.77	0.95	200	1.00	0.95
16	2	0.99	200	1.00	0.99	0.97	200	1.00	0.97	0.98	200	1.00	0.98

16	3	0.98	200	1.00	0.98	1.00	200	1.00	1.00	0.98	200	1.00	0.98
16	4	0.98	200	1.00	0.98	0.97	200	1.00	0.97	0.98	200	1.00	0.98
17	1	0.98	200	1.00	0.98	0.91	200	1.00	0.91	0.97	200	1.00	0.97
17	2	0.72	199	1.00	0.72	0.83	200	1.00	0.83	0.94	200	1.00	0.94
17	3	0.97	200	1.00	0.97	0.92	200	1.00	0.92	0.98	200	1.00	0.98
17	4	0.98	200	1.00	0.98	0.98	200	1.00	0.98	0.97	200	1.00	0.97
17	5	0.99	200	1.00	0.99	0.97	200	1.00	0.97	0.99	200	1.00	0.99
17/2	1	0.99	200	1.00	0.99	0.99	200	1.00	0.99	0.98	200	1.00	0.98
17/2	2	0.98	200	1.00	0.98	0.86	200	1.00	0.86	0.96	200	1.00	0.96
17/2	3	0.00	0	0.00	0.00	0.00	0	0.00	0.00	0.00	0	0.00	0.00
18	1	0.98	200	1.00	0.98	0.96	200	1.00	0.96	0.97	200	1.00	0.97
18	2	0.91	200	1.00	0.91	0.97	200	1.00	0.97	0.92	200	1.00	0.92
18	3	0.98	200	1.00	0.98	0.93	200	1.00	0.93	0.98	200	1.00	0.98
18	4	0.87	197	0.99	0.86	0.66	194	0.97	0.64	0.94	200	1.00	0.94
18	5	0.96	200	1.00	0.96	0.98	200	1.00	0.98	0.97	200	1.00	0.97
19	1	0.98	200	1.00	0.98	0.94	200	1.00	0.94	0.98	200	1.00	0.98
19	2	0.96	200	1.00	0.96	0.93	200	1.00	0.93	0.97	200	1.00	0.97
19	3	0.93	199	1.00	0.92	0.89	200	1.00	0.89	0.87	198	0.99	0.86
19	4	0.96	200	1.00	0.96	0.96	200	1.00	0.96	0.94	200	1.00	0.94
19	5	0.88	200	1.00	0.88	0.77	200	1.00	0.77	0.93	200	1.00	0.93
All data	**Mean**	0.83	175.33	0.88	0.83	0.76	164.09	0.82	0.76	0.86	183.15	0.92	0.85
	Std	0.32	65.23	0.33	0.32	0.36	77.23	0.39	0.36	0.26	53.11	0.27	0.27
	Median	0.96	200.00	1.00	0.96	0.94	200.00	1.00	0.94	0.97	200.00	1.00	0.97
Non-failed	**Mean**	0.94	199.10	1.00	0.94	0.90	192.88	0.96	0.90	0.93	197.92	0.99	0.92
	Std	0.07	5.20	0.03	0.08	0.07	0.81	0.00	0.07	0.10	8.99	0.04	0.12
	Median	0.97	200.00	1.00	0.97	0.95	200.00	1.00	0.95	0.97	200.00	1.00	0.97

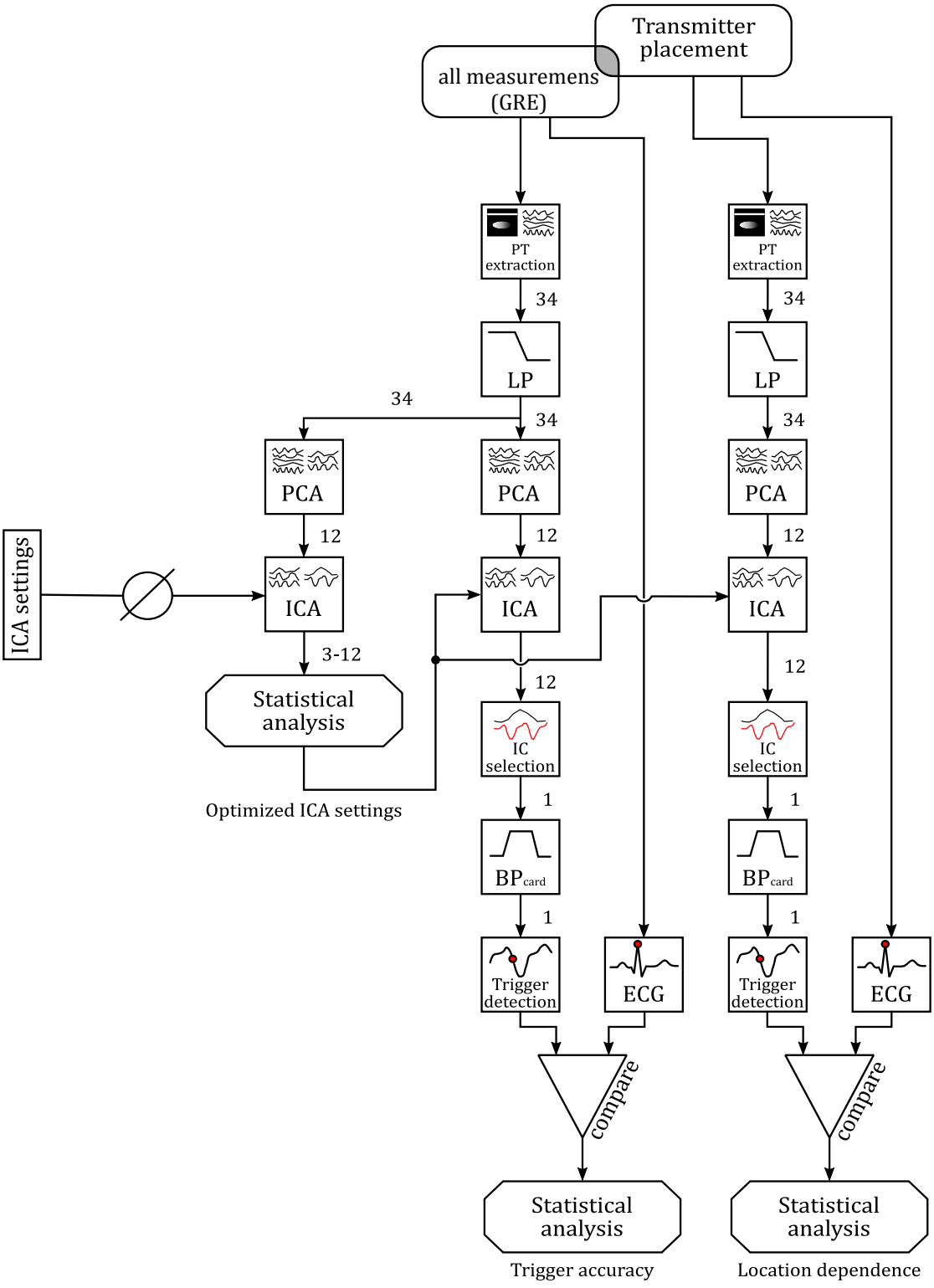

Figure A.1.: Flow-chart of processing steps of all analyses described in Chap. 3 Sec. 4. Numbers next to connections are the number of channels.